Western Graduate&PostdoctoralStudies

Western University
Scholarship@Western

Electronic Thesis and Dissertation Repository

8-28-2023 10:30 AM

Synchrotron Study of Phase Transition and Heterostructures in Metal Oxide Semiconductors

Bingyu Dong, *Western University*

Supervisor: Tsun-Kong Sham, *The University of Western Ontario*

A thesis submitted in partial fulfillment of the requirements for the Master of Science degree in Chemistry

© Bingyu Dong 2023

Follow this and additional works at: https://ir.lib.uwo.ca/etd

 Part of the Analytical Chemistry Commons, and the Physical Chemistry Commons

Recommended Citation

Dong, Bingyu, "Synchrotron Study of Phase Transition and Heterostructures in Metal Oxide Semiconductors" (2023). *Electronic Thesis and Dissertation Repository*. 9668.
https://ir.lib.uwo.ca/etd/9668

This Dissertation/Thesis is brought to you for free and open access by Scholarship@Western. It has been accepted for inclusion in Electronic Thesis and Dissertation Repository by an authorized administrator of Scholarship@Western. For more information, please contact wlswadmin@uwo.ca.

Abstract

Transition metal oxides, including titanium dioxide (TiO_2), zinc oxide (ZnO) and Tin dioxide (SnO_2) are widely recognized semiconducting photocatalysts. This project engages in a detailed examination of the phase transition of TiO_2 and the synthesis of heterostructured metal oxides using an eco-friendly method of ball-milling. A variety of spectroscopy and microscopy techniques have been used to analyze the products. Synchrotron-based techniques: X-ray Absorption near-edge spectroscopy (XANES), X-ray Emission Spectroscopy and X-ray excited optical luminescence (XEOL) can demonstrate the local structure and bonding. The finding highlights a phase transition in TiO_2 and the formation of new zinc titanium compounds at speeds of 300rpm and 500rpm. However, at the 150rpm ball milling speed, heterostructured TiO_2/ZnO and TiO_2/SnO_2 formed. This study offers valuable insights into the impact of ball-milling on the synthesis and transformation of semiconducting transition metal oxides, providing a pathway toward the advancement of high-performance semiconductors.

Keywords: Semiconductor, Heterostructure, Ball-Milling, TiO_2, ZnO, SnO_2, Electronic structure, XANES, XES, XEOL

Summary for Lay Audience

Semiconductors, with their significant utility in the electronic industry, include optoelectronic devices, photoelectrochemical technologies, and high-power electronics, which are continually evolving to meet rising performance demands. Semiconducting transition metal oxides are the most common and extensively characterized heterogeneous photocatalysts such as titanium dioxide (TiO_2), zinc oxide (ZnO) and tin dioxide (SnO_2). Researchers have widely recognized the potential of mixed-phased and heterostructured semiconductors to significantly enhance the photocatalytic properties of semiconductors. Compared to other synthesis methods, ball-milling is renowned as a cost-effective, eco-friendly approach. Ball milling is a mechanical technique widely used to grind samples into a smaller size. During the ball milling process, the centrifugal forces cause speed differences between the balls and jars, creating friction and point collisions and releasing high pulverization energy.

This thesis engages in a comprehensive analysis of the phase transition of TiO_2 and the synthesis of heterostructured metal oxides (TiO_2/ZnO and TiO_2/SnO_2) through ball-milling. For the phase transition of TiO_2, X-ray absorption near-edge structures (XANES) offer greater sensitivity in assessing the chemical and structural environment, and linear combination fitting (LCF) is utilized to determine the chemical ratio within the product. Moreover, the changes in the chemical and electronic environment after the formation of heterostructure TiO_2/ZnO and TiO_2/SnO_2 can be detected by the synchrotron techniques, including X-ray Absorption near-edge spectroscopy (XANES), X-ray Emission Spectroscopy, X-ray excited optical luminescence (XEOL), and 2D X-ray Absorption Near Edge Structure-X-ray Excited Optical Luminescence (2D-XANES-XEOL).

The finding highlights a phase transition in TiO_2 and the formation of new zinc titanium compounds at the speed of 300rpm and 500rpm. However, at the 150rpm ball milling speed, heterostructured TiO_2/ZnO and TiO_2/SnO_2 formed. This study offers valuable insights into the impact of ball-milling on the synthesis and transformation of semiconducting transition metal oxides, paving the path toward the development of high-performance semiconductors.

Co-Authorship Statement

In Chapter 4, the WIEN2K calculation was analyzed by Dr. Yun-Mui You.

The transmission electron microscopy/energy dispersive spectroscopy (TEM-EDX) mapping in Chapter 4 was performed by Ms. Yihong Liu from the Department of Chemistry. The TEM images in Chapter 4 were performed by Mr. Xiaozhang Yao from the Department of Chemical Engineering.

The scanning electron microscopy images in Chapters 3 and 4 were collected with the help of Mr. Todd Simpson and Mr. Tim Goldhawk from the Nanofabrication Faculty at Western University.

The powder X-ray diffraction (PXRD) data as presented in Chapters 3 and 4 was collected with help of Dr. Paul D. Boyle from the X-ray Facility, Department of Chemistry at Western University and Dr. Lo-Yueh Chang at 09A XRD beamline of Taiwan Photon Source (TPS).

The synchrotron data, including X-ray absorption near-edge spectroscopy (XANES), X-ray emission spectroscopy (XES), and X-ray excited optical luminescence (XEOL), as presented in Chapters 3 and 4, were conducted with the invaluable assistance of Dr. Tom Regier and Dr. James Dynes. These experiments were performed at the Spherical Grating Monochromator (SGM) beamline, with additional assistance from Dr. Teak Boyko at the Resonant Elastic and Inelastic X-ray Scattering (REIXS) beamline, both located within the Canadian Light Source (CLS).

Acknowledgments

Firstly, my deepest appreciation is extended to my mentor, Dr. Tsun-Kong Sham, for his invaluable guidance, continuous encouragement, and unswerving patience throughout my graduate study. His extensive knowledge, insightful analysis, and passion for the subject have not only been a source of inspiration but have also fundamentally shaped my own learning and research. Dr. Tsun-Kong Sham has been instrumental in enhancing the quality and scope of my research. His unwavering faith in my abilities, even during the most challenging periods of this endeavour, was an immense source of motivation.

Secondly, I would like to show my sincere gratitude to my group members: Dr. Yun-Mui Yiu, Dr. Zhiqiang Wang, Dr. Weihan Li, Dr. Xuchun Wang, Dr. Minsi Li, Dr. Shumin Zhang, Dr. Yipeng Sun, Dr. Jiamin Fu, Mr. Jiabin Xu, Mr. Zhiliang Dong, and Mr. Carolos Mendes, for their immense contributions, cooperation, and companionship throughout my graduated study. Especially, I wish to extend my heartfelt gratitude to Dr. Jiatang Chen, whose invaluable assistance with my thesis writing has been instrumental to the completion of this project.

Moreover, I wish to show my deep appreciation for the technical assistance from the following people: Dr. Tom Regier and Dr. James Dynes from the SGM beamline and Dr. Teak Boyko from REIXS beamline at the CLS; Dr. Lo-Yue Zhang from TPS; Dr. Paul D. Boyle from the X-ray Facility, Department of Chemistry; by Ms. Yihong Liu from the Department of Chemistry; Mr. Xiaozhang Yao from Department of Chemical Engineering; as well as Mr. Todd Simpson and Mr. Tim Goldhawk from the Nanofabrication Faculty at UWO; Ms. Their expertise and support were instrumental to the success of this study.

The research conducted at Western University has been facilitated by financial support from the Natural Science and Engineering Research Council of Canada (NSERC), the Canadian Research Chair (CRC) program, and the Canada Foundation for Innovation (CFI). Additionally, the Canadian Light Source (CLS) receives its funding from NSERC, the National Research Council (NRC), the Canadian Institutes of Health Research (CIHR), and the University of Saskatchewan. I wish to express my gratitude to the CLS for offering the Graduate Student Travel Support Program. I am also thankful for the Nanofabrication Facility at the University of Western Ontario.

Last but not least, I would like to thank my family in China. To my loving parents, who have always been my pillars of strength, your unwavering belief in me and ceaseless encouragement have been the cornerstone of my perseverance through this journey. I also would like to thank towards my boyfriend and my beloved pets, who have been my constant companions.

Table of Contents

List of Tables

List of Figures

ALD	Atomic layer deposition
APS	Advanced Photon Source
BM	Ball Mill/ Ball-Milling
BSE	Backscattered electron
CB	Conduction band
CESR	Cornell Electron Storage Ring
CLS	Canadian Light Source
CNPEM	Brazilian Center for Research in Energy and Materials
DESY	Deutsches Elektronen Synchrotron
DLSRs	Diffraction-limited storage rings
DOS	Density of states
EDX/EDS/EDXS	Energy dispersive X-ray spectroscopy
EHT	Electron high tension
EPD	Electrophoretic deposition
EPU	Elliptically polarizing undulator
ERL	Energy recovery linac
ESRF	European Synchrotron Radiation Facility
EXAFS	Extended x-ray absorption fine structure
FLY	Fluorescence yield
HALF	Hefei Advanced Light Facility
HASYLAB	Hamburger Synchrotronstrahlungslabor
HEG	High Energy Grating
HEPS	High Energy Photon Source
HOMO	Highest occupied molecular orbital
KE	Kinetic energy
LCF	Linear combination fitting
LINAC	Linear accelerator
LUMO	Lowest unoccupied molecular orbitals
LURE	Laboratoire pour l'Utilisation du Rayonnement Electromagnétique

NSLS	National Synchrotron Light Source
PXRD/XRD	Powder X-ray diffraction
REIXS	Resonant Elastic and Inelastic X-ray Scattering
RF	Radiofrequency
RIXS	Resonant Inelastic X-ray Scattering
SE	Secondary electrons
SEM	Scanning electronic microscopy
SFM	Surface Feet per Minute
SGM	Spherical Grating Monochromator
SLAC	Stanford Linear Accelerator Center
SRS	Synchrotron Radiation Source
TEM	Transmission electron microscope
TEY	Total electron yield
TPS	Taiwan Photon Sources
VB	Valance band
VBM	Valance band maximum
VLS-PGM	Variable-Line-Spacing Plane Grating Monochromator
VUV	Vacuum Ultraviolet
XAFS	X-ray absorption fine structure
XANES/XAS	X-ray absorption near edge spectrum
XEOL	X-ray excited optical luminescence
XES	X-ray Emission Spectroscopy
2D XEOL-XANES	Two-dimensional X-ray absorption near-edge structure-X-ray excited optical luminescence

Chapter 1

1. Introduction

1.1 Titanium dioxide (TiO_2), Zinc oxide (ZnO) and Tin dioxide (SnO_2)

For the first time in the history of humankind, human usage and pollution of water have reached a stage that might potentially restrict future food production, urban supplies, and ecosystem function.[1] The emerging global water crisis has suddenly caught worldwide attention. Freshwater is mainly contaminated by manufactured chemicals such as pesticides, dyes, and detergents.[2] The demand for more effective and affordable sustainable technology for wastewater treatment and controlling environmental pollution is increasing. All things considered, in the regions where the demand for water is not being met, wastewater treatment has been addressed as a probable method for this issue.

Heterogeneous photocatalysis is considered an effective process to address the degradation of organic pollutants in the air and water since it can eliminate and convert organic compounds into carbon dioxide, water, and inorganic anions since the pioneering work by Honda and Fujishima.[3,4] Semiconducting transition metal oxides are the most common and extensively characterized heterogeneous photocatalysts such as titanium dioxide (TiO_2), zinc oxide (ZnO) and Tin dioxide (SnO_2). Titanium dioxide and zinc oxide are transition-metal-oxide semiconductors, and they have similar performance in physicochemical properties, such as chemical and thermal stability, nontoxicity, and resistance to photo corrosion.[5–7] There are mainly four types of crystal structures in TiO_2, anatase, rutile, brookite, and TiO_2(B). Anatase and rutile TiO_2 are more popular research topics among the four different phases[8–11], and both belong to tetragonal crystal systems with distorted TiO_6 octahedra (as Fig. 1-1 shown), while the octahedra unit and shared edges are different. These differences in lattice structure cause differences in the electronic band structures and different band gaps. For anatase, the band gap is 3.20 eV, and the band gap for rutile is 3.02 eV[12,13]. Zinc Oxide is still a prominent study issue in today's scientific community due to its excellent performance in chemical stability, thermal conductivity, UV-protection properties and antibacterial.[14]

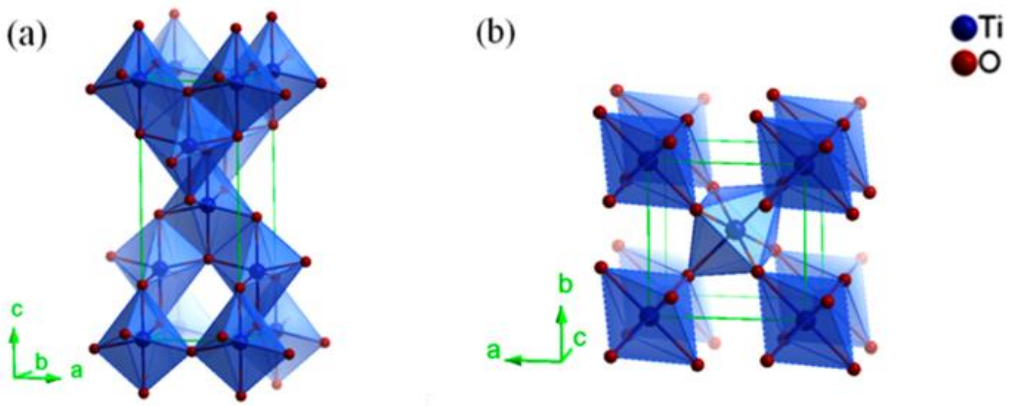

Figure 1-1. Crystal structure of a) anatase TiO_2 b) rutile TiO_2 [15]

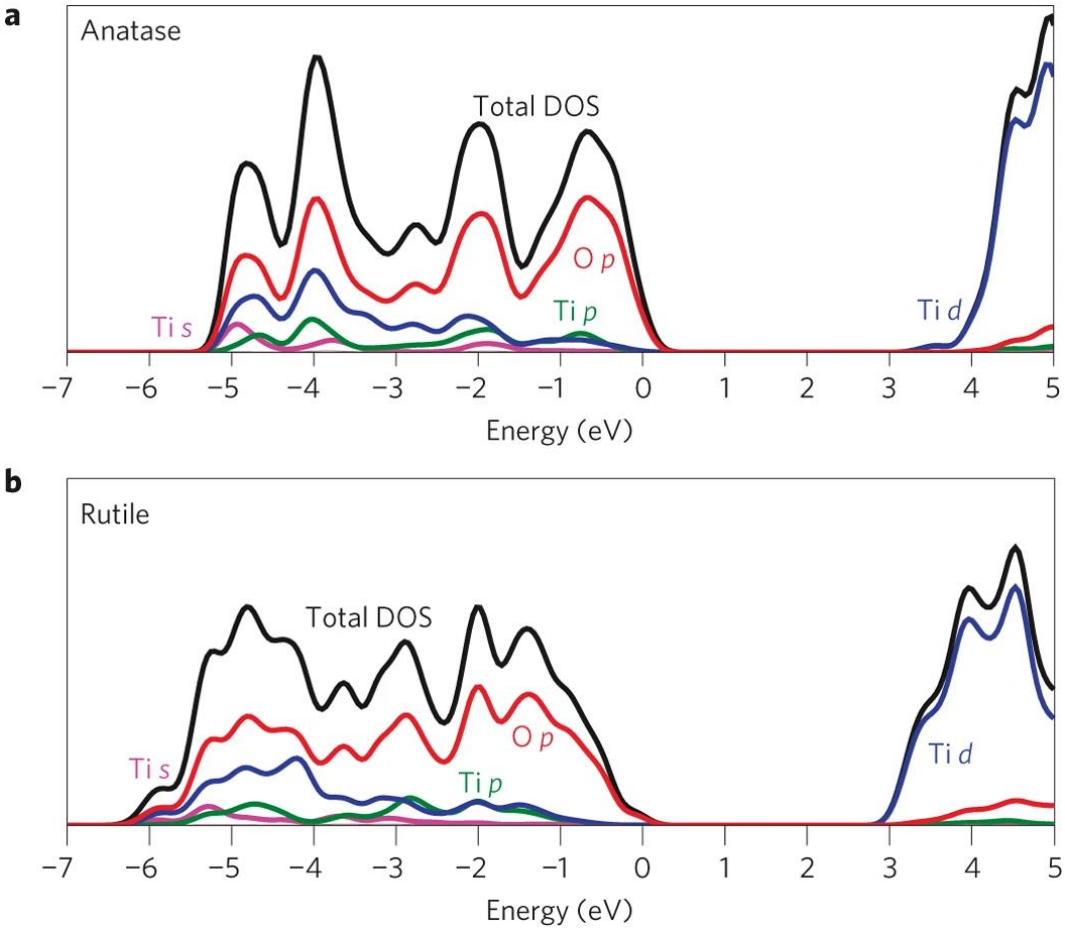

Figure 1-2. Calculated density of states (DOS) plots of a) anatase TiO_2 b) rutile TiO_2[16]

Figure 1-2 exhibits the calculated electronic density of states (DOS) of anatase and rutile TiO_2. The black line represents the total DOS, which is the cumulative contribution from all atoms and

orbitals in the system. And others represent the partial DOS. In the TiO_2, the main contributor is Oxygen 2p orbital (red line O p in Figure 1-2) in valance band (VB), and Titanium 3d orbital (blue line in Figure 1-2) in conduction band (CB).

Zinc Oxide (ZnO) is an essential II-VI semiconductor that is still a prominent study issue in today's scientific community. It is a widely used semiconductor material in the formation of optoelectronic devices[17], the usage in photoelectrochemical technologies[18], and high-power electronics[15]. It is an n-type semiconductor with a band gap of 3.37 eV (suitable for the UV region, UV and blue wavelength optoelectronic applications) and exciton binding energy of 60 meV[19]. Wurtzite (hexagonal) is the most stable phases at the room temperature (as shown in Figure 1-3). Zn atom is represented by yellow, and O atom is represented by grey. Both atoms exist in the tetrahedral coordination.

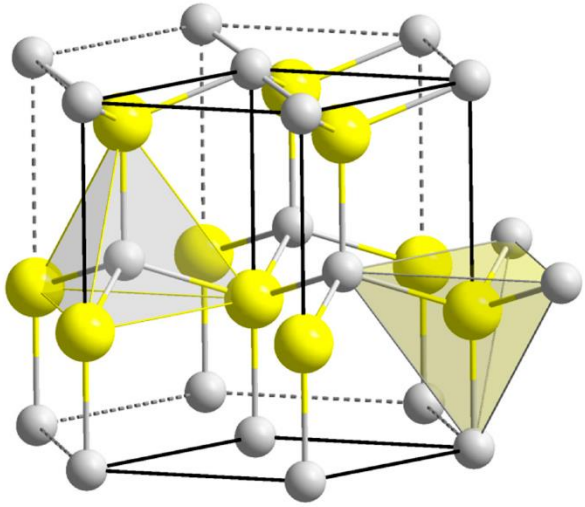

Figure 1-3. Crystal structure of ZnO, Zn atoms show in yellow, O atoms show in grey[20]

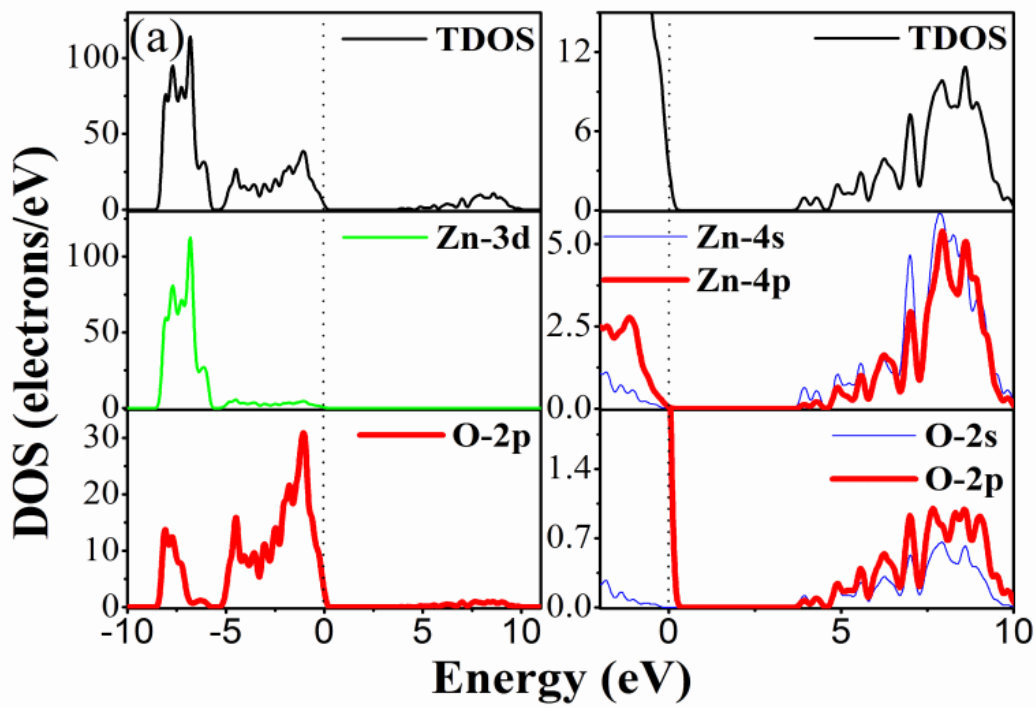

Figure 1-4. Calculated DOS plots of ZnO[21]

Figure 1-4 exhibits the calculated electronic DOS of ZnO. The top diagram represents the total DOS, and others represent the partial DOS. The lower energy range corresponds to the VB, and it is mainly composed of O 2p orbitals, while the higher energy range corresponds to the CB and it is mainly contributed by Zn 4s and 4p orbitals.

Tin Dioxide (SnO_2) is a significant wide band gap (3.7 eV) metal oxide and behaves as an n-type semiconductor, and it is the firmest oxides of tin in cassiterite mineral. Figure 1-5 illustrates the crystal structure of SnO_2, red balls are O atoms and purple balls are Sn atoms. Figure 1-6 exhibits the calculated DOS of SnO_2, it shows that the upper valence band (VB) is mainly composed of O(p) states, and the lower portion of the conduction band (CB) has an anti-bonding characteristic that originates from both Sn(4s) and O(p) states.

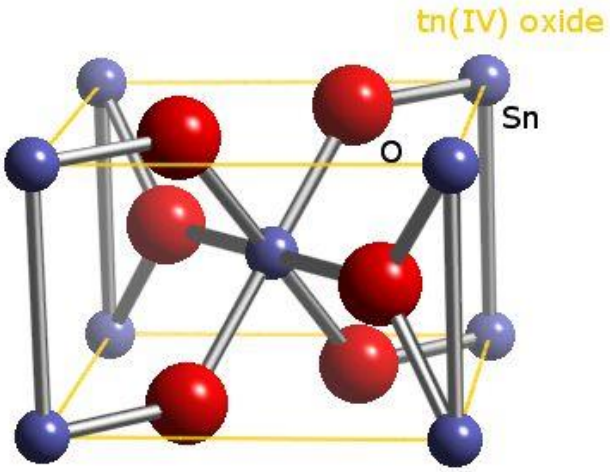

Figure 1-5. Crystal geometry of SnO_2, Sn atoms show in purple, O atoms shows in red[22]

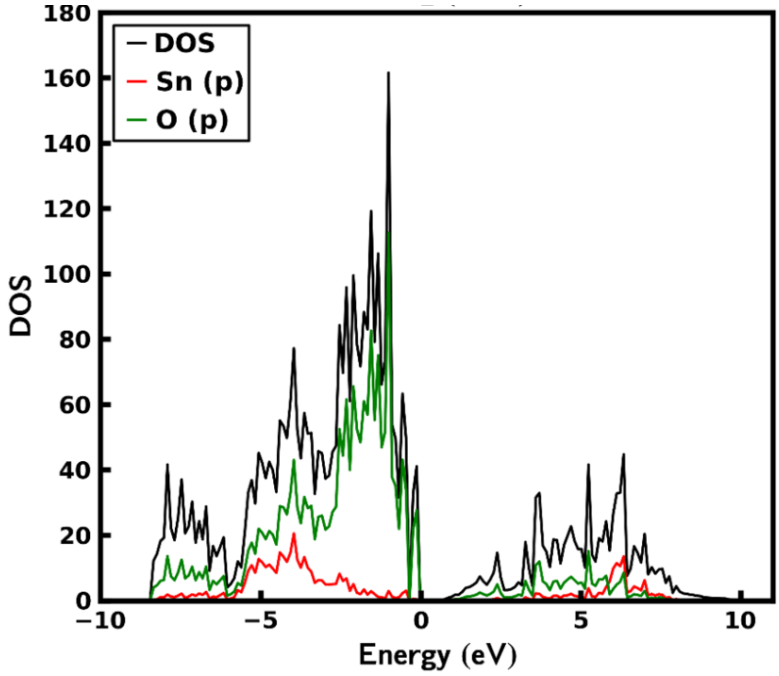

Figure 1-6. Calculated DOS plots of SnO_2[23]

1.2 Photocatalyst

A word 'photocatalyst' is formed by merging two terms – 'photo', relating to photons, and 'catalyst', which refers to the substance that modifies the reaction rate when it is present. Therefore, the material which can alter the chemical reaction and increase the rate when it exposure to the light is defined as photocatalysts[24]. Photocatalysis encompasses reactions that occur by exploiting

a semiconductor that absorbs visible light. In general, all solid can be defined according to their band gap: insulator, semiconductor, and conductor. As Figure 1-7 shown, in metals, there is an overlap between the valence and conduction bands, and it is a conductor. In contrast, in insulators, a significant gap (e.g.~10 eV) separates the electrons in the valence band from the conduction band. Semiconductors, on the other hand, have a relatively small gap between the valence and conduction bands (~ 1 - 4 eV), which allows the gap to be bridged by thermal or other excitations. Moreover, semiconductor can be separated into n-type semiconductor and p-type semiconductor. The n-type materials have electron energy levels situated close to the top of the band gap, which makes them readily excitable and able to enter the conduction band. Conversely, p-type materials have additional holes within the band gap that allow for valence band electrons to be excited, leaving behind mobile holes in the valence band.

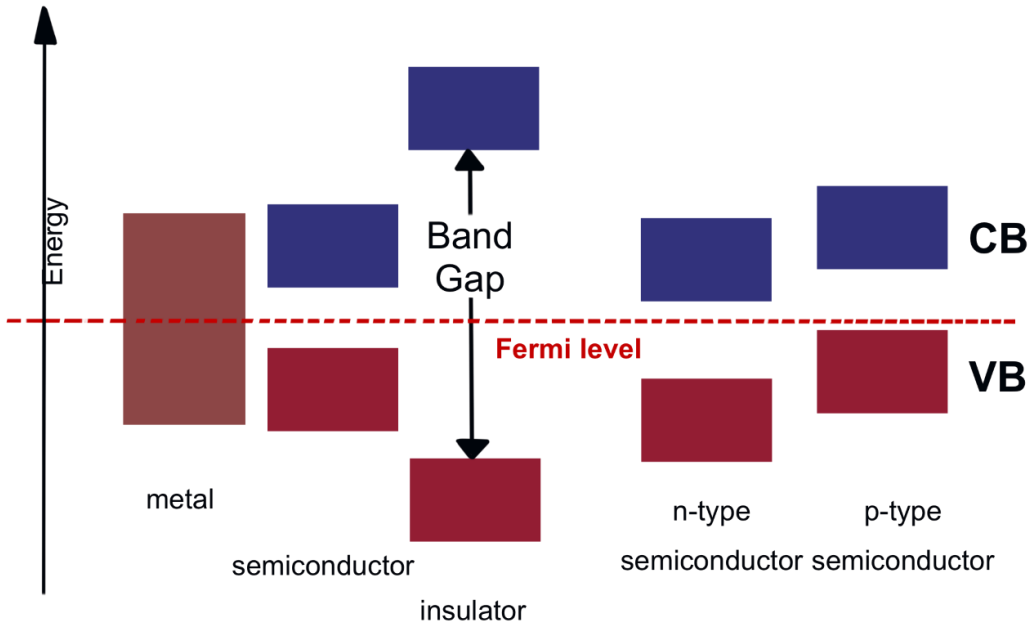

Figure 1-7. Classification of different materials

Figure 1-8 shows the photocatalytic reaction based on TiO_2. In the photocatalytic reaction, the creation of electronic holes (h^+) in the valance band (VB) and photoexcited (e^-) in the conduction band (CB) because of the light irradiation of electrons from the VB to CB. Spontaneously, in the presence of water the formation of OH· radicals and superoxide radicals ($O_2^{\cdot -}$) in the VB and CB, respectively, have been promoted. Both OH· and $O_2^{\cdot -}$ are involved in the elimination of organic

waste. Separating the photoexcited electrons and holes and reducing the recombination rate of e^-/h^+ pairs has become the main goal of photocatalyst studies in this context.[25,26]

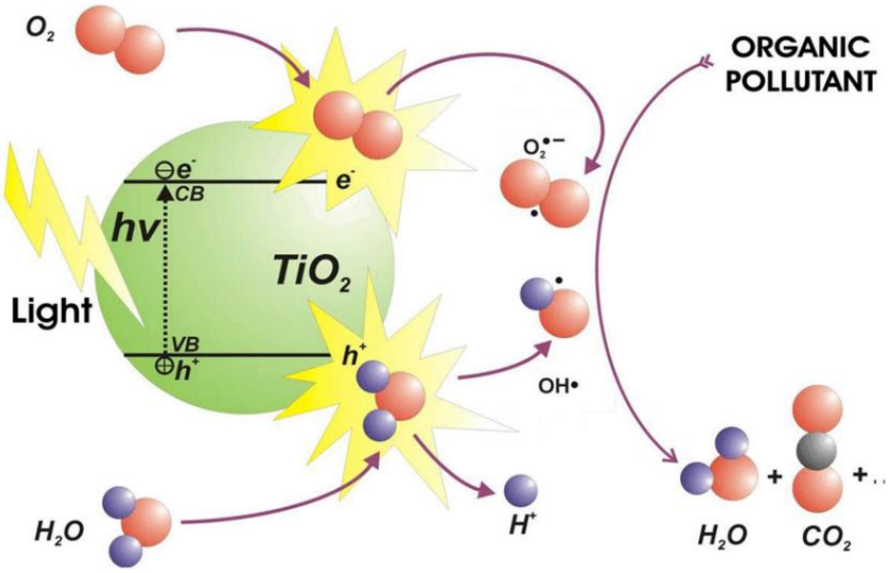

Figure 1-8. Photocatalytic reactions based on TiO_2 [27]

1.3 Synthesis methods of mixed-phase TiO_2

Prior investigations highlight that the photoactivity potential of single phased TiO_2 is considerably elevated when a mixed composition of anatase and rutile phases is present[28,29]. Importantly, this elevation in photoactivity is significantly noticeable in nanometer-scaled mixtures of TiO_2[28]. Such observations have inspired continued scientific study aimed at refining the structural characteristics of TiO_2, emphasizing the potential benefits of a mixed-phase approach. Generally, the transition from anatase to rutile phase occurs within a temperature range of 600°C to 700 °C[30]. Numerous techniques have been employed to modify this transition, such as metal oxide doping[31], hydrothermal methods[32], and chemical vapour deposition[33,34]. In the industry, ball-milling is widely used as an environmentally friendly approach for mechanochemical reaction[35]. Chapter 3 focuses following research investigates to optimize the mixed-phase approach by ball-milling method in nanometer-scaled TiO_2.

1.4 Synthesis methods of heterostructures

In previous studies, multiple methods have been applied to increase the recombination time of e^-/h^+ pairs including loading noble metals catalysts[36,37], doping transition metal ions[38], and forming heterostructures[39–41]. The enhanced properties of heterostructures have been proved by many

scientists[42,43]. This attention arises from their excellent development in properties, including distinctive surface morphology and unique charge transport mechanisms[44]. Heterostructure is defined as a semiconductor structure in which the chemical composition varies with position, and the interface between different chemical compositions is defined as a heterojunction[45]. The simplest heterostructure only contains one heterojunction. Covalent bonding, charge transfer, and orbital reconstruction processed alter the character and occupancy of d orbital at the interface heterojunction in transition-metal-oxide heterostructures.

Many approaches have been used to form heterostructures, including the electrophoretic deposition (EPD) technique[42], the hydrothermal method[41], the atomic layer deposition (ALD), and the ball milling[46]. To develop a sustainable, low-cost, and approachable method for synthesizing heterostructures, ball milling and atomic layer deposition reaped attention from scientists[47]. Therefore, Chapter 4 illustrates the synthesis of TiO_2/ZnO heterostructures by various methods can result in variations in the interface of the TiO_2/ZnO system.

1.5 Ball-Milling

Ball milling is utilized for the purpose of grinding various materials, such as mining ores, coal, pigments, and feldspar for pottery. Grinding can be conducted in either a wet or dry state. Ball milling is a mechanical technique widely used to grind samples into a smaller size in the industry field. During the ball milling process (as shown in Figure 1-9), the centrifugal forces produce the speed differences between balls and jars, creating friction and point collisions and releasing high pulverization energy (temperature and pressure), which can create pressure and temperature locally[48]. Ball milling can be used in the optimization of phase/structure composition. At the same time, ball milling is introduced as an eco-friendly synthetic method to start a mechanochemical reaction[35]. The Ball-Milling rate is closely related to Surface Feet per Minute (SFM) and its jar diameter.

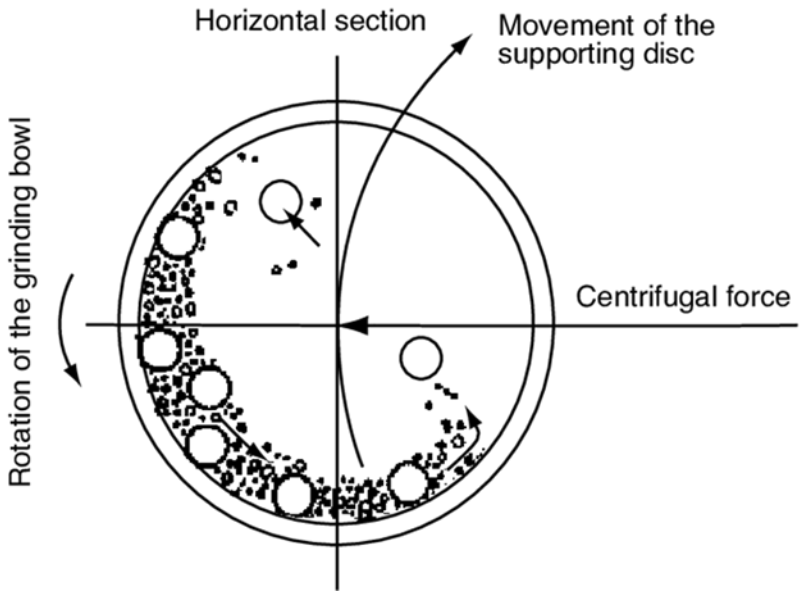

Figure 1-9. The schematic diagram of ball mill jar[48]

1.6 Thesis outline

In this project, I delineate the findings from our examination of these modifications, specifically detailing the impacts of ball-milling on the phase transition and heterostructure formation, as observed through the application of synchrotron radiation techniques.

The outline of this thesis is given below: Chapter 1 delivers the background of heterostructures, the synthesis of heterostructures via the ball-milling method, an overview of synchrotron radiation used in characterization, and the research objective of this thesis. Chapter 2 describes the characterization techniques of heterostructures: synchrotron techniques, including X-ray absorption near edge spectrum (XANES), X-ray Emission Spectroscopy (XES) and X-ray excited optical luminescence (XEOL); conventional techniques, including the powder X-ray diffraction (PXRD), energy dispersive X-ray spectroscopy (EDX), scanning electronic microscopy (SEM) and transmission electron microscope (TEM). Chapter 3 presents the TiO_2 phase transition in different ball milling rates. Chapter 4 illustrates a study of the X-ray absorption spectroscopy of heterostructures prepared from the ball-milling method of the phase transition of heterostructures. Moreover, it shows the effects of different ball-milling rates on products. Chapter 5 presents the summary and conclusions of this thesis and proposes future work.

1.5 Reference

1. Jury, W. A., Vaux, H. J. (2007). The emerging global water crisis: Managing scarcity and conflict between water users. Advances in Agronomy, 1–76. https://doi.org/10.1016/s0065-2113(07)95001-4
2. Li, N., Hu, Y., Lu, Y.-Z., Zeng, R. J., Sheng, G.-P. (2016). Multiple response optimization of the coagulation process for upgrading the quality of effluent from Municipal Wastewater Treatment Plant. Scientific Reports, 6(1). https://doi.org/10.1038/srep26115
3. Yang, B., Wang, J., Jiang, C., Li, J., Yu, G., Deng, S., Lu, S., Zhang, P., Zhu, C., Zhuo, Q. (2017). Electrochemical mineralization of perfluorooctane sulfonate by novel F and SB co-doped Ti/SnO_2 electrode containing Sn-Sb Interlayer. Chemical Engineering Journal, 316, 296–304. https://doi.org/10.1016/j.cej.2017.01.105
4. Peng, Y., Wang, K. K., Liu, T., Xu, J., Xu, B. G. (2017). Synthesis of one-dimensional Bi_2O_3-$Bi_2O_{2.33}$ heterojunctions with high interface quality for enhanced visible light photocatalysis in degradation of high-concentration phenol and Mo Dyes. Applied Catalysis B: Environmental, 203, 946–954. https://doi.org/10.1016/j.apcatb.2016.11.011
5. Tian, J., Chen, L., Dai, J., Wang, X., Yin, Y., Wu, P. (2009). Preparation and characterization of TiO_2, ZnO, and TiO_2/ZnO nanofilms via sol–gel process. Ceramics International, 35(6), 2261–2270. https://doi.org/10.1016/j.ceramint.2008.12.010
6. Debecker, D. P., Hulea, V., Mutin, P. H. (2013). Cheminform abstract: Mesoporous mixed oxide catalysts via non-hydrolytic sol-gel: A Review. ChemInform, 44(16). https://doi.org/10.1002/chin.201316207
7. Sanchez, C., Belleville, P., Popall, M., Nicole, L. (2011). Cheminform abstract: Applications of advanced hybrid organic-inorganic nanomaterials: From laboratory to market. ChemInform, 42(24). https://doi.org/10.1002/chin.201124253
8. Chen, X., Liu, L., Yu, P. Y., Mao, S. S. (2011). Increasing solar absorption for photocatalysis with black hydrogenated titanium dioxide nanocrystals. Science, 331(6018), 746–750. https://doi.org/10.1126/science.1200448
9. Ye, M., Gong, J., Lai, Y., Lin, C., Lin, Z. (2012). High-efficiency photoelectrocatalytic hydrogen generation enabled by palladium quantum dots-sensitized TiO_2 nanotube arrays. Journal of the American Chemical Society, 134(38), 15720–15723. https://doi.org/10.1021/ja307449z
10. Li, N., Hu, Y., Lu, Y.-Z., Zeng, R. J., Sheng, G.-P. (2016). Multiple response optimization of the coagulation process for upgrading the quality of effluent from Municipal Wastewater Treatment Plant. Scientific Reports, 6(1). https://doi.org/10.1038/srep26115
11. Su, D., Dou, S., Wang, G. (2015). Anatase Tio2: Better anode material than amorphous and rutile phases of TiO_2 for Na-Ion Batteries. Chemistry of Materials, 27(17), 6022–6029. https://doi.org/10.1021/acs.chemmater.5b02348
12. Choi, Y., Umebayashi, T., Yoshikawa, M. (2004). Fabrication and characterization of C-doped anatase TiO_2 photocatalysts. Journal of Materials Science, 39(5), 1837–1839. https://doi.org/10.1023/b:jmsc.0000016198.73153.31
13. Li, L., Yan, J., Wang, T., Zhao, Z.-J., Zhang, J., Gong, J., Guan, N. (2015). Sub-10 nm rutile titanium dioxide nanoparticles for efficient visible-light-driven photocatalytic hydrogen production. Nature Communications, 6(1). https://doi.org/10.1038/ncomms6881
14. Kołodziejczak-Radzimska, A., Jesionowski, T. (2014). Zinc oxide—from synthesis to application: A Review. Materials, 7(4), 2833–2881. https://doi.org/10.3390/ma7042833

15. Ma, Y., Wang, X., Jia, Y., Chen, X., Han, H., Li, C. (2014). Titanium dioxide-based nanomaterials for photocatalytic fuel generations. Chemical Reviews, 114(19), 9987–10043. https://doi.org/10.1021/cr500008u
16. Scanlon, D. O., Dunnill, C. W., Buckeridge, J., Shevlin, S. A., Logsdail, A. J., Woodley, S. M., Catlow, C. R., Powell, Michael. J., Palgrave, R. G., Parkin, I. P., Watson, G. W., Keal, T. W., Sherwood, P., Walsh, A., Sokol, A. A. (2013). Band alignment of Rutile and anatase TiO_2. Nature Materials, 12(9), 798–801. https://doi.org/10.1038/nmat3697
17. Shi, J., Zhang, J., Yang, L., Qu, M., Qi, D., Zhang, K. H. (2021). Wide bandgap oxide semiconductors: From materials physics to optoelectronic devices. Advanced Materials, 33(50). https://doi.org/10.1002/adma.202006230
18. Chen, D., Zou, X., Dong, F., Zhen, C., Xiao, D., Wang, X., Wu, Q., Cao, Y., Tu, J. (2021). Donor–acceptor compensated ZnO semiconductor for photoelectrochemical biosensors. ACS Applied Materials Interfaces, 13(28), 33006–33014. https://doi.org/10.1021/acsami.1c07499
19. Özgür, Alivov, Ya. I., Liu, C., Teke, A., Reshchikov, M. A., Doğan, S., Avrutin, V., Cho, S.-J., Morkoç, H. (2005). A comprehensive review of ZnO materials and Devices. Journal of Applied Physics, 98(4). https://doi.org/10.1063/1.1992666
20. Borysiewicz, M. A. (2019). ZnO as a functional material, a review. Crystals, 9(10), 505. https://doi.org/10.3390/cryst9100505
21. Wu, H.-C., Peng, Y.-C., Shen, T.-P. (2012). Electronic and optical properties of substitutional and interstitial si-doped ZnO. Materials, 5(11), 2088–2100. https://doi.org/10.3390/ma5112088
22. Mark Winter, U. of S. and W. L. (n.d.). Tin dioxide. WebElements Periodic Table " Tin " tin dioxide. https://www.webelements.com/compounds/tin/tin_dioxide.html
23. Griego, C. D., Saravanan, K., Keith, J. (2018). Benchmarking Computational Alchemy for Carbide, Nitride, and Oxide Catalysts. https://doi.org/10.26434/chemrxiv.7122089
24. Ameta, R., Solanki, M. S., Benjamin, S., Ameta, S. C. (2018). Photocatalysis. Advanced Oxidation Processes for Waste water Treatment, 135–175. https://doi.org/10.1016/b978-0-12-810499-6.00006-1
25. Linsebigler, A. L., Lu, G., Yates, J. T. (1995). Photocatalysis on TiO_2 surfaces: Principles, mechanisms, and selected results. Chemical Reviews, 95(3), 735–758. https://doi.org/10.1021/cr00035a013
26. Samokhvalov, A. (2017). Hydrogen by photocatalysis with nitrogen codoped titanium dioxide. Renewable and Sustainable Energy Reviews, 72, 981–1000. https://doi.org/10.1016/j.rser.2017.01.024
27. Ibhadon, A., Fitzpatrick, P. (2013). Heterogeneous photocatalysis: Recent advances and applications. Catalysts, 3(1), 189–218. https://doi.org/10.3390/catal3010189
28. Ohno, T., Tokieda, K., Higashida, S., Matsumura, M. (2003). Synergism between rutile and anatase TiO_2 particles in photocatalytic oxidation of naphthalene. Applied Catalysis A: General, 244(2), 383–391. https://doi.org/10.1016/s0926-860x(02)00610-5
29. Jia, J., Ohno, T., Matsumura, M. (2000). Efficient dihydroxylation of naphthalene on photo irradiated rutile TiO_2 powder in solution containing hydrogen peroxide. Chemistry Letters, 29(8), 908–909. https://doi.org/10.1246/cl.2000.908
30. Byrne, C., Fagan, R., Hinder, S., McCormack, D. E., Pillai, S. C. (2016). New approach of modifying the anatase to rutile transition temperature in TiO_2 photocatalysts. RSC Advances, 6(97), 95232–95238. https://doi.org/10.1039/c6ra19759k

31. Pillai, S. C., Periyat, P., George, R., McCormack, D. E., Seery, M. K., Hayden, H., Colreavy, J., Corr, D., Hinder, S. J. (2007). Synthesis of high-temperature stable anatase TiO_2 photocatalyst. The Journal of Physical Chemistry C, 111(4), 1605–1611. https://doi.org/10.1021/jp065933h
32. Sun, B., Vorontsov, A. V., Smirniotis, P. G. (2003). Role of platinum deposited on TiO_2 in phenol photocatalytic oxidation. Langmuir, 19(8), 3151–3156. https://doi.org/10.1021/la0264670
33. Mills, A., Elliott, N., Parkin, I. P., O'Neill, S. A., Clark, R. J. (2002). Novel TiO_2 CVD films for semiconductor photocatalysis. Journal of Photochemistry and Photobiology A: Chemistry, 151(1–3), 171–179. https://doi.org/10.1016/s1010-6030(02)00190-9
34. Goossens, A., Maloney, E.-L., Schoonman, J. (1998). Gas-phase synthesis of nanostructured anatase TiO_2. Chemical Vapor Deposition, 04(03), 109–114. https://doi.org/10.1002/(sici)1521-3862(199805)04:03<109::aid-cvde109>3.0.co;2-u
35. Ban, V., Sadikin, Y., Lange, M., Tumanov, N., Filinchuk, Y., Černý, R., Casati, N. (2017). Innovative in situ ball mill for X-ray diffraction. Analytical Chemistry, 89(24), 13176–13181. https://doi.org/10.1021/acs.analchem.7b02871
36. Vaishampayan, M. V., Deshmukh, R. G., Mulla, I. S. (2008). Influence of PD doping on morphology and LPG response of SnO_2. Sensors and Actuators B: Chemical, 131(2), 665–672. https://doi.org/10.1016/j.snb.2007.12.055
37. Tao, W.-H., Tsai, C.-H. (2002). H2S sensing properties of noble metal doped WO_3 thin film sensor fabricated by micromachining. Sensors and Actuators B: Chemical, 81(2–3), 237–247. https://doi.org/10.1016/s0925-4005(01)00958-3
38. Li, X., Chang, Y., Long, Y. (2012). Influence of SN doping on ZnO sensing properties for ethanol and acetone. Materials Science and Engineering: C, 32(4), 817–821. https://doi.org/10.1016/j.msec.2012.01.032
39. Miller, D. R., Akbar, S. A., Morris, P. A. (2014). Nanoscale metal oxide-based heterojunctions for Gas Sensing: A Review. Sensors and Actuators B: Chemical, 204, 250–272. https://doi.org/10.1016/j.snb.2014.07.074
40. Zhang, Z., Xu, M., Liu, L., Ruan, X., Yan, J., Zhao, W., Yun, J., Wang, Y., Qin, S., Zhang, T. (2018). Novel SnO_2@ZnO hierarchical nanostructures for highly sensitive and selective NO2 gas sensing. Sensors and Actuators B: Chemical, 257, 714–727. https://doi.org/10.1016/j.snb.2017.10.190
41. Yang, X., Zhang, S., yu, Q., Zhao, L., Sun, P., Wang, T., Liu, F., Yan, X., Gao, Y., Liang, X., Zhang, S., Lu, G. (2019). One step synthesis of branched SnO_2/ZnO heterostructures and their enhanced gas-sensing properties. Sensors and Actuators B: Chemical, 281, 415–423. https://doi.org/10.1016/j.snb.2018.10.138
42. Testoni, G. O., Amoresi, R. A. C., Lustosa, G. M. M. M., Costa, J. P. C., Nogueira, M. V., Ruiz, M., Zaghete, M. A., & Perazolli, L. A. (2018). Increased photocatalytic activity induced by TiO_2/Pt/SnO_2 heterostructured films. *Solid State Sciences*, *76*, 65–73. https://doi.org/10.1016/j.solidstatesciences.2017.12.006
43. Yu, Q., Zhu, J., Xu, Z., Huang, X. (2015). Facile synthesis of α-Fe_2O_3@SnO_2 core–shell heterostructure nanotubes for high performance gas sensors. Sensors and Actuators B: Chemical, 213, 27–34. https://doi.org/10.1016/j.snb.2015.01.130
44. Theerthagiri, J., Chandrasekaran, S., Salla, S., Elakkiya, V., Senthil, R. A., Nithyadharseni, P., Maiyalagan, T., Micheal, K., Ayeshamariam, A., Arasu, M. V., Al-

Dhabi, N. A., Kim, H.-S. (2018). Recent developments of metal oxide-based heterostructures for photocatalytic applications towards environmental remediation. Journal of Solid State Chemistry, 267, 35–52. https://doi.org/10.1016/j.jssc.2018.08.006
45. Xu, F., Meng, K., Cheng, B., Wang, S., Xu, J., Yu, J. (2020). Unique S-scheme heterojunctions in self-assembled TiO_2/CSPBBR3 hybrids for CO_2 photoreduction. Nature Communications, 11(1). https://doi.org/10.1038/s41467-020-18350-7
46. Wang, Y., Yu, J., Peng, W., Tian, J., Yang, C. (2019). Novel multilayer TiO_2 heterojunction decorated by low G-C_2N_4 content and its enhanced photocatalytic activity under UV, visible and solar light irradiation. Scientific Reports, 9(1). https://doi.org/10.1038/s41598-019-42438-w
47. de los Santos, D. M., Navas, J., Sánchez-Coronilla, A., Alcántara, R., Fernández-Lorenzo, C., Martín-Calleja, J. (2015). Highly al-doped TiO_2 nanoparticles produced by Ball Mill Method: Structural and Electronic Characterization. Materials Research Bulletin, 70, 704–711. https://doi.org/10.1016/j.materresbull.2015.06.008
48. Baheti, V., Abbasi, R.,Militky, J. (2012). Ball milling of jute fibre wastes to prepare nanocellulose. World Journal of Engineering, 9(1), 45–50. https://doi.org/10.1260/1708-5284.9.1.45

Chapter 2

2. Instrument and Techniques

2.1 Synchrotron radiation facilities and beamlines

2.1.1 Synchrotron Overview

Synchrotron radiation is electromagnetic radiation produced by relativistic electrons (speed close to light) emitted when it moves and accelerates along an arc-shaped magnetic field. It is named synchrotron radiation because this change has to be synchronized with the enhancement of energy acquired through the increase in the speed of particles[1].

Synchrotron technology has gone through three generations of development. We are now on the verge of moving into the 4th generation and have become widely accessible for users of diverse disciplines.

The first-generation, Tantalus I with storage ring was the first operated synchrotron light source in 1968 and obtained the first spectrum in Wisconsin. The first storage ring was designed by Mills and Rowe, and it only has an energy of 240 MeV and a circumference of 9.38 m. There were 10 fine beamlines completed in the following years and equipped with monochromators, which became the model of the modern Synchrotron Center. Shortly thereafter, there was a notable increase in attention towards storage rings. The Orsay laboratory in France initiated synchrotron radiation studies on the 540 MeV ACO storage ring in 1971. In 1974, the Stanford Synchrotron Radiation Project founded the 2.5 GeV SPEAR ring in the Stanford Linear Accelerator Center (SLAC). Moreover, the 3.5-GeV DORIS ring is located at Deutsches Elektronen Synchrotron (DESY), and the 5.6-GeV Cornell Electron Storage Ring (CESR) is situated at Cornell University (the CHESS facility)[2]. All the first-generation Synchrotron Centers were operated in a parasitic mode under low beam currents and low beam energies with limited output of synchrotron radiation.

The second-generation was designed to provide more dedicated synchrotron radiation by utilizing electrons (positrons) as the charged particles confined in the storage ring instead of colliders high energy physics experiments. The first installation of an improved storage ring (2 GeV) appeared in Synchrotron Radiation Source (SRS) at the Daresbury Laboratory. More new Synchrotron Centers were established in the following years. For example, the National Synchrotron Light

Source (NSLS) at the Brookhaven National Laboratory in 1981; the Photon Factory at the KEK laboratory in 1982 in Tsukuba, Japan; the BESSY facility in Berlin; and the Laboratoire pour l'Utilisation du Rayonnement Electromagnétique (LURE) in Orsay. In other locations, first-generation Synchrotron centers were gradually transformed into second-generation through enhancements and arrangements made with laboratory management to allocate a portion. Such as the Stanford Synchrotron Radiation Laboratory at SLAC and Hamburger Synchrotronstrahlungslabor (HASYLAB) at DESY.

The third-generation optimizes the brightness by adding undulators and wigglers to accelerate the electrons. The whole electromagnetic spectrum can be emitted from synchrotron radiation. Then the spectra can be separated by different ranges from the beamlines. At the experimental station, scientists can choose specific parts of the spectrum (e.g. IR to X-rays) to conduct their experiment.

Figure 2-1 shows the schematic diagram of a typical synchrotron radiation facility. Firstly, the linear accelerator (LINAC) accelerated the emitted electron from a heated cathode (the injection system) to a high speed. Then, high-speed electrons were injected into the booster ring and accelerated to 99.9999985% of the speed of light. The vacuumed storage ring can keep the high-speed electron beam circulating for many hours. To avoid electron loss due to scattering from gas atoms, the vacuum chamber is essential. Besides that, the turning sections were equipped with bending magnets to control the direction of electron beams. The radiofrequency (RF) cavity provides an oscillating electromagnetic to compensate for the energy loss of electron beams. Moreover, in a synchrotron facility, there are many beamlines, each optimized for a specific field of research. Each beamline is accompanied by an experimental endstation, the facility-user interface where users can have their input on how the experiment can be conducted.

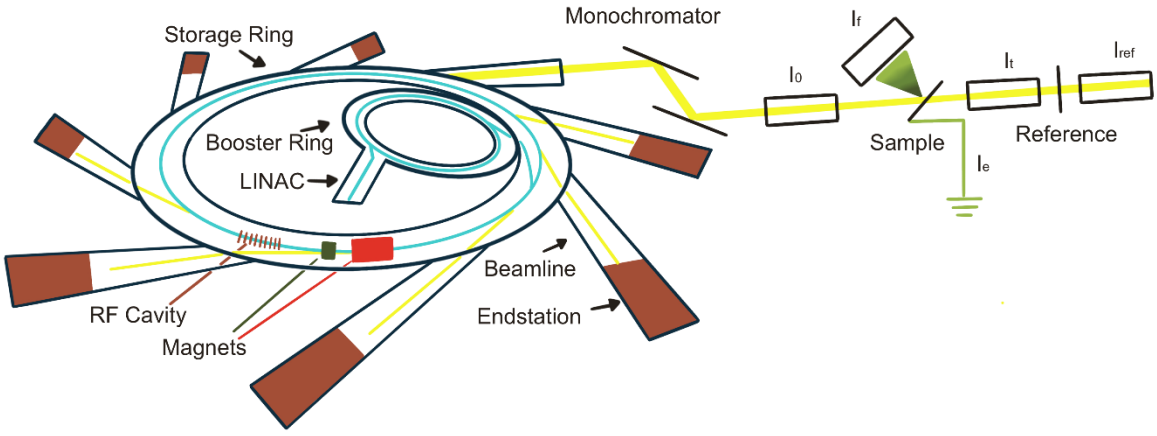

Figure 2-1. The diagram of a typical synchrotron radiation facility. The blue lines stand for the electron path. The yellow lines stand for synchrotron radiation.

The first of the third-generation is the European Synchrotron Radiation Facility (ESRF) in Grenoble with a 6 GeV storage ring in 1994. Later, more third-generation Synchrotron facilities were established. In 1996, the Advanced Photon Source (APS) at Argonne National Laboratory with 7 GeV storage ring. In 1997, the Spring-8 (8 GeV) in Harima Science Garden City in Japan. And The Canadian Light Source (CLS) in Saskatoon, Canada in 2002.

The next-generation is developed in the diffraction-limited storage rings (DLSRs)[3], the Energy recovery linac (ERL)[4], and the X-ray free-electron lasers (x-ray FELs)[5]. And the fourth-generation facility is based on the DLSRs and firstly found the MAX IV in Sweden[6]. Subsequently, more countries and regions initiated the construction of the fourth-generation. Such as, the APS-U at Argonne National Laboratory in United States[7], the Sirius, is designed by the Brazilian Center for Research in Energy and Materials (CNPEM) in Brazil[8], and High Energy Photon Source (HEPS) and Hefei Advanced Light Facility (HALF) in China.

It should be noted that each generation of development leads to a brighter and faster pulse synchrotron beam allowing for investigating the structure and functionality of matter in unprecedent details. We are now in the transition periods of 3rd to 4th generation. I will describe below the beamlines where I conducted my experiments for this thesis work

2.1.2 Canadian Light Source (CLS)

The Canadian Light Source (CLS) is a 3rd generation synchrotron light source in Saskatoon, Saskatchewan, Canada. The storage ring energy of CLS is 2.9 GeV at a current of around 250 mA in the accelerator with a lifetime of approximately 20 hours[9]. Figure 2-2 shows the schematic diagram of the Canadian Light Source. Currently, there are 20 beamlines available in CLS, which can cover energy range from Far-IR to hard X-ray.

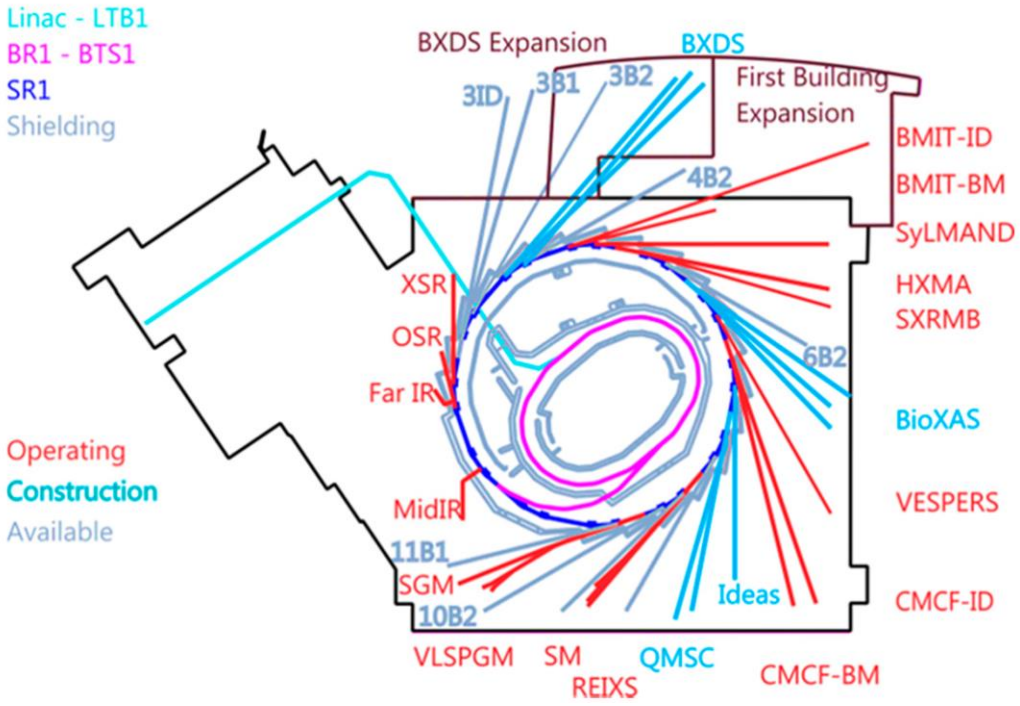

Figure 2-2. The schematic diagram of the Canadian Light Source (CLS)[9].

2.1.2.1 Spherical Grating Monochromator (SGM) Beamline

The spherical grating monochromator (SGM) Beamline (11ID-1) at CLS uses an elliptically polarizing undulator as the beam source within resolution(E/ΔE) of 5000 and the photon energy range of 250-2000 eV, which is suitable for measurement of the L-edge of transition metal and the K-edge of low-Z elements. Figure 2-3 illustrates the configuration of the SGM beamline, revealing the presence of a dragon-type monochromator at the beamline. Three gratings are available for selecting the desired energy range: a low-energy grating covering 250-700 eV, a medium-energy grating spanning 450-1250 eV, and a high-energy grating ranging from 740-2000 eV. There are two in-line endstations: high resolution x-ray absorption spectroscopy and photoelectron

spectroscopy are supplied in SGM. EA1 is specifically designed for photoemission investigations, while EA2 is intended for X-ray absorption measurements.

The light source is generated from a 45 mm planar undulator, which is channeled to the experimental section via two horizontal deflecting mirrors and a single vertical focusing mirror, projecting toward the entrance slit and subsequently onto the chosen grating. Three gratings are equipped in SGM featuring line spacing of 600, 1100, and 1700 lines/mm. Two toroidal refocusing mirrors are used to concentrate the beam onto the sample regions. The sample is situated in a vacuumed chamber at the endstation.

In this project, the XANES and related XEOL data of Ti $L_{3,2}$-edge, Zn $L_{3,2}$-edge, Sn $M_{5,4}$-edge and O K-edge can be collected from SGM beamline.

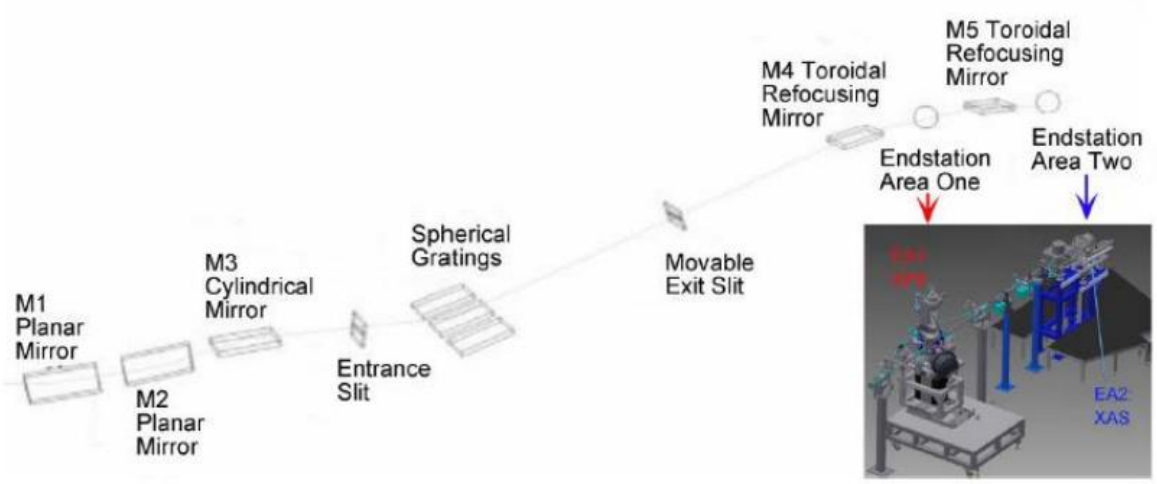

Figure 2-3. The schematic diagram of the SGM beamline[10]

2.1.2.2 Resonant Elastic and Inelastic X-ray Scattering (REIXS) Beamline

There are two endstations in REIXS beamline: RSXS endstation and RIXS endstation. In this project, RIXS endstation is selected for the experiment. In the RIXS endstation, there are X-ray Emission Spectroscopy (XES), Resonant Inelastic X-ray Scattering (RIXS) and X-ray Absorption Spectroscopy (XAS/XANES) techniques are equipped. The energy range of REIXS beamline is from 95 to 2000 eV with a resolution of 5×10^{-5} at 100 eV, and 1.3×10^{-4} at 1000 eV. Two common

elliptically polarizing undulator (EPU) are equipped in this beamline: horizontal polarization and vertical polarization. In this project, the horizontal polarization undulator serves as the light source. Furthermore, the Variable-Line-Spacing Plane Grating Monochromator (VLS-PGM) can be adjusted between a Carbon Mirror with Au LEG (Low Energy Grating) grating, a Nickel mirror with Ni LEG grating and a Silicon mirror with Au HEG (High Energy Grating) grating in energy ranging of 100-250 eV, 200-750 eV and 350-1500 eV, respectively. For further setting up of the XES spectrometer, another grating must be selected based on energy to be measured: XLEG (<200 eV), LEG (180~750 eV), MEG (260 eV~750 eV) and HEG (600~1000 eV). It should be noted that the grating of higher energy invariably exhibits superior resolution. Finally, the X-ray electron beam targets the samples, which are mounted on copper or carbon tapes and placed in the vacuumed chamber at the RIXS endstation.

In this project, the XANES and related XES data of Ti $L_{3,2}$-edge can be collected from REIXS beamline.

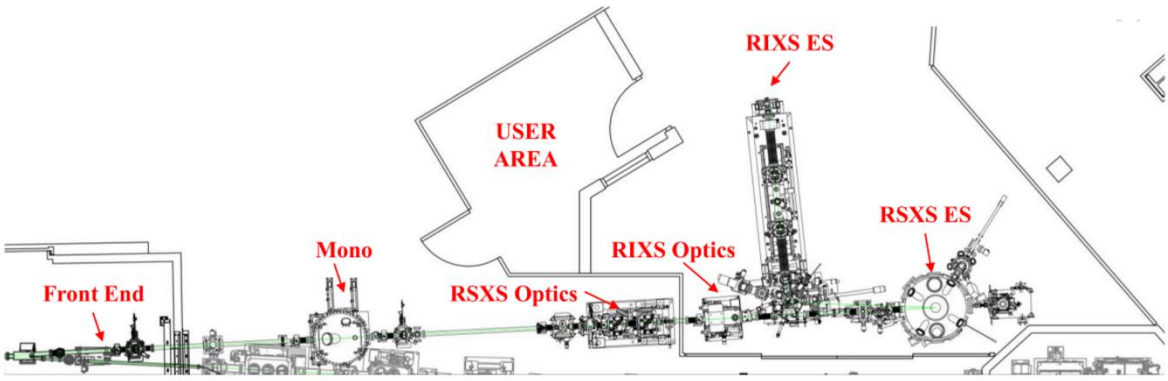

Figure 2-4. The schematic diagram of the REIXS beamline[11]

2.1.3 Taiwan Photon Source (TPS)

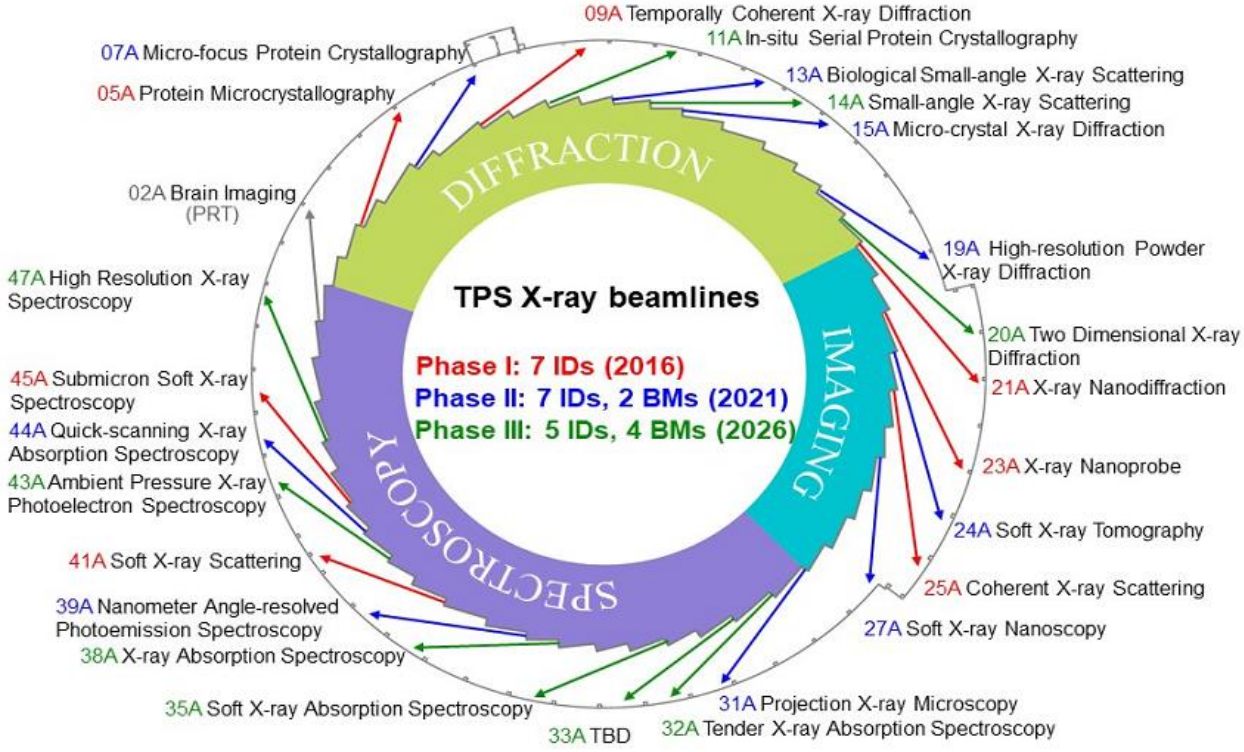

Figure 2-5. The schematic diagram of the TPS[12].

Taiwan Photon Source (TPS) is a 3rd generation synchrotron light source in Hsinchu, Taiwan. The storage ring energy of TPS is 3-3.3 GeV with 518m circumference. Figure 2-5 shows the schematic diagram of the TPS. The TPS possesses a potential capacity of approximately 40 beamlines, among which 7 from Phase-I and 9 from Phase-II are presently available for users while Phase-III is under construction and will finish around 2026.

In this project, Beamline 19A High resolution Powder Diffraction (HRPXRD) was employed for XRD data collection. Its strategic design facilitates the comprehensive examination of molecular structures across varied sample environment.

2.2 Synchrotron-based technique

2.2.1 The X-ray absorption fine structure (XAFS)

XAS is an element-, chemical- and site-specific technique; it can focus on one element from a sample containing various elements. It is widely used to explore electronic states and local atomic structures. When the high-energy X-ray strikes an atom, if the photon has enough energy, it will be absorbed, and a core electron is excited to an unoccupied state and if the energy is sufficient to excite the core electron into the continuum, it is called the absorption threshold or the absorption edge, above the edge, it produces photoelectrons[13]. When the photoelectron is originated from the 1s orbital (K-shell), the sharp absorption discontinuity is identified as K-edge. Similarly, when the photoelectron originated from 2s or 2p core-level (L-shell), it is called L-edge, and so on[14]. In the L-edge spectrum, there are one peaks at the L_2 edge and two prominent peaks at the L_2 and L_3 edge [15], which represent that the core-electron is originally excited from $2p_{1/2}$ and $2p_{2/3}$ orbitals, respectively.

$$\frac{I_t}{I_0} = e^{-\mu t} \quad \textbf{(Equation 2-1)}$$

Beer-Lambert Law (**Equation 2-1**) can be applied to calculate the relationship between the intensity of the transmitted X-ray (I_t) and incident X-ray (I_0), where μ is the linear absorption Coefficient in cm^{-1} and t is the sample thickness in cm. When the photon energy is adequate to excite a core electron (core electron is excited to an unoccupied state, such as an unoccupied bond state, a quasi-bound state, or the continuum), the μ increases dramatically and shows as an sharpen edge jump in the absorption coefficient and then degraded progressively until reaching the next absorption edge, details is showed on Figure 2-6.

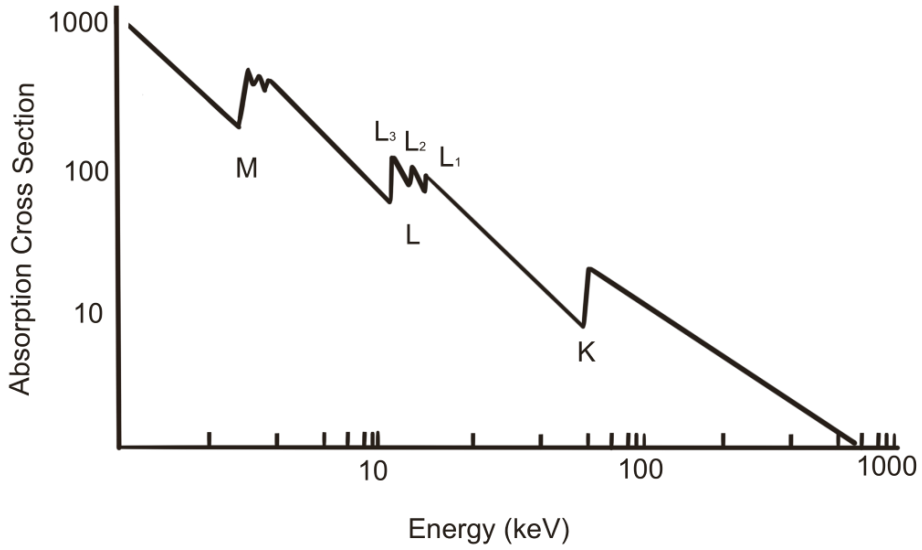

Figure 2-6. X-ray absorption cross section (cm^2g^{-1}) of Pt as a function of X-ray photon energy (keV)

The μ can be expressed as **Equation 2-2**, where the σ stands for mass absorption cross-section (cm^2g^{-1}), ρ stands for sample density (g/cm^3), Z stands for atomic number, A stands for atomic mass (g), and E stands for X-ray energy.

$$\mu = \sigma \cdot \rho \approx \frac{\rho Z^4}{AE^3} \textbf{ (Equation 2-2)}$$

The **Equation 2-2** clearly shows that μ is significantly correlated with A and Z, which designate the XAS is an element-specific measured technique. Besides that, figure 2-5 illustrates the plot of absorption cross-section versus X-ray energy (keV) in Platinum (Pt), and there are three main transitions were shown, M-edge, L-edge (L_3, L_2, and L_1), and K-edge.

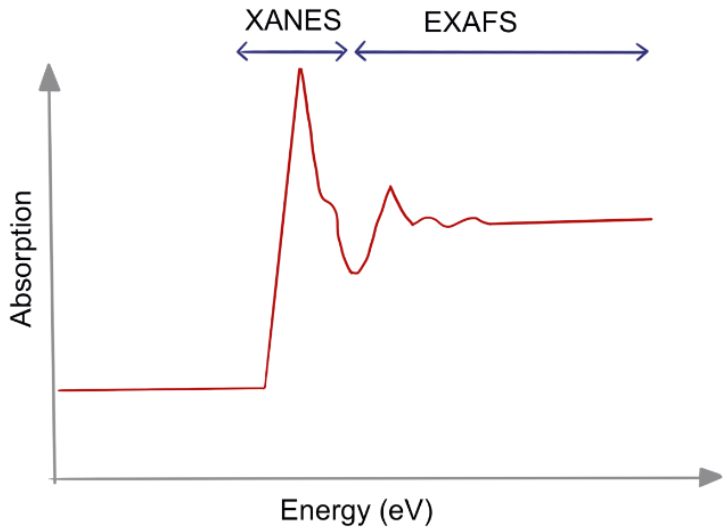

Figure 2-7. Schematic of an X-ray absorption spectrum

The X-ray absorption spectrum can be separated into two parts, X-ray absorption near edge spectrum (XANES, 20 eV-50 eV, below and above the absorption edge, also referred as Near Edge X-ray Absorption Fine Structures), and extended x-ray absorption fine structure (EXAFS, 50 eV-1000 eV, above the edge), as figure 2-6 shows below. Generally, in the soft X-ray beamlines only the XANES spectrum can be collected since the energy is close to the edges. The premium factor to distinguish XANES and EXAFS is the different electron scattering behaviors with various kinetic energy. Photoelectrons with the low kinetic energy (KE) are scattered by valence electrons, undergoes multiple scattering in a molecular environment and dominantly contribute to the XANES. In contract, photoelectrons with the high KE are scattered by core electrons, and they favor single scattering along the bond, and dominantly contribute to the EXAFS. Figure 2-7 shows the schematic illustration of different scattering pathways.

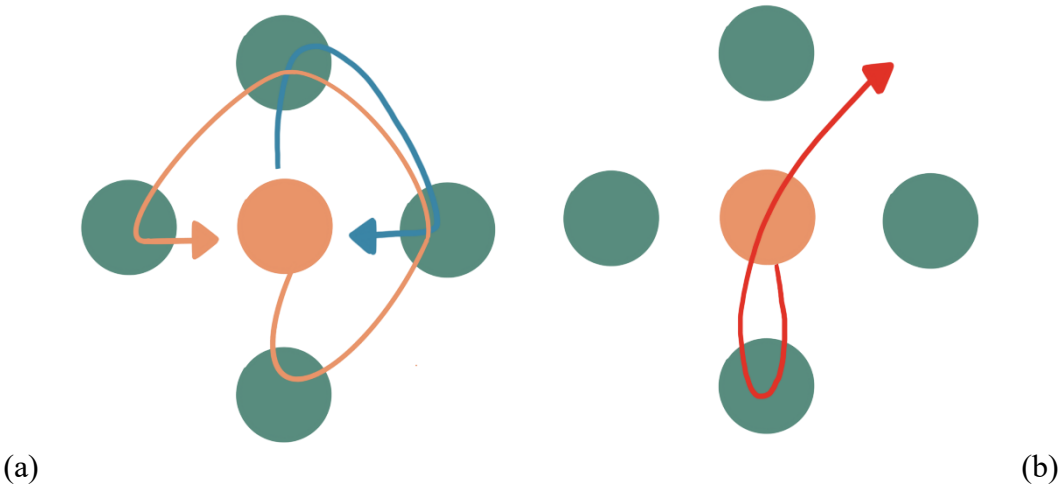

Figure 2-8. Schematic illustration of (a) multiple scattering with low kinetic energy (b) single scattering with high kinetic energy

From the XANES, electronic and geometric information can be obtained, such as ligand-field, spin-state, and centrosymmetry and the unoccupied densities of state (DOS) of different angular momentum character due to dipole transition. The EXAFS focuses on the radial probability distribution of electron density close to the absorbing atom, which can be used to determine the bond length and coordination numbers and analyzed quantitatively. In general, the XANES and EXAFS are analyzed separately.

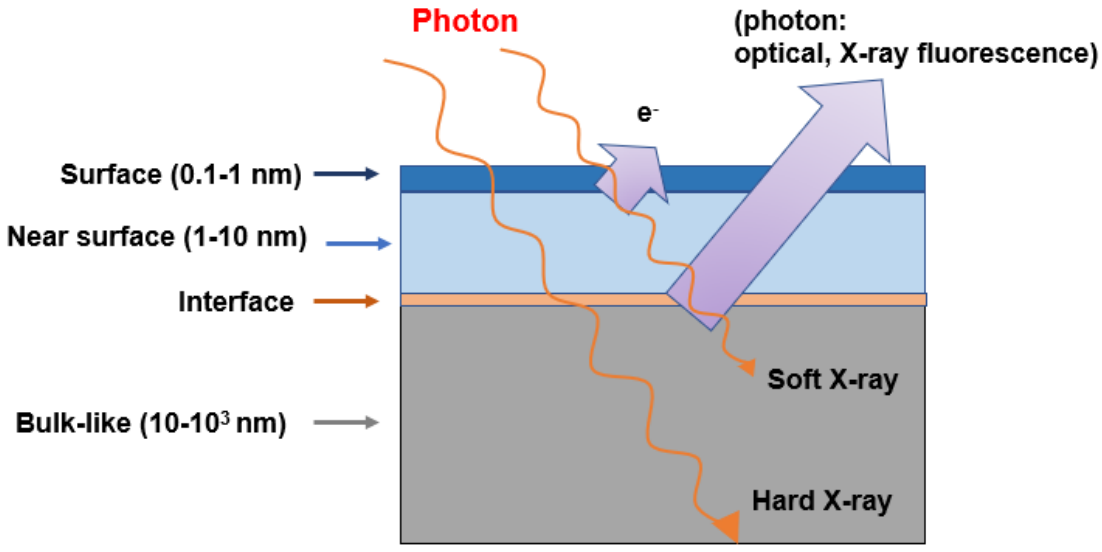

Figure 2-9. X-ray probing depth in different energy

Commonly, X-ray can be sorted by different energy, such as Vacuum Ultra Violet (VUV, 30-200 eV), soft X-rays (200-5000 eV), and hard X-rays (>5000 eV). VUV and soft X-rays can only access lower energy levels and have large absorption coefficients, compared to hard X-rays, which makes them more prone to absorption by air and other media (like figure 2-8 shows above), providing surface and near surface sensitivity.

2.2.2 Detection mode

The most important factor of XAS is to measure the attenuation X-ray absorption coefficient of material using the tunable energies, which is on/above the absorption edge. In general, XAS can be utilized by different detection modes to fulfill diverse requirements of experiments and gather distinct data to character samples. Multiple detectors are equipped in the beamline and working simultaneously. Fluorescence yield (FLY), total electron yield (TEY) and transmission are the three most common modes in the beamlines. As the X-ray beam interacting upon the sample, it can exhibit different ways as depicted in Figure 2-9.

Transmission mode is the most direct way to calculate the absorption coefficient by applying the **Equation 2-1,** which is based on the Beer-Lambert Law (details in section 2.2.1).

$$\mu t = ln\frac{I_0}{I_t} \quad \textbf{(Equation 2-1)}$$

However, the limitations of transmission mode are the thickness of samples and the energy level of X-rays. The sample must less than one-absorption-length (μt = 1) to achieve around 36.8% transmission rate. Normally the hard X-rays beamlines are equipped with the transmission mode, because of the incident X-ray is high enough to pass through the sample. In this project, no transmission detection was used, partly because of the low energy, partly because of the sample geometry.

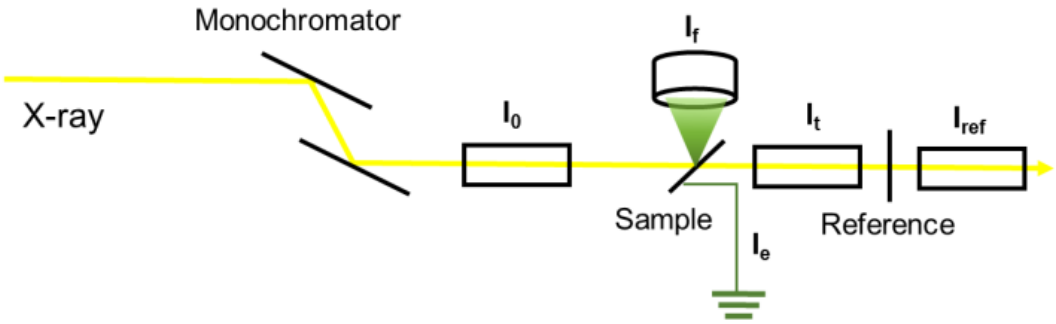

Figure 2-10. Schematic illustration of detection modes in XAS

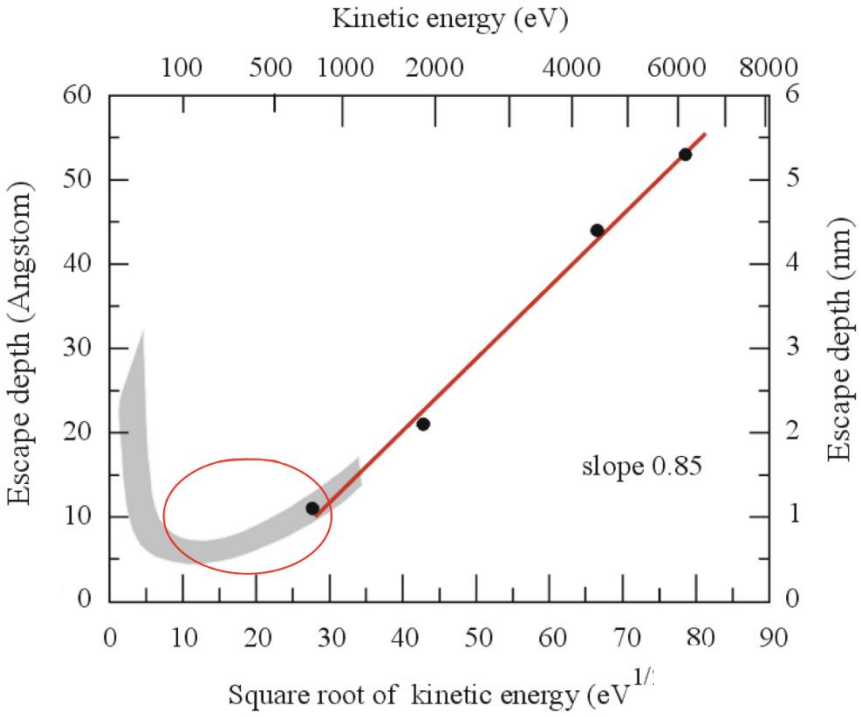

Figure 2-11. The spectra of Attenuation lengths from Synchrotron Radiation (SR) measurements[16].

Total electron yield (TEY) modes collect the current compensation signals (I_e) from total number of electrons (including photoelectrons, auger electrons, and secondary electrons – figure 2-10) ejected from the material. Since the electrons is low mass charge carriers, their travel trajectories are significantly influenced by electromagnetic fields. Consequently, the TEY mode is restricted

to measuring the surface of samples. The relationship between electron escape length and its kinetic energy is shown as Fig. 2-11. TEY is particularly advantageous for soft X-ray measurements due to the exceptionally short attenuation length of electrons, thereby mitigating the influence of thickness effects.

TEY modes were employed in this project to gather the information from both surface and bulk properties of samples in XANES.

2.2.3 X-ray excited optical luminescence (XEOL)

X-ray excited optical luminescence (XEOL) refers to the energy-transfer process where the absorption of an X-ray photon generates high-energy electrons (including Auger electrons and photoelectrons). Subsequently, the further ionization and excitation of these high-energy electrons occurred. Energy is conveyed to luminescent center via inelastic processes, while the appearance of holes in the VB and electrons in the CB in the semiconductor materials. The ensuing recombination of holes and electrons results in the emission of light in the UV-visible and Near IR region (commonly known as optical photons).[17] It can be descried as a photon-in and photon-out technique. It plays a significant role on the analyzation of the light-emitting material[18–20]. Figure 2-11 illustrates that a substance is exposed to high-energy photons, causing the excitation of electrons which then undergo de-excitation pathways, ultimately resulting in the emission of optical photons.

By combining XEOL and XAS, it creates a new method to investigate the electronic properties of materiel in a highly site-selective approach[21]. The XAS-XEOL research is original concentrated on semiconductor structures, where defects and/or surface states display unique luminescence, and associations with specific chemical phases can be determined through their distinct XAS[22–24].

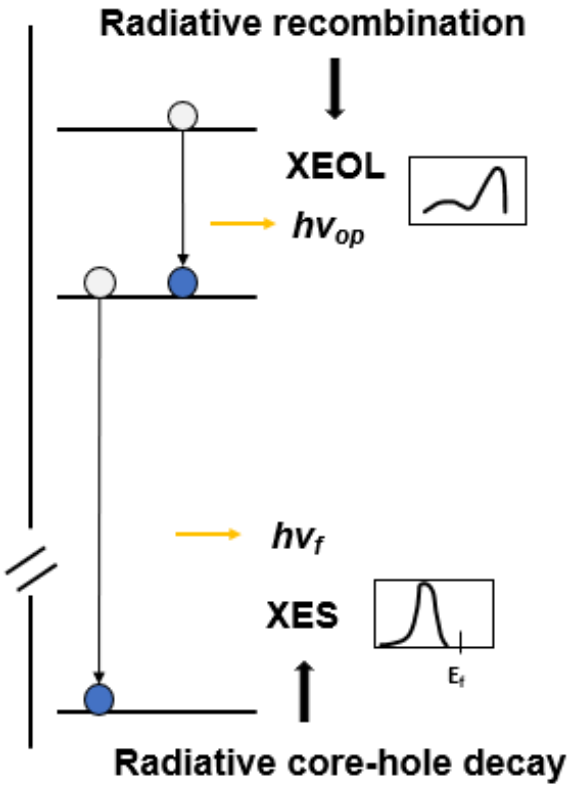

Figure 2-12. The process of radiative combination (XEOL) and the radiative core-hole decay (XES) with their schematic spectrums

2.2.4 X-ray Emission Spectroscopy (XES)

X-ray Emission Spectroscopy (XES) can be also introduced as a photon-in and photon-out technique. In Figure 2-11, a core hole is left behind when an X-ray excites a core electron out of its shell. The transition of electrons from the higher energy level to the spot will occur. This recombination process creates emitted photons, which can be measured. X-ray emission spectrum can be used to determine the electronic environment of chemicals[25].

By combining the XAS (probing the HOMO and HOMO + in molecules or the unoccupied electronic states, such as the conduction band in solids) and XES (probing the LUMO, LUMO – in molecules or the occupied electronic states, the valence band in solids) data, the band gap can be calculated in this project and the electronic structure in the vicinity of the fermi level can be track. XEOL and XES data were collected simultaneously from RIXS beamline at CLS.

2.3 Other characterization techniques

2.3.1 Powder X-ray diffraction (PXRD)

The Powder X-ray diffraction is designed to employ the information of an x-ray beam through material to generate crystallinity of samples in the solid state.

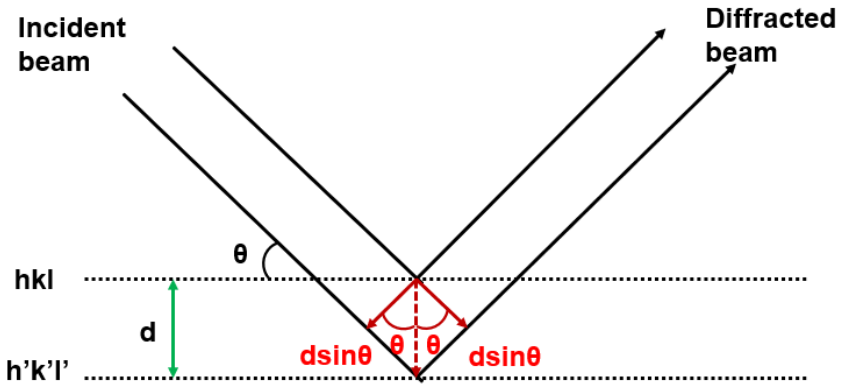

Figure 2-13. Crystallographic diffraction geometry

Figure 2-12 shows the geometry of X-ray diffraction. When an x-ray beam meets a crystal, it causes the electrons in its path to vibrate at the same frequency and wavelength as the incident beam. While many of the scattered waves cancel each other out, some scatter in certain directions where the waves reinforce each other, resulting in diffraction. This phenomenon occurs because each atom in a row of atoms can be thought of as the center of a radiating spherical wave. If the scattered waves reinforce each other constructively, the wave fronts align and produce a cooperative scattering effect that causes diffraction. Diffraction occurs when waves bend and spread out, and it can provide information about the arrangement of the atoms. The relationship between the angle of incidence beam and the resulting diffraction pattern can be described as **Equation 2-4**, which is known as the Bragg Law.

$$n\lambda = 2d \sin\theta \quad (\textbf{Equation 2-4})$$

In **Equation 2-4**, n is the order of reflection (1, 2, 3, …, n), λ is the wavelength of the incident X-ray beam, d is the distance between the planes of atoms in a crystal lattice, θ is the angle between

the incident X-ray and the crystal lattice planes, and 2θ is the angle between the incident and diffracted beams.

The diffraction pattern that is produced is a fingerprint of crystal structure of the material which can be utilized to identify the unknown materials. In this project, part of X-ray diffraction (XRD) data was collected at the Chemistry Department of Western University using a specialized equipment setup. The equipment includes a sealed tube source that emits Cu Kα radiation with a diffraction angle of 1.5 (2 θ), as well as an Inel XRG3000 generator and an Inel CPS 120 detector. Moreover, some XRD data was measured at 19A High resolution Powder Diffraction (HRXRD) of Taiwan Photon Source (TPS) in Hsinchu, Taiwan. The wavelength of the incident X-ray was 0.61992 Å (20 keV).

2.3.2 Scanning electron microscope (SEM)

In this study, SEM was utilized to characterize the morphology of the metal oxides produced in the ball-milling process. A focused high-energy electron beam scans the surface of specimens, leading to the interaction of electrons and sample and deceleration of electrons in the specimens.

The technique offers several detection modes, secondary electrons (SE), back-scattered electrons (BSE), In-Lens and Everhart-Thornley (E-T). SE arise due to the ionization of the material. When low-energy electrons are applied, the SE signal from the outermost stratum (few nanometers) of the surface can be detected.[26,27] The signal intensity of SEM, which is proportional to the number of SE detected, is then employed to construct a morphological image of the sample surface, as shown in Figure 2-13.

The In-lens detector, located within the path of the beam (as shown in Figure 2-14), offers a highly efficient detection performance. Attributable to an advanced magnetic field at the pole piece, there is a substantial enhancement in the efficiency of SE collection. It is noteworthy that the in-lens detector perceives electrons from an identical viewpoint as the source beam, whereas the Everhart-Thornley (E-T) detector intercepts electrons from an alternative angle.

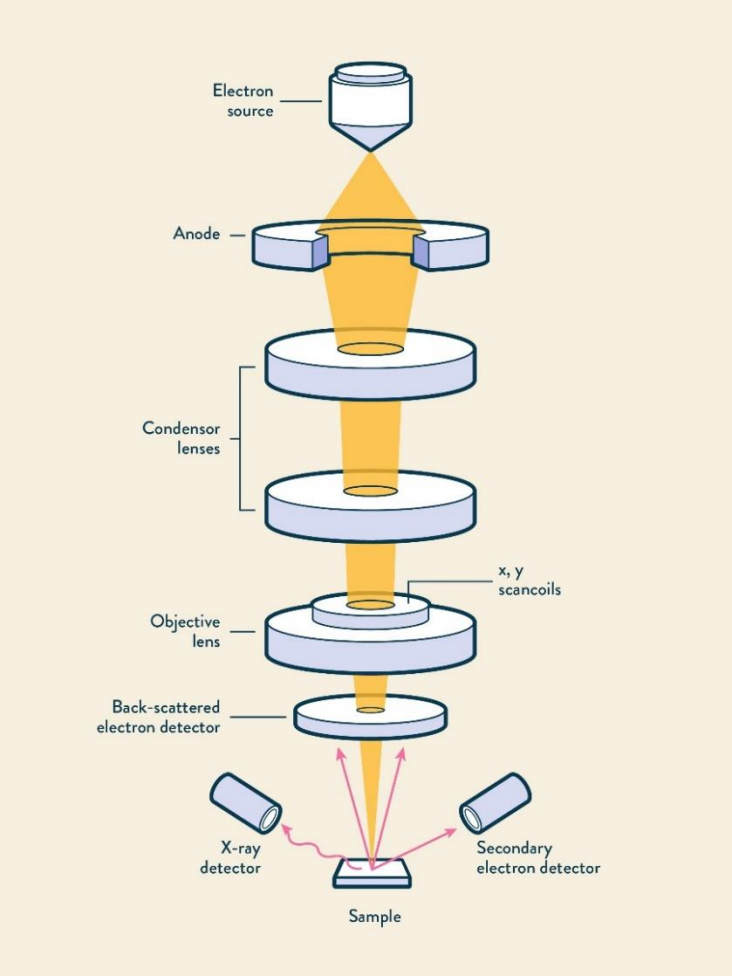

Figure 2-14. A Geometry of fundamental components of Scanning Electron Microscope[28]

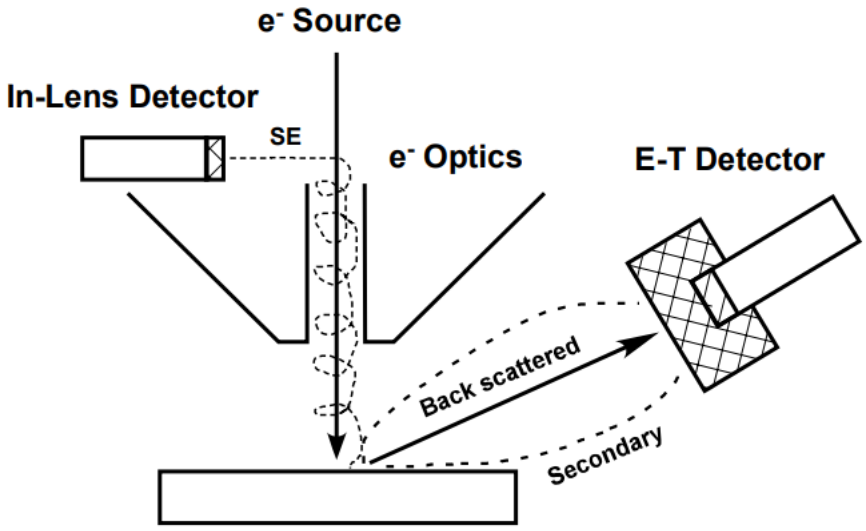

Figure 2-15. Schematic diagram of SEM with two detectors[29].

The SEM investigation was conducted at the Western Nanofabrication Facility employing the Zeiss (Oberkochen, Germany) LEO 1530 and 1540XB instruments. The electron high tension (EHT) was set to 1 kV for the analysis.

2.3.3 Transmission electron microscope (TEM)

To utilize more morphology details from samples, transmission electron microscope (TEM) is employed in this project. Different from the SEM, the electron beam is transmitted through a very thin sample (size <150 nm), creating the detailed images about the sample's crystal structure, composition, and morphology.

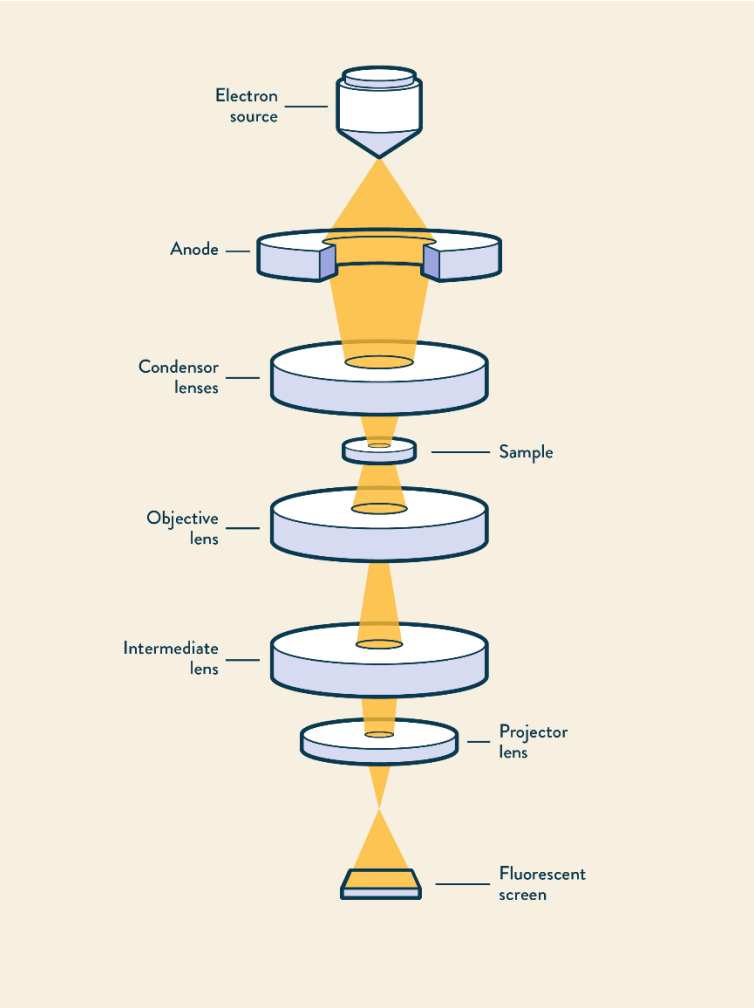

Figure 2-16. A Geometry of fundamental components of Transmission Electron Microscope[28]

Figure 2-14 illustrates the fundamental components of the TEM. At the top of the TEM, the electron gun emits a broad stream of high-energy electrons to the vacuum tube and pass the

condenser lens. The condenser lens is used to focus the board beams into a thin coherent electronic beam, while the condenser aperture limits the beam by blocking electrons with high angles. Afterward, the beam encounters the specimen and a portion of it is transmitted, depending on the sample's thickness and electron transparency. The objective lens then concentrates this transmitted portion onto a phosphor screen resulting in an image[30].

The TEM investigation was conducted at the Canadian Center for Electron Microscopy at University of McMaster employing the Thermo Scientific Talos L120C and the Thermo Scientific Talos 200X instruments.

Table 2-1. The comparison of SEM and TEM[31]

	SEM	TEM
Electron Source	Focused high-energy electron beam; up to 30 kV	Broad high-energy electron beam; 60-300 kV
Resolution	~0.5 nm	<50 pm
Magnification	Up to 2 million	Up to 50 million
Image	(morphology of surface) 3-D[31]	(Inner structure)2-D[31]
Sample limitation	No specific limitations	Thin sample: size < 150 nm

2.3.3 Energy-dispersive X-ray spectroscopy (EDX)

Energy-dispersive X-ray spectroscopy (EDX/EDS/EDXS) is a technique employed for the identification and characterization of chemical elements. It relies on the interactions occurring at the sample surface, precipitated by the incident electron beam. The atoms are ionized to by incident electrons and forming ejected electrons and vacancy in the inner shell. To transition to a lower energy state, an electron from an outer shell fills the vacancy left by the ejected electron, in the process releasing an energy quantum. The resulting energy is corresponded to the energy level of the orbits, making it a consistent parameter for elemental identification. It can be further collected in EDX detectors and analyzed in computer. The EDX measurement used in this project is carried out at the TEM analysis.

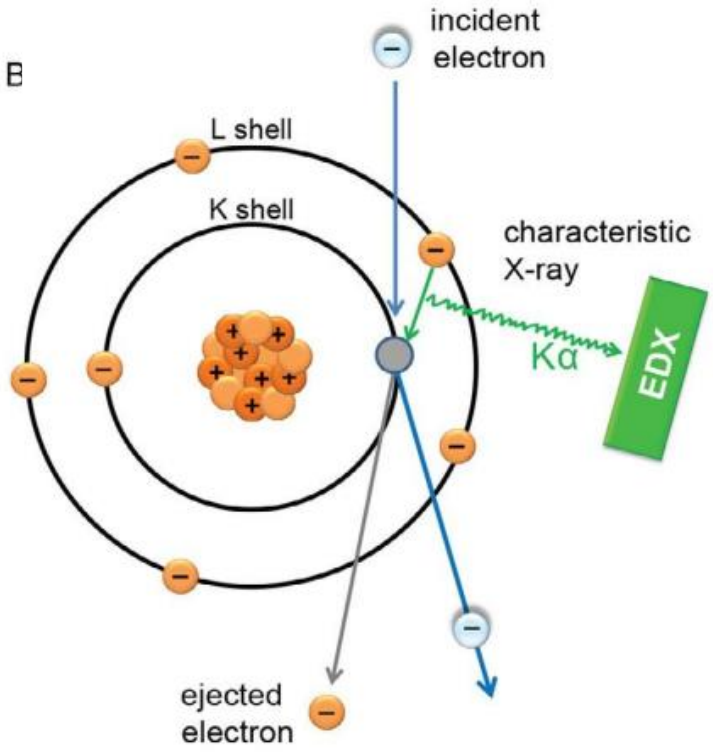

Figure 2-17. Schematic illustration of EDX analysis to map atoms[32].

2.3.4 WIEN2k calculation and the plots of density of states (DOS)

WIEN2k is a computer language of density functional theory. It can use to generate the information of local density approximation, Modified Becke-Johnson (MBJ) exchange potential and generalized gradient approximation. Density functional theory is based on the Kohn-Sham's equation (**Equation 2-6**). Where T[n] represents the Kohn-Sham kinetic energy functional of n electrons system, v[r] represents the external potential, n[r] is the density, and E_{xc}[n] is the exchange-correlation energy functional of an interacting system with density n[r].

$$\mathrm{E} = \mathrm{T[n]} + \int v(r)n(r)d^3r + \iint \frac{n(r)n(r')}{|r-r'|} d^3r d^3r' + E_{xc}[n] \quad \textbf{(Equation 2-6)}$$

Based on the density functional theory, the plots of density of states (DOS) can be calculated. The plots of DOS provide the information of electronic structures and optical properties of materials in a simple but highly-informative method. It provides a quantitative evaluation of the various energy states present within a system that electrons have the potential to occupy. The X-axis represents energy level with unit of electronvolt (eV), and Y-axis is the density of states with the unit of number of electrons in per eV. In each plot, the valance band maximum (VBM) is set to 0

eV, while the lower energy range corresponds to the valance band (VB) and the higher energy range corresponds to the conduction band (CB). Total density of states (TDOS) is the cumulative contribution from all atoms and orbitals in the system, and others represent the partial DOS (as shown in Figure 2-16, black line is TDOS and others are partial DOS).

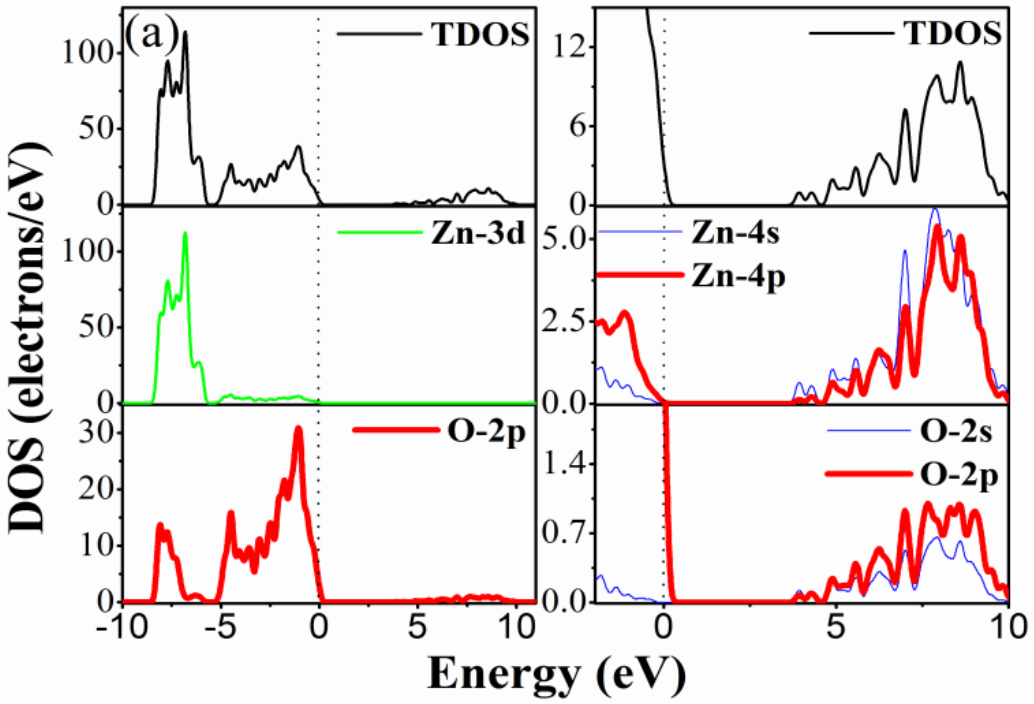

Figure 2-18. Calculated DOS plots of ZnO[33]

In this project, the theoretically DOS and simulate of XAS of part of samples were calculated using WIEN2k language by Dr. Yun-Mui Yiu.

2.4 Reference

1. Gavaghan, H. (2001). What is a synchrotron? Nature, 410(6829), 722–722. https://doi.org/10.1038/35070715
2. Robinson, A. L. (2015). History of synchrotron radiation. Synchrotron Radiation News, 28(4), 4–9. https://doi.org/10.1080/08940886.2015.1059228
3. Hettel, R. (2014). DLSR design and plans: An international overview. Journal of Synchrotron Radiation, 21(5), 843–855. https://doi.org/10.1107/s1600577514011515
4. Bilderback, D. H., Brock, J. D., Dale, D. S., Finkelstein, K. D., Pfeifer, M. A., Gruner, S. M. (2010). Energy Recovery LINAC (ERL) coherent hard X-ray sources. New Journal of Physics, 12(3), 035011. https://doi.org/10.1088/1367-2630/12/3/035011
5. Pellegrini, C., Marinelli, A., Reiche, S. (2016). The physics of X-ray free-electron lasers. Reviews of Modern Physics, 88(1). https://doi.org/10.1103/revmodphys.88.015006
6. Tavares, P. F., Leemann, S. C., Sjöström, M., Andersson, Å. (2014). The Max IV Storage Ring Project. Journal of Synchrotron Radiation, 21(5), 862–877. https://doi.org/10.1107/s1600577514011503
7. Lower emittance lattice for the advanced photon source upgrade using ... (n.d.). https://accelconf.web.cern.ch/napac2016/papers/wepob01.pdf
8. Liu, L., Milas, N., Mukai, A. H., Resende, X. R., de Sá, F. H. (2014). The sirius project. Journal of Synchrotron Radiation, 21(5), 904–911. https://doi.org/10.1107/s1600577514011928
9. Cutler, J., Chapman, D., Dallin, L., Lamb, R. (2017). The Brightest Light in Canada: The Canadian Light Source. Quantum Beam Science, 1(1), 4. https://doi.org/10.3390/qubs1010004
10. XAS endstation. SGM. (n.d.). https://sgm.lightsource.ca/about-us/xas-endstation/
11. REIXS beamline. REIXS. (n.d.). https://reixs.lightsource.ca/about/beamline/
12. Beamline map. Taiwan Photon Source Beamlines. (n.d.). https://tpsbl.nsrrc.org.tw/index.aspx?lang=en
13. Aneesh, P. M., Krishna, K. M., Jayaraj, M. K. (2009). Hydrothermal synthesis and characterization of undoped and EU-doped ZnGaO nanoparticles. Journal of The Electrochemical Society, 156(3). https://doi.org/10.1149/1.3070662
14. Yano, J., Yachandra, V. K. (2009). X-ray absorption spectroscopy. Photosynthesis Research, 102(2–3), 241–254. https://doi.org/10.1007/s11120-009-9473-8
15. de Groot, F. M., Hu, Z. W., Lopez, M. F., Kaindl, G., Guillot, F., Tronc, M. (1994). Differences between L_3 and L_2 X-ray absorption spectra of transition metal compounds. The Journal of Chemical Physics, 101(8), 6570–6576. https://doi.org/10.1063/1.468351
16. Dallera, C., Duò, L., Braicovich, L., Panaccione, G., Paolicelli, G., Cowie, B., Zegenhagen, J. (2004). Looking 100 Å deep into spatially inhomogeneous dilute systems with hard X-ray photoemission. Applied Physics Letters, 85(19), 4532–4534. https://doi.org/10.1063/1.1814441
17. Sham, T. K., Sammynaiken, R., Zhu, Y. J., Zhang, P., Coulthard, I., Naftel, S. J. (2000). X-ray excited optical luminescence (XEOL): A potential tool for Oeld Studies. Thin Solid Films, 363(1–2), 318–321. https://doi.org/10.1016/s0040-6090(99)01006-8
18. Sham, T. K. (2015). Soft X-ray excited optical luminescence from Functional Organic Materials. Journal of Electron Spectroscopy and Related Phenomena, 204, 196–207. https://doi.org/10.1016/j.elspec.2015.04.004

19. Peng, M., Li, Y., Gao, J., Zhang, D., Jiang, Z., Sun, X. (2011). Electronic structure and photoluminescence origin of single-crystalline germanium oxide nanowires with green light emission. The Journal of Physical Chemistry C, 115(23), 11420–11426. https://doi.org/10.1021/jp201884y
20. Paik, T., Gordon, T. R., Prantner, A. M., Yun, H., Murray, C. B. (2013). Designing tripodal and triangular gadolinium oxide nanoplates and self-assembled Nanofibrils as potential multimodal bioimaging probes. ACS Nano, 7(3), 2850–2859. https://doi.org/10.1021/nn4004583
21. Hageraats, S., Keune, K., Stanescu, S., Laurent, J.-M., Fresquet, W., Thoury, M. (2021). Combining X-ray excited optical luminescence and X-ray absorption spectroscopy for correlative imaging on the nanoscale. Journal of Synchrotron Radiation, 28(6), 1858–1864. https://doi.org/10.1107/s1600577521009450
22. Sham, T. K., Naftel, S. J., Kim, P.-S. G., Sammynaiken, R., Tang, Y. H., Coulthard, I., Moewes, A., Freeland, J. W., Hu, Y.-F., Lee, S. T. (2004). Electronic structure and optical properties of silicon nanowires: A study using X-ray excited optical luminescence and X-ray emission spectroscopy. Physical Review B, 70(4). https://doi.org/10.1103/physrevb.70.045313
23. Armelao, L., Heigl, F., Jürgensen, A., Blyth, R. I., Regier, T., Zhou, X.-T., Sham, T. K. (2007). X-ray excited optical luminescence studies of ZnO and EU-doped ZnO nanostructures. The Journal of Physical Chemistry C, 111(28), 10194–10200. https://doi.org/10.1021/jp071379f
24. Li, J., Liu, L., Sham, T.-K. (2015). 2d XANES–XEOL spectroscopy studies of morphology-dependent phase transformation and corresponding luminescence from hierarchical TiO_2 nanostructures. Chemistry of Materials, 27(8), 3021–3029. https://doi.org/10.1021/acs.chemmater.5b00363
25. Zimmermann, P., Peredkov, S., Abdala, P. M., DeBeer, S., Tromp, M., Müller, C., van Bokhoven, J. A. (2020). Modern X-ray spectroscopy: XAS and XES in the Laboratory. Coordination Chemistry Reviews, 423, 213466. https://doi.org/10.1016/j.ccr.2020.213466
26. Egerton, R. F. (2005). Physical Principles of Electron Microscopy. https://doi.org/10.1007/b136495
27. Townshen, A. (1983). Principles of instrumental analysis. Analytica Chimica Acta, 152, 314. https://doi.org/10.1016/s0003-2670(00)84936-3
28. SEM vs TEM. Analysis Separations from Technology Networks. (n.d.). http://www.technologynetworks.com/analysis/articles/sem-vs-tem-331262
29. Virginia Tech. (2006). Metal oxide nanoparticles: Optical properties and interaction with chemical warfare agent simulants (dissertation).
30. Wang, Z. L. (2000). Transmission electron microscopy of shape-controlled nanocrystals and their assemblies. The Journal of Physical Chemistry B, 104(6), 1153–1175. https://doi.org/10.1021/jp993593c
31. Zhao, J., Liu, X. (2023). Electron microscopic methods (TEM, SEM and energy dispersal spectroscopy). Encyclopedia of Soils in the Environment, 575–588. https://doi.org/10.1016/b978-0-12-822974-3.00013-6
32. Pirozzi, N. M., Kuipers, J., Giepmans, B. N. G. (2021). Sample preparation for energy dispersive X-ray imaging of biological tissues. Methods in Cell Biology, 89–114. https://doi.org/10.1016/bs.mcb.2020.10.023

33. Wu, H.-C., Peng, Y.-C., Shen, T.-P. (2012a). Electronic and optical properties of substitutional and interstitial Si-doped ZnO. Materials, 5(11), 2088–2100. https://doi.org/10.3390/ma5112088

Chapter 3

Chapter 3. XANES and XEOL studies of ball-milling metal oxides

This chapter presents a study of the influence of various ball-milling rates in the phase transition of TiO_2 and the formation of anatase and rutile TiO_2 heterostructure. The SEM, TEM, XANES, LCF and 2D-XANES-XEOL of various rates of ball-milling samples will be discussed.

3.1 Introduction

The discovery of titanium (Ti) occurred in 1791, followed by the identification of naturally-occurring titanium dioxide (TiO_2) in 1795[1]. Industrial production of TiO2 began in the 1920s[1]. In addition to its established industrial applications, TiO_2 has been subjected to extensive investigation for its potential applications in diverse fields such as water remediation[2], photocatalysis[3], lithium-ion batteries[4], and sensor devices[5], among others. Anatase, rutile and brookite are three phases of natural TiO_2 and the physical and chemical properties are diversified by size effects and associated surface effects. When the coherent diffraction domains of these TiO_2 systems are reduced to the nanometer scale, notable alterations occur in the band gap, refractive index, and rate of charge transfer across the interface.[6] Previous research demonstrates that a mixed composition of anatase and rutile TiO_2 exhibits enhanced photocatalytic activity compared to pure anatase or rutile TiO_2[7,8]. Notably, the enhancement of photoactivity is more pronounced in the nanometer-scaled mixed TiO_2[7]. These findings provide passion for further research focused on optimizing the structural characteristics of TiO_2 through the utilization of the mixed-phase approach.

The transition from anatase to rutile phase typically occurs within a temperature range of 600°C to 700 °C[9]. Numerous techniques have been employed to modify this transition, such as metal oxide doping[10], hydrothermal methods[11], and chemical vapour deposition[12,13]. In the industry, ball-milling is widely used as an environmentally friendly approach for mechanochemical reaction[14]. This project focuses on the phase transition process of TiO_2 that happened in the ball-milling experiment.

The morphology of the nanoparticles and their phase transformation of the nanoparticles are monitored using scanning electron microscopy (SEM), transmission electron microscopy (TEM)

and X-ray diffraction (XRD) techniques, respectively. Besides that, X-ray absorption near-edge structures (XANES) offer greater sensitivity in assessing the chemical and structural environment, and linear combination fitting is utilized to determine the chemical ratio within the product.

3.2 Experimental section

3.2.1 Ball-milling metal oxides synthesis

3.2.1.1 Materials

Anatase titanium (IV) oxide (TiO_2, nanopowder, <25 nm particle size, 99.7% trace metals basis), Rutile titanium (IV) oxide (TiO_2, nanopowder, <100 nm particle size, 99.5% trace metals basis) were commercial products, which were purchased from Sigma Aldrich. All chemicals were used without further purification.

3.2.1.2 Synthesis method

One gram of commercially nanosized powder, anatase TiO_2, was added to a 125 mL zirconium dioxide (ZrO_2) grinding jar, along with a set of ZrO_2 grinding balls (Figure 3-1). The inner diameter of jar is 50 mm, outer diameter is 70 mm, and the depth is 50 mm. The ball-milling jars were evacuated to maintain a vacuum state during the milling process. The milling speeds were set at 150, 300 and 500 rpm using the Planetary Ball Mill PM 200. The ball milling procedure was carried out for a duration of 10 hours. Subsequently, the resulting samples #1-#3 (as detailed in Table 3-1) were collected and subjected to characterization. Sample #4 was prepared by mixing 3 grams of commercial anatase TiO_2 and rutile TiO_2. In the case of samples 5 and 6, identical quantities of commercially available anatase TiO_2 and rutile TiO_2, amounting to a total of 1 gram, were measured and incorporated into a 125 mL ZrO_2 milling jar, accompanied by ZrO_2 milling balls. Similar to previous experiment, the jars were evacuated, and the ball milling rates were regulated at 300 and 500 rpm, with the process lasting for 10 hours.

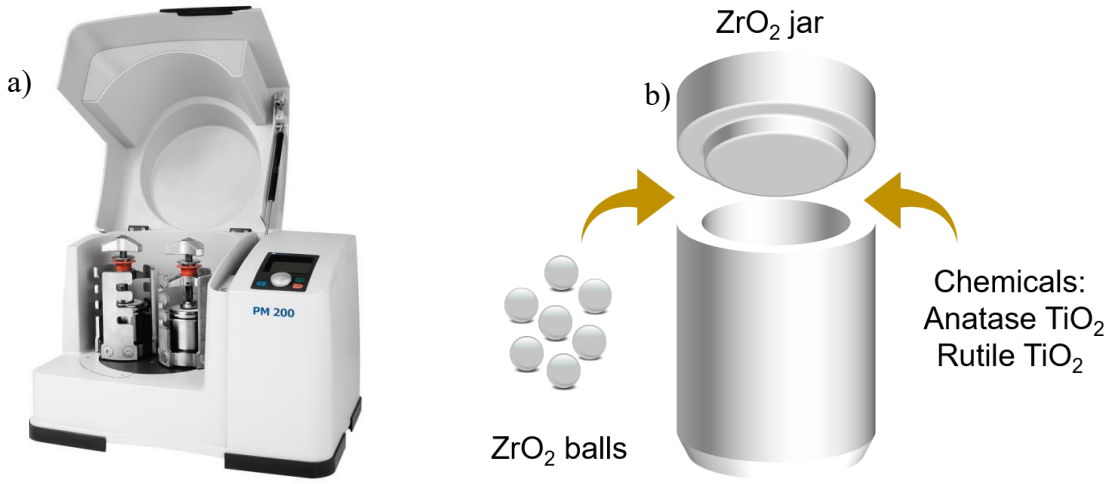

Figure 3-1. a) Planetary Ball Mill PM 200 image from Retsch.com b) 125 mL Ball mill jars

Table 3-1. Samples synthesized with different conditions.

Sample ID	Precursor Type	Synthesis Method	Ball Mill Speed	Processing Time	Full Name
#1	Anatase TiO_2	BM	150 rpm	10 h	A-TiO_2-150
#2	Anatase TiO_2	BM	300 rpm	10 h	A-TiO_2-300
#3	Anatase TiO_2	BM	500 rpm	10 h	A-TiO_2-500
#4	Anatase & Rutile TiO_2	Mixing			(A+R) TiO_2-mix
#5	Anatase & Rutile TiO_2	BM	300 rpm	10 h	(A+R) TiO_2-300
#6	Anatase & Rutile TiO_2	BM	500 rpm	10 h	(A+R) TiO_2-500

3.2.2 Characterization

Powder X-ray diffraction (PXRD), scanning electron microscope (SEM), transmission electron microscope (TEM), X-ray absorption near edge spectrum (XANES), and X-ray excited optical luminescence (XEOL) have been reported.

The chemical composition, morphology, and crystallographic structure can be accomplished by employing SEM (via a Zeiss-LEO 1530 Gemini FE-SEM), TEM, and PXRD. Technical support for TEM (Thermo Scientific Talos 200X) was provided by the Canadian Center for Electron Microscopy at McMaster University, while PXRD technical assistance (Inel CPS Powder Diffractometer, Cu Kα radiation with 2θ=1.5) was supplied by the X-ray facility at Western University and 19A HRXRD beamline of TPS in Hsinchu, Taiwan with wavelength of the incident X-ray was 0.61992 Å (20 keV). The XANES and XEOL data were obtained at the Spherical Grating Monochromator beamline (SGM-featuring energy in the range of 250 to 2000 eV) and the Resonant Inelastic X-ray Scattering (RIXS-featuring energy in the range of 95 to 2000 eV) beamline at the Canadian Light Source (CLS) in Saskatoon, Saskatchewan, Canada. For the purposes of this study, incident photon flux was used to normalize all XANES and XEOL spectra.

Results and discussions

3.3 Ball-milling anatase TiO_2 in various rate

3.3.1 Morphology

The TEM and SEM images reveal detailed structural information in nano-domain, facilitating the examination of individual nanoparticles and their corresponding morphological features. And TEM and SEM images provide insight into the size distribution, shape, and surface characteristics of the nanoparticles, enabling a comprehensive analysis of their physical properties.

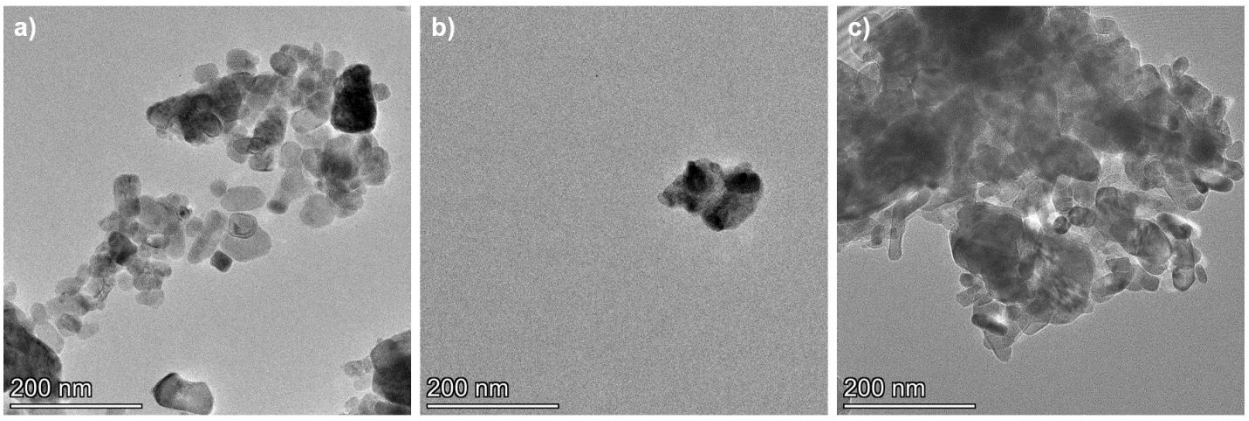

Figure 3-2. TEM images with a magnification of 7400 x of a) sample#1 b) sample #2 c) sample #3

The TEM images of samples #1 (A-TiO_2-150), #2 (A-TiO_2-300) and #3 (A-TiO_2-500) are presented in Figure 3-2 a, b, and c respectively. Following the modification through ball-milling, the nanoparticles demonstrated an exhibited size range of 20-50 nm. In the higher ball-milling rate (300 and 500 rpm), a predominant observation was the propensity of the particles to undergo aggregation, resulting in the formation of larger clusters.

3.3.2 Chemical Composition

In order to corroborate the phase transition of TiO_2 and the presence of heterostructures, the utilization of XRD analysis serves as an indispensable mechanism to affirm the chemical constituents of the samples. Verification of the chemical entities can be achieved by juxtaposing the resultant products against standard Powder Diffraction File (PDF) cards.

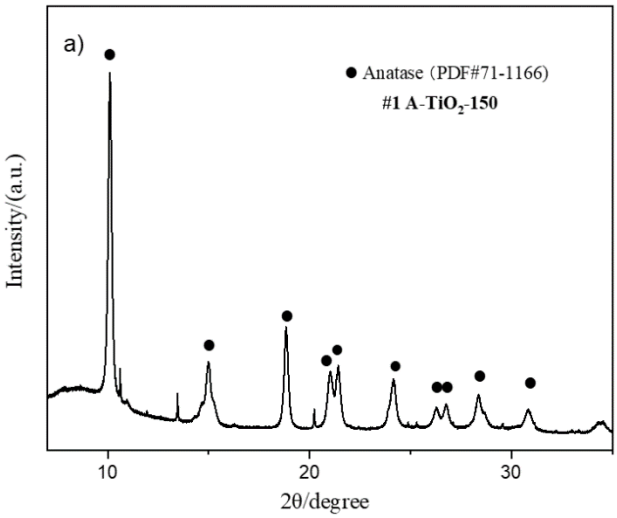

Figure 3-3. XRD images of sample #1 (A-TiO_2-150) with anatase TiO_2 PDF #78-1510

For samples #1 (A-TiO_2-150) (as illustrated in Figures 3-3), only signals originating from the precursor was detectable. This finding, is consistent with the TEM result, suggests that no phase transition occurred at lower ball milling speeds.

Figure 3-4 illustrate the formation of chemical component in sample #2 (A-TiO_2-300) and sample#3 (A-TiO_2-500). The products exhibited signals corresponding to both anatase and rutile TiO_2 phases, indicating the occurrence of a phase transition during the ball milling process. The

integrated area of anatase TiO_2 is noticeably lower compared to rutile, indicating a higher degree of crystallinity for the rutile phase relative to anatase. Furthermore, the integrated area of the rutile peak surpasses that of anatase, suggesting a higher concentration of rutile compared to anatase.

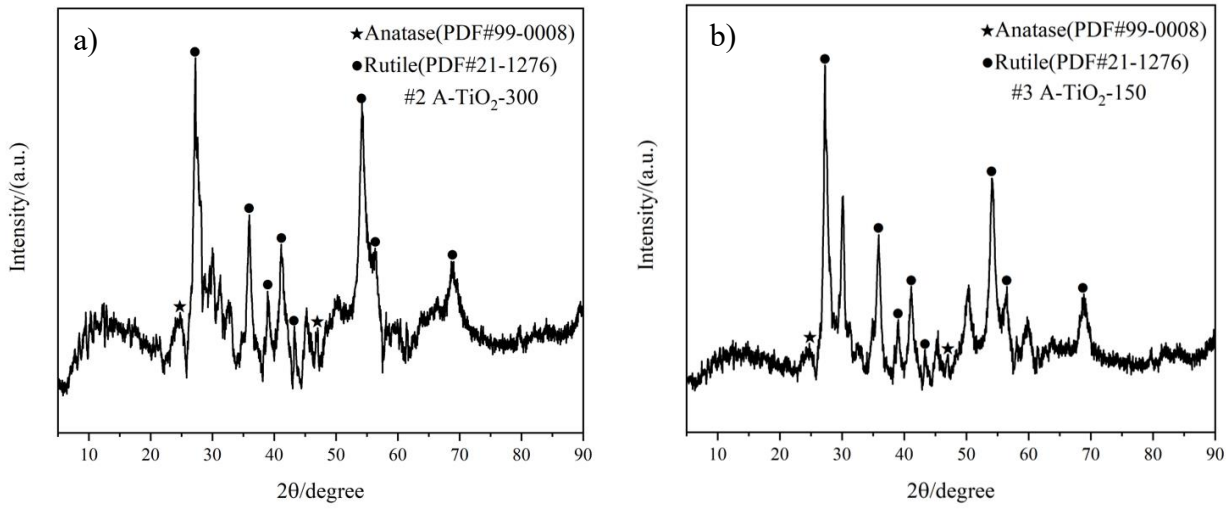

Figure 3-4. XRD images of a) sample #2 (A-TiO_2-300) b) sample#3 (A-TiO_2-500) with anatase TiO_2 PDF #99-0008 and rutile TiO_2 PDF #21-1276

3.3.3 XANES analysis

The X-ray absorption near-edge structures (XANES or XAS) spectra provides valuable insight into different aspects of chemical and electronic structure. Pre-edge, white line and beyond the edge are the three main features that need to be analyzed. Pre-edge: prior to the absorption edge, the intensity of pre-edge peaks is notably influenced by the coordination geometry surrounding the central atom. White line: following the absorption edge, a qualitative assignment of the oxidation state can be determined. Beyond the edge: the investigation extends just beyond the edge, focusing on the coordination shells as the emitted photoelectron interact with neighboring atoms[15].

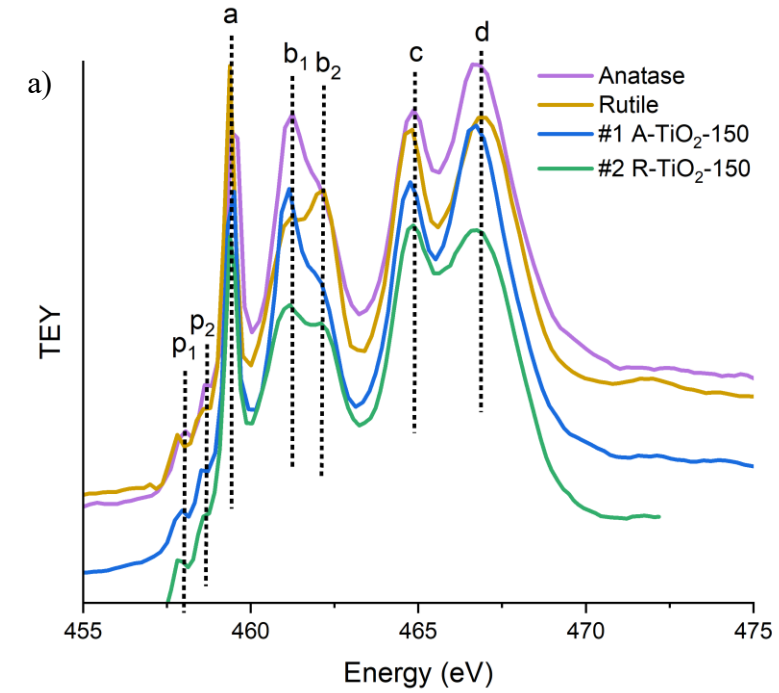
a)
a
b1 b2
c
d
p1
p2
Anatase
Rutile
#1 A-TiO2-150
#2 R-TiO2-150
TEY
455
460
465
470
475
Energy (eV)

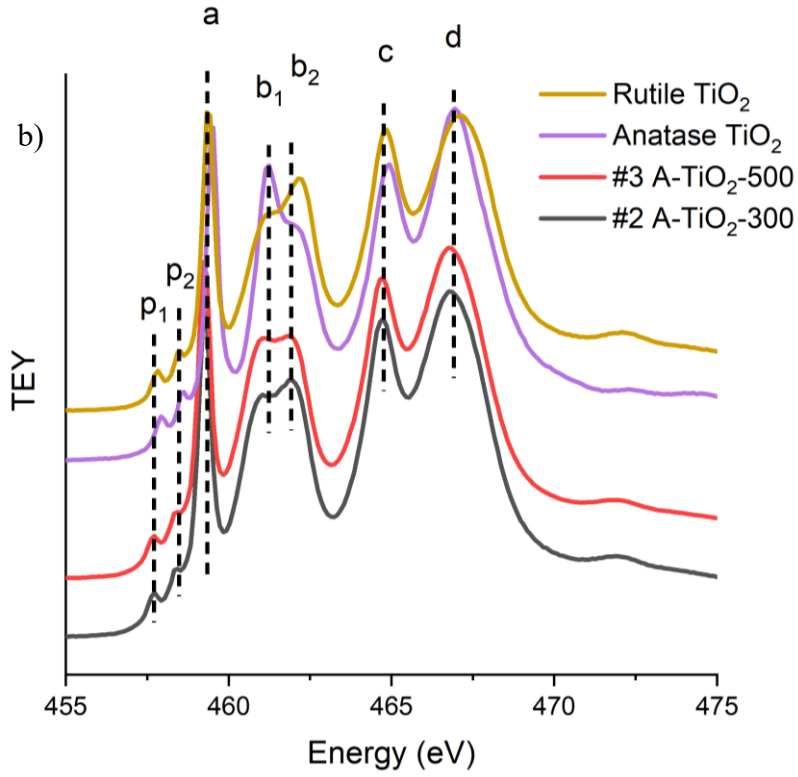
b)
a
b1
b2
c
d
p1
p2
Rutile TiO2
Anatase TiO2
#3 A-TiO2-500
#2 A-TiO2-300
TEY
455
460
465
470
475
Energy (eV)

Figure 3-5. XANES spectrums at the Ti $L_{3,2}$-edge of a) samples 1 (A-TiO_2-150) and reference anatase and rutile TiO_2 b) samples #2 and #3 (A-TiO_2-300 and A-TiO_2-500) and reference anatase and rutile TiO_2

The XANES spectra in Fig 3-5 were collected at the Spherical Grating Monochromator (SGM) beamline in TEY detection mode, situated at the Canadian Light Source (CLS) within the University of Saskatchewan in Saskatoon. XANES spectra were generated for samples 1-6 across Ti $L_{3,2}$-edge. Figure 3-5a generate the XANES data of samples 1 (A-TiO_2-150), and Figure 3-5b generate the XANES data of samples #2 and #3 (A-TiO_2-300 and A-TiO_2-500).

Generally, the XANES observed at the Ti $L_{3,2}$-edge represent a state where X-ray excited electrons from the 2p core level to unoccupied 3d states of the Ti atom. However, these structures demonstrates a more complex configuration, resulting from the coupling of the crystal field effect and the atomic interaction[16,17]. Figure 3-a, a and b display two small pre-peaks p_1&p_2 prior to the absorption edge, which are caused by core-hole-d-electron interactions[18]. Peak a, b_1, and b_2 (at Ti L_3-edge) correspond to electron transition from Ti $2p_{3/2}$ to Ti 3d states, while peaks c and d (at Ti L_2-edge) originate from the electron transition from Ti $2p_{1/2}$ to Ti 3d states[18,19]. Based on the crystal field splitting, both Ti L_3-edge (457-462 eV) and Ti L_2-edge (462-469 eV) exhibit peak splitting into two groups: t_{2g} (peak a and c) and e_g (peak b and d)[18–21]. In the reference samples of rutile and anatase TiO_2, the e_g (peak b) further split into peak b_1 and b_2 at Ti $L_{3,2}$-edge, attributed to the presence of local[22] or long-range[23] tetragonal distortion at the Ti site with the TiO_6 octahedron. The distinction between peaks b_1 and b_2 serves as a distinctive characteristic for the rutile (D_{2h}) and anatase (D_{2d}) phases of TiO_2, resulting from the local distortions of TiO_6 in each octahedral symmetry. In anatase TiO_2, peak b_1 is more pronounced than b_2, while the opposite is observed in rutile TiO_2.

Figure 3-5a demonstrates that samples #1 exhibits peak characteristics resembling those of reference anatase TiO_2. Nevertheless, a closer examination reveals a reduction in the distinguishability of the additional split peaks, b_1 and b_2. For sample#1, it exhibits the same characteristic as anatase TiO_2, providing further confirmation of the XRD results indicating the presence of only anatase TiO_2 after ball-milling at 150rpm for 10 hours.

Samples #2 and #3 exhibit similar peak features to the reference anatase TiO_2 in the XANES region, with the exception of peak b, as shown in Figure 3-5 b. The distinctive difference observed at peak

b is a result of the presence of mixed phases in the products with anatase phase on the surface. Despite this, the splitting in peak b remains apparent, indicating that the local and long-range tetragonal distortion at Ti site remains same and the electronic and structural environments at the Ti site within the TiO_6 octahedron remain unchanged. However, due to the presence of both anatase and rutile phases in the products, the relative intensity of peaks b_1 and b_2 experiences variations. Further investigation of the products through quantitative analysis can be conducted using the linear combination fitting (LCF) method in Athena software.

3.3.4 Linear Combination Fitting

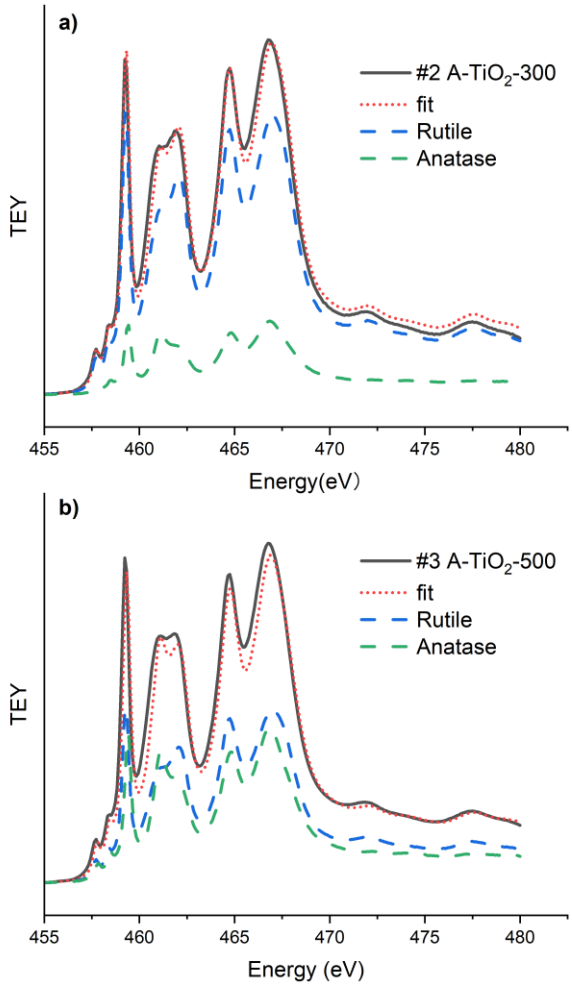

Figure 3-6. Linear Combination Fitting of XAS spectrums at the Ti $L_{3,2}$-edge of a) sample #3 (A-TiO_2-300) b) samples #5 (A-TiO_2-500) c) sample #4 (R-TiO_2-300) d) sample #6 (R-TiO_2-500) and reference anatase and rutile TiO_2

Linear combination fitting (LCF) has been used to study an XANES spectra obtained from an unidentified sample can be expressed as a linear combination of two or more spectra derived from known structures[24]. The principle of linear combination analysis is straightforward, it involves mathematically fitting the unknown spectra with reference standards XANES using a least-squares fitting approach[25]. As a result, linear combination analysis proves highly effective in determining the relative quantities of known constituents present in the sample under investigation[24].

The relative compositional ratio of the individual components within the ball-milling samples can determined using the LCF method. Figure 3-6 a and b present the results of linear fitting for sample #2 and #3, respectively. The red dash-dotted curve represents the fitting curve, the black dash-dotted curve corresponds to the experimental data of samples, the green dash-dotted curve represents the reference anatase TiO_2, and the blue dash-dotted curve is the reference rutile TiO_2. The fitting curves show excellent agreement with the experimental data, and the weight ratio of rutile TiO_2 to anatase TiO_2 is approximately 0.715 for sample #2, and 1.320 for sample#3. It is noteworthy that sample#2 and sample#3 share the same precursor but differ in their ball-milling rates, resulting in an increase in the weight ratio from 0.715 to 1.320. In conclusion, a higher ball-milling speed correlates with a higher rutile-to-anatase weight ratio. It should be noted that the anatase is present on the surface as XRD indicates a dominant rutile structure.

3.3.5 Conclusion

In conclusion, a phase transition from anatase to rutile was observed during the ball-milling process at 300 and 500 rpm albeit occurring on the surface. The findings from XRD, XANES and LCF collectively confirm the existence of both anatase and rutile phases. Additionally, with an increase in the ball-milling rate, there is a corresponding increase in the rutile-to-anatase ratio. This finding allows for the control of anatase and rutile ratio by ball milling in catalysts design.

3.4 Ball-milling mixed phased in various rate

To further validate the previous findings presented above, mixed-phase samples of TiO_2 with anatase-to-rutile ratio of 1:1 were subjected to the same synthesis method. The resulting products underwent comprehensive characterization using techniques such as TEM, SEM, XRD, XANES, and LCF for in-depth analysis.

3.4.1 Morphology

Figure 3-7 illustrates the morphology of sample #7 (A+R) TiO_2-mix, revealing nanoparticles with an approximate diameter of 50 nm. The nanoparticles can be described as exhibiting characteristics of both anatase and rutile TiO_2. The boundaries between different particles are clearly observed. Upon comparison with the SEM of reference anatase TiO_2 and rutile TiO_2 (Fig. S-1), no significant differences in size and surface characteristics are observed.

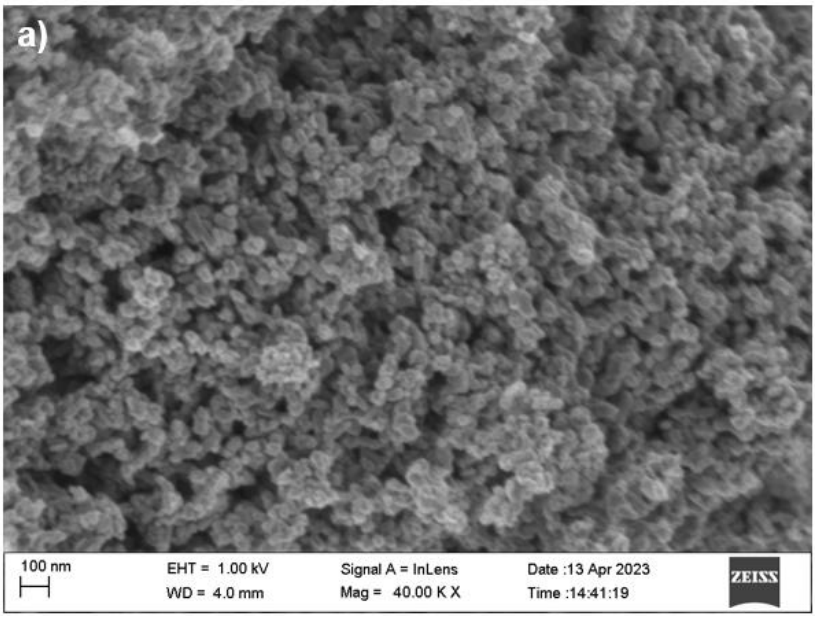

Figure 3-7. SEM images with an acceleration voltage of 1 kV and a magnification of 40.00 kx for sample #4 (A+R) TiO_2-mix

The TEM images of samples #5 (A+R) TiO_2-300 and sample #6 (A+R) TiO_2-500 are shown in Figure 3-8 a and b, respectively. The size of nanoparticles ranges approximately from 20 to 50 nm. Following ball-milling at 300rpm or 500 rpm for 10h, the size of the mixed-phase TiO_2 nanoparticles decreased. Besides that, the nanoparticles aggregated, leading to the formation of bulkier structures, and the boundaries between different particles become less distinct.

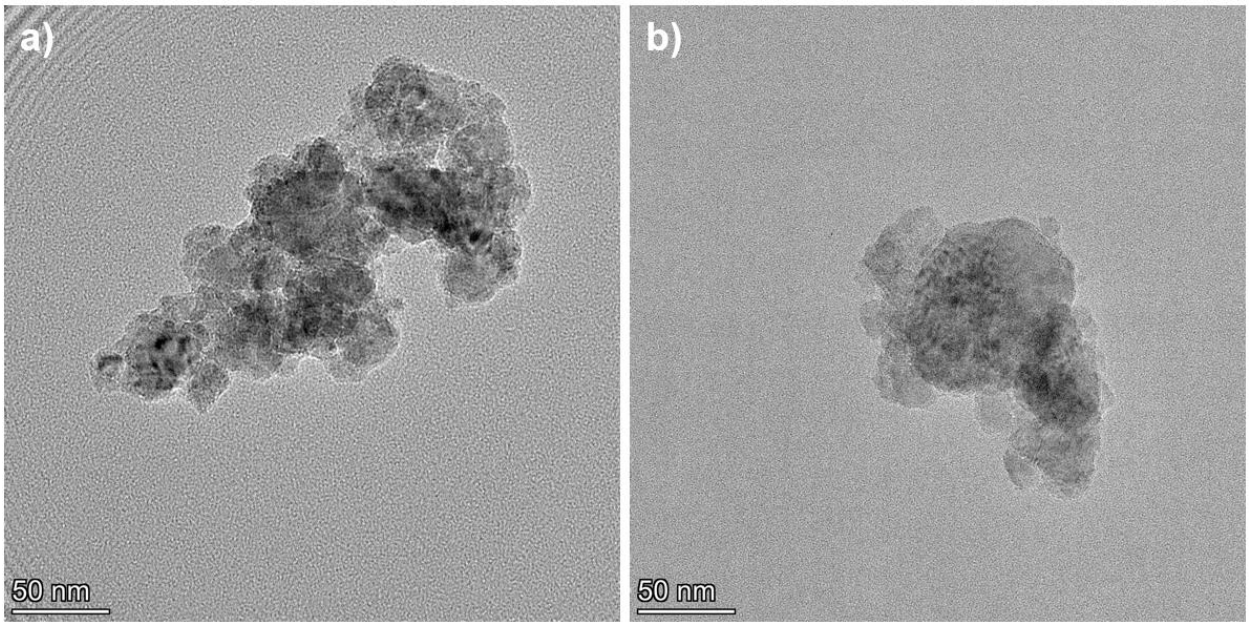

Figure 3-8. TEM images with a magnification of 190 Kx of a) sample#5 (A+R) TiO_2-300 b) sample #6 (A+R) TiO_2-500

3.4.2 Chemical Composition

In order to validate the existence of phase transition process and novel chemical compounds, XRD analysis is employed to verify the chemical composition within the samples. The utilization of standard PDF cards enables the identification of these chemical compound through comparative analysis.

Figure 3-9 represents the XRD analysis results of sample #4 (A+R) TiO_2-mix, sample#5 (A+R) TiO_2-300 and sample #6 (A+R) TiO_2-500. In the unprocessed sample #4, signals corresponding to both anatase and rutile TiO_2 have been detected. In sample #5 and #6, signals from anatase and rutile TiO_2 were also detected. However, the relative area of rutile is significantly higher than anatase, indicating a higher degree of crystallinity for the rutile phase compared to anatase. Furthermore, the integrated area of the rutile peak exceeds that of anatase, suggesting a higher concentration of rutile in comparison to anatase.

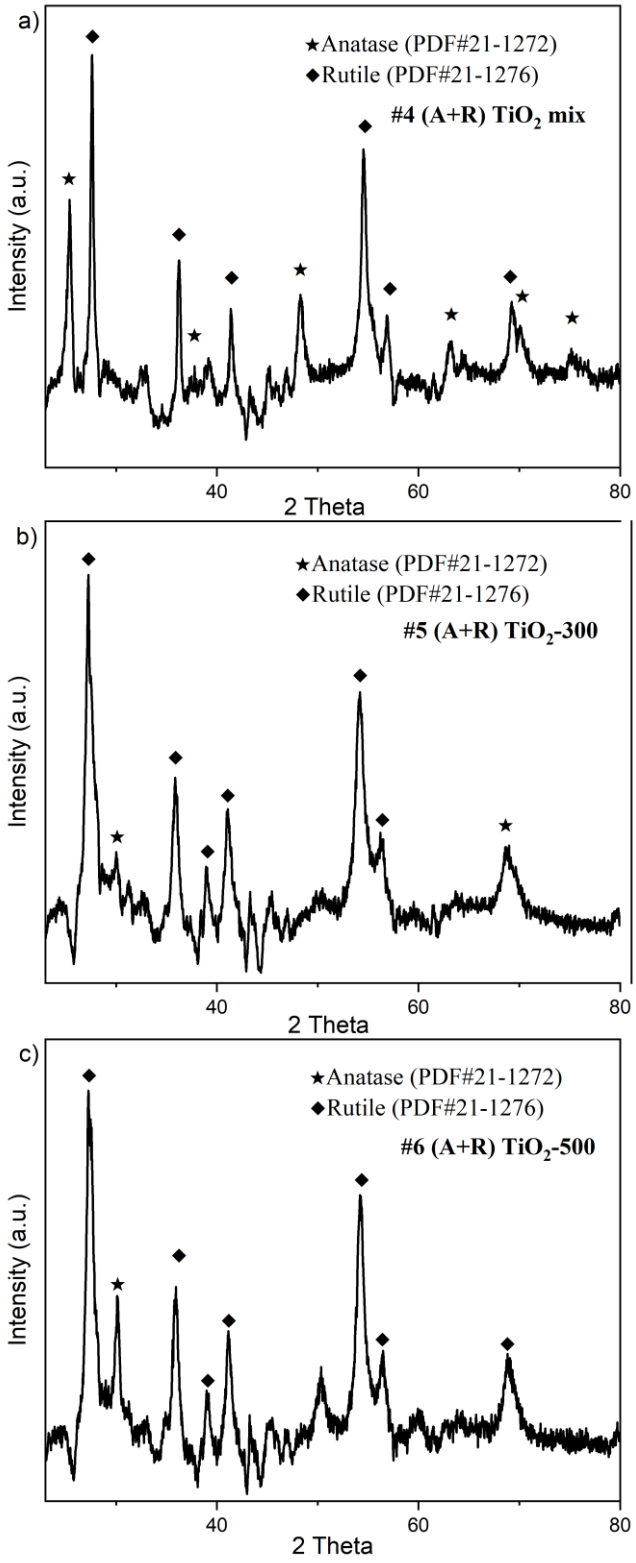
a)
★Anatase (PDF#21-1272)
◆Rutile (PDF#21-1276)
#4 (A+R) TiO2 mix
Intensity (a.u.)
40
60
80
2 Theta
b)
★Anatase (PDF#21-1272)
◆Rutile (PDF#21-1276)
#5 (A+R) TiO2-300
Intensity (a.u.)
40
60
80
2 Theta
c)
★Anatase (PDF#21-1272)
◆Rutile (PDF#21-1276)
#6 (A+R) TiO2-500
Intensity (a.u.)
40
60
80
2 Theta

Figure 3-9. XRD spectrums of a) sample #4 (A+R) TiO_2-mix b) sample#5 (A+R) TiO_2-300 c) sample #6 (A+R) TiO_2-500 with anatase TiO_2 PDF #21-1272 and rutile TiO_2 PDF #21-1276

3.4.3 XANES analysis

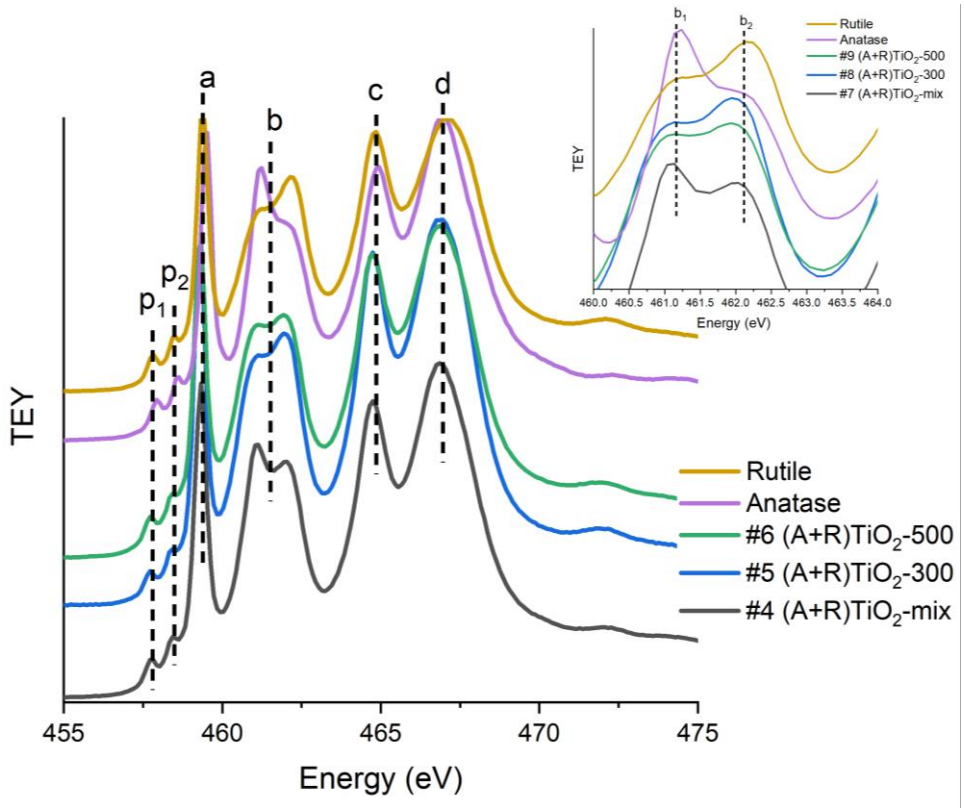

Figure 3-10. XAS spectrums and zoom-in XAS spectrums at the Ti $L_{3,2}$-edge of a) samples 4,5,6 [(A+R) TiO_2-mix, (A+R) TiO_2-300, (A+R) TiO_2-500] and reference anatase and rutile TiO_2.

As introduced in the previous study, each peak observed in XANES represents the local environment of Ti atom. Figure 3-10 illustrates the XANES spectra of sample#4, #5, and #6, aligned with reference anatase and rutile TiO_2, aiming to investigate the electronic and structural changes in the products. All three samples exhibit similar peak features to the reference data, expect for peak b. In sample #4, the peak b shows the anatase-like feature. In contrast, sample#5 and #6 show the rutile-like feature. The splitting within peak b remains apparent, indicating the persistence of electronic and structural environments at the Ti site within the distorted, rutile like

TiO_6 environment. However, due to the coexistence of anatase and rutile phases in the products, the relative intensity of peaks b_1 and b_2 demonstrates variations. To further investigate the products, quantitative analysis can be conducted using the linear combination fitting (LCF) method.

3.4.4 Linear Combination Fitting

As introduced in previous study, the LCF method allows for the relative compositional ratio of each component present in the modified samples. In Figure 3-11, the fitting curves (red dotted line) exhibit remarkable concordance with the experimental data (black dotted line), and the weight ratio of rutile TiO_2 to anatase TiO_2 is approximately 0.990 for sample #4, 2.304 for sample #5, and 2.377 for sample#6. All three samples share the same precursor but differ in their ball-milling rates. It further approves that a higher ball-milling speed correlates with a higher rutile-to-anatase weight ratio.

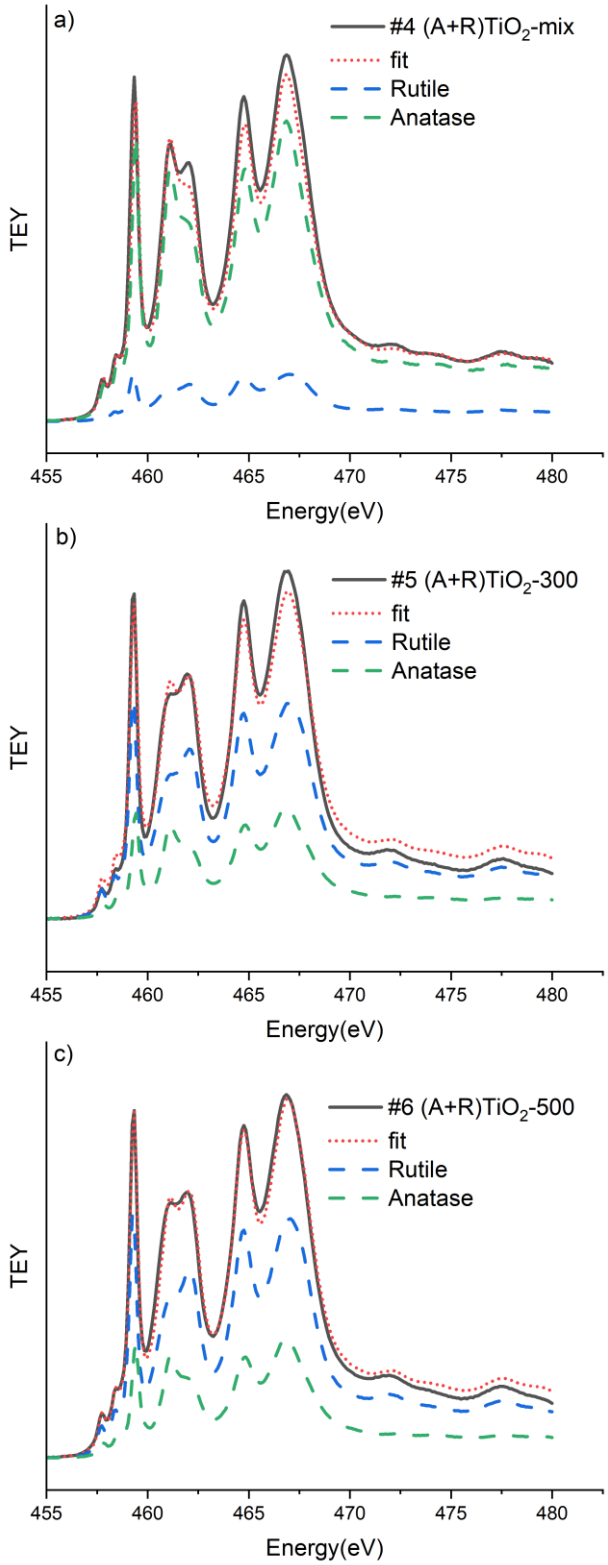
a)
#4 (A+R)TiO2-mix
fit
Rutile
Anatase
TEY
455
460
465
470
475
480
Energy(eV)
b)
#5 (A+R)TiO2-300
fit
Rutile
Anatase
TEY
455
460
465
470
475
480
Energy(eV)
c)
#6 (A+R)TiO2-500
fit
Rutile
Anatase
TEY
455
460
465
470
475
480
Energy(eV)

Figure 3-11. Linear Combination Fitting of XAS spectrums at the Ti $L_{3,2}$-edge of a) sample #4 (A+R) TiO_2-mix b) sample#5 (A+R) TiO_2-300 c) sample #6 (A+R) TiO_2-500 and reference anatase and rutile TiO_2

3.5 Summary

In the case of single-precursor systems, ball-milling serves as an environmentally friendly synthesis method that triggers phase transitions. To further validate the occurrence of phase transitions during sample modification process, a mixed-precursors system was employed. The ball-milling process successfully induced phase transitions, and as the ball-milling rate increased, the ratio of anatase-to-rutile decrease. These results were corroborated by the XRD, SEM, TEM, XANES techniques. The relative composition ratio was determined using the LCF method in Athena software.

3.6 Reference

1. Gázquez, M. J., Bolívar, J. P., Garcia-Tenorio, R., Vaca, F. (2014). A review of the production cycle of titanium dioxide pigment. Materials Sciences and Applications, 05(07), 441–458. https://doi.org/10.4236/msa.2014.57048
2. Testoni, G. O., Amoresi, R. A. C., Lustosa, G. M. M. M., Costa, J. P. C., Nogueira, M. V., Ruiz, M., Zaghete, M. A., Perazolli, L. A. (2018a). Increased photocatalytic activity induced by TiO_2/Pt/SnO_2 heterostructured films. Solid State Sciences, 76, 65–73. https://doi.org/10.1016/j.solidstatesciences.2017.12.006
3. Foo, C., Li, Y., Lebedev, K., Chen, T., Day, S., Tang, C., Tsang, S. C. (2021). Characterisation of oxygen defects and nitrogen impurities in TiO_2 photocatalysts using variable-temperature X-ray powder diffraction. Nature Communications, 12(1). https://doi.org/10.1038/s41467-021-20977-z
4. Madian, M., Eychmüller, A., Giebeler, L. (2018). Current advances in TiO_2-based nanostructure electrodes for high performance lithium-ion batteries. Batteries, 4(1), 7. https://doi.org/10.3390/batteries4010007
5. Wang, Ying, Jia, W., Strout, T., Schempf, A., Zhang, H., Li, B., Cui, J., Lei, Y. (2009). Ammonia gas sensor using polypyrene-coated TiO_2/ZnO nanofibers. Electroanalysis, 21(12), 1432–1438. https://doi.org/10.1002/elan.200904584
6. Ricci, P. C., Carbonaro, C. M., Stagi, L., Salis, M., Casu, A., Enzo, S., Delogu, F. (2013). Anatase-to-Rutile phase transition in TiO_2 nanoparticles irradiated by Visible light. The Journal of Physical Chemistry C, 117(15), 7850–7857. https://doi.org/10.1021/jp312325h
7. Ohno, T., Tokieda, K., Higashida, S., Matsumura, M. (2003a). Synergism between rutile and anatase TiO_2 particles in photocatalytic oxidation of naphthalene. Applied Catalysis A: General, 244(2), 383–391. https://doi.org/10.1016/s0926-860x(02)00610-5
8. Jia, J., Ohno, T., Matsumura, M. (2000a). Efficient dihydroxylation of naphthalene on photoirradiated rutile TiO_2 powder in solution containing hydrogen peroxide. Chemistry Letters, 29(8), 908–909. https://doi.org/10.1246/cl.2000.908
9. Byrne, C., Fagan, R., Hinder, S., McCormack, D. E., Pillai, S. C. (2016a). New approach of modifying the anatase to rutile transition temperature in TiO_2 photocatalysts. RSC Advances, 6(97), 95232–95238. https://doi.org/10.1039/c6ra19759k
10. Pillai, S. C., Periyat, P., George, R., McCormack, D. E., Seery, M. K., Hayden, H., Colreavy, J., Corr, D., Hinder, S. J. (2007a). Synthesis of high-temperature stable anatase TiO_2 photocatalyst. The Journal of Physical Chemistry C, 111(4), 1605–1611. https://doi.org/10.1021/jp065933h
11. Sun, B., Vorontsov, A. V., Smirniotis, P. G. (2003a). Role of platinum deposited on TiO_2 in phenol photocatalytic oxidation. Langmuir, 19(8), 3151–3156. https://doi.org/10.1021/la0264670
12. Mills, A., Elliott, N., Parkin, I. P., O'Neill, S. A., Clark, R. J. (2002a). Novel TiO_2 CVD films for semiconductor photocatalysis. Journal of Photochemistry and Photobiology A: Chemistry, 151(1–3), 171–179. https://doi.org/10.1016/s1010-6030(02)00190-9
13. Goossens, A., Maloney, E.-L., Schoonman, J. (1998a). Gas-phase synthesis of nanostructured anatase TiO_2. Chemical Vapor Deposition, 04(03), 109–114.

https://doi-org.proxy1.lib.uwo.ca/10.1002/(SICI)1521-3862(199805)04:03%3C109::AID-CVDE109%3E3.0.CO;2-U
14. Ban, V., Sadikin, Y., Lange, M., Tumanov, N., Filinchuk, Y., Černý, R., Casati, N. (2017). Innovative in-situ ball mill for X-ray diffraction. Analytical Chemistry, 89(24), 13176–13181. https://doi.org/10.1021/acs.analchem.7b02871
15. Gaur, A., Shrivastava, B. D. (2015). Speciation using X-ray Absorption Fine Structure (XAFS). Review Journal of Chemistry, 5(4), 361–398. https://doi.org/10.1134/s2079978015040032
16. de Groot, F. M., Fuggle, J. C., Thole, B. T., Sawatzky, G. A. (1990). $L_{2,3}$ X-ray-absorption edges of d^0 compounds: K^+, Ca^{2+}, Sc^{3+}, and Ti^{4+} in O_h (octahedral) symmetry. Physical Review B, 41(2), 928–937. https://doi.org/10.1103/physrevb.41.928
17. Chen, S. C., Sung, K. Y., Tzeng, W. Y., Wu, K. H., Juang, J. Y., Uen, T. M., Luo, C. W., Lin, J.-Y., Kobayashi, T., Kuo, H. C. (2013). Microstructure and magnetic properties of oxidized titanium nitride thin filmsin situgrown by pulsed laser deposition. Journal of Physics D: Applied Physics, 46(7), 075002. https://doi.org/10.1088/0022-3727/46/7/075002
18. Crocombette, J. P., Jollet, F. (1994). Ti 2p X-ray absorption in Titanium Dioxides (TiO_2): The influence of the cation site environment. Journal of Physics: Condensed Matter, 6(49), 10811–10821. https://doi.org/10.1088/0953-8984/6/49/022
19. de Groot, F. M., Faber, J., Michiels, J. J., Czyżyk, M. T., Abbate, M., Fuggle, J. C. (1993). Oxygen 1s X-ray absorption of Tetravalent Titanium Oxides: A comparison with single-particle calculations. Physical Review B, 48(4), 2074–2080. https://doi.org/10.1103/physrevb.48.2074
20. Li, J., Liu, L., Sham, T.-K. (2015). 2d XANES–XEOL spectroscopy studies of morphology-dependent phase transformation and corresponding luminescence from hierarchical TiO_2 nanostructures. Chemistry of Materials, 27(8), 3021–3029. https://doi.org/10.1021/acs.chemmater.5b00363
21. Harada, Y., Watanabe, M., Eguchi, R., Ishiwata, Y., Matsubara, M., Kotani, A., Yagishita, A., Shin, S. (2001). Polarization dependence of the soft x-ray Raman scattering at the L edge of TiO_2. Journal of Electron Spectroscopy and Related Phenomena, 114–116, 969–973. https://doi.org/10.1016/s0368-2048(00)00374-1
22. de Groot, F. M., Fuggle, J. C., Thole, B. T., Sawatzky, G. A. (1990a). 2p X-ray Absorption of 3d Transition-Metal Compounds: An Atomic Multiplet Description including the Crystal Field. Physical Review B, 42(9), 5459–5468. https://doi.org/10.1103/physrevb.42.5459
23. Kucheyev, S. O., van Buuren, T., Baumann, T. F., Satcher, J. H., Willey, T. M., Meulenberg, R. W., Felter, T. E., Poco, J. F., Gammon, S. A., Terminello, L. J. (2004). Electronic Structure of Titania Aerogels from Soft X-ray Absorption Spectroscopy. Physical Review B, 69(24). https://doi.org/10.1103/physrevb.69.245102
24. Calvin, S., Furst, K. E. (2018). XAFS for everyone. CRC Press, an imprint of Taylor Francis Group.
25. Ravel, B., Newville, M. (2005). ATHENA, ARTEMIS, HEPHAESTUS: Data Analysis for X-ray Absorption Spectroscopy Using IFEFFIT. Journal of Synchrotron Radiation, 12(4), 537–541. https://doi.org/10.1107/s090904950501271

Chapter 4

Chapter 4. XANES and XEOL studies of ball-milling TiO_2/ZnO and TiO_2/SnO_2 heterostructures

This chapter presents a study of the influence of various ball-milling rates in forming TiO_2/ZnO heterostructures and exploring the electron transfer between TiO_2/ZnO and TiO_2/SnO_2 heterojunctions. The SEM, TEM, EDX, XANES, XES, and 2D-XANES-XEOL of ball-milling samples will be discussed.

4.1 Introduction

Heterogenous photocatalysis is acknowledged as a clean technology capable of addressing the degradation of organic wastes. This is due to its ability to destroy and convert organic compounds into water, carbon dioxide, and inorganic anions[1,2]. Semiconductors, which are critical materials for facilitating heterogeneous photocatalysis, include titanium dioxide (TiO_2), zinc oxide (ZnO) and tin dioxide (SnO_2), widely appreciated for their superior photocatalytic performance[3,4]. In the ball-milling process, the milling rate is a crucial factor in the formation of heterostructures. Moreover, ball milling is extensively utilized in the industry for mechanochemical reactions as an eco-friendly synthetic method[5].

This project aims to investigate the influence of various ball-milling rates on the formation of TiO_2/ZnO heterostructures and explore the electron transfer between TiO_2/ZnO and TiO_2/SnO_2 heterojunctions. Techniques such as Scanning Electron Microscopy (SEM) and Transmission Electron Microscopy (TEM) are applied to examine the morphology and crystal structure of the heterostructures. Additionally, X-ray diffraction (XRD) analysis is incorporated as part of the characterization process to determine the crystal structure and chemical compositions of the products. Moreover, the chemical environments of elements and the electron transfers between heterojunctions can be determined by using synchrotron techniques. The X-ray Absorption Spectroscopy (XAS), X-ray Emission Spectroscopy (XES), and 2D X-ray Absorption Near Edge Structure-X-ray Excited Optical Luminescence (2D-XANES-XEOL) spectra can reveal the changes in the chemical environments of specific elements across various chemicals. This, in turn, can be instrumental in portraying the alterations in crystal structure.

4.2 Experimental section

4.2.1 TiO_2/ZnO and TiO_2/SnO_2 heterostructure synthesis

4.2.1.1 Materials

Anatase titanium (IV) oxide (TiO_2, nanopowder, <25 nm particle size, 99.7% trace metals basis), Rutile titanium (IV) oxide (TiO_2, nanopowder, <100 nm particle size, 99.5% trace metals basis), zinc oxide (ZnO, nanopowder, <100 nm particle size), and Tin (IV) oxide (mesh 99.9%), were commercial products, which were purchased from Sigma Aldrich. All chemicals were used without further purification.

4.2.1.2 Synthesis method

Weighted amounts of commercial nanosized powder of any two types out of a total of four distinct chemical compounds (anatase TiO_2, rutile TiO_2, ZnO and SnO_2), in the stoichiometric molar ratio of 1:1 totaling 1g, were added into a 125 mL zirconium dioxide (ZrO_2) grinding jar with a set of ZrO_2 grinding balls. The ball-milling jars, shown in Figure 4-1, were evacuated to keep the reactants in a vacuum state. The milling speeds were varied, being set at 100, 150, 300, and 500 rpm on the Planetary Ball Mill PM 200 for different experimental conditions. The ball milling process was maintained for 10 hours. After grinding, samples were collected and characterized as presented in Table 4-1.

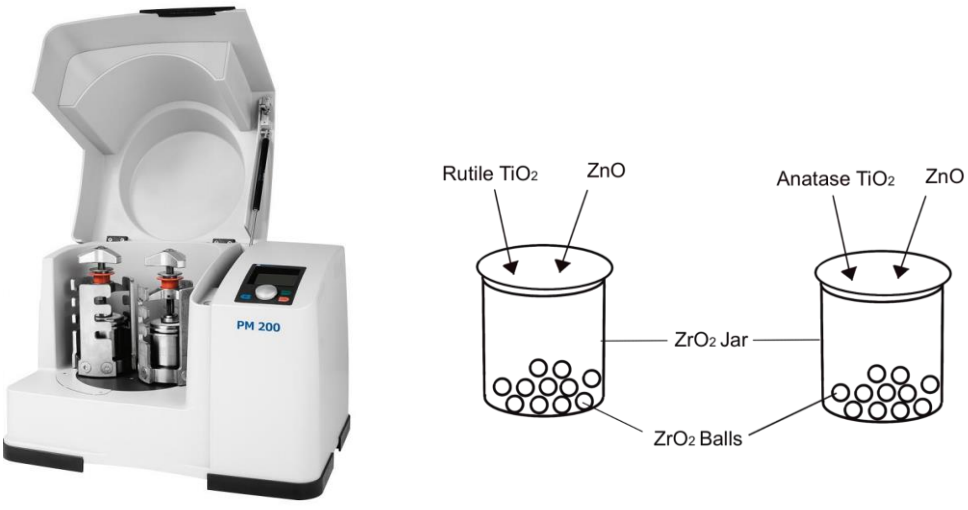

a) b)

Figure 4-1. a) Planetary Ball Mill PM 200 image from Retsch.com b) 125 mL Ball mill jars

Table 4-1. Samples synthesized with different conditions.

Sample ID	Precursor Type	Ball Mill Speed	Ball Mill Time	Full Name
#1	Anatase TiO_2 & ZnO	150 rpm	10 h	A-TiO_2-ZnO-150
#2	Rutile TiO_2 & ZnO	150 rpm	10 h	R-TiO_2-ZnO-150
#3	Anatase TiO_2 & ZnO	300 rpm	10 h	A-TiO_2-ZnO-300
#4	Rutile TiO_2 & ZnO	300 rpm	10 h	R-TiO_2-ZnO-300
#5	Anatase TiO_2 & ZnO	500 rpm	10 h	A-TiO_2-ZnO-500
#6	Rutile TiO_2 & ZnO	500 rpm	10 h	R-TiO_2-ZnO-500
#7	Anatase TiO_2 & SnO_2	150 rpm	10 h	A-TiO_2-SnO_2-150
#8	Rutile TiO_2 & SnO_2	150 rpm	10 h	R-TiO_2-SnO_2-150

4.2.2 Characterization

Same characterization techniques as Chapter 3 were used in this chapter. Moreover, EDX and WIEN analysis were employed in this project.

The constituent chemical elements, sample morphology, and crystalline structure were investigated using SEM (Zeiss-LEO 1530 Gemini FE-SEM), TEM, TEM-EDX, and PXRD. Technical support for TEM (Thermo Scientific Talos 200X) and TEM-EDX (Thermo Scientific Talos L120C with a Bruker XFlash 6TI30 EDS detector) were provided by the Canadian Center for Electron Microscopy (CCEM) at McMaster University, while PXRD (Inel CPS Powder Diffractometer, Cu Kα radiation with 2θ=1.5) was supported by the X-ray facility at Western University.

The XANES data were acquired at the SGM and REIXS beamlines, at the Canadian Light Source (CLS) in Saskatoon, SK, Canada. Concurrently, XES and XEOL measurements were taken. All XANES and XEOL spectra were normalized to the incident photon flux, thereby ensuring the comparability of the results obtained in this study.

Results and discussions

4.3 Ball-milling rate-dependent TiO_2/ZnO heterostructure

4.3.1 Morphology

Heterojunctions in semiconductors, as the interfaces between differing chemical compositions, can be discerned through SEM and TEM imagery. The formation of heterostructures is confirmed in sample #1 (Figure 4-2a) and #2 (Figure 4-2b), both exhibiting a hierarchical morphology with nanoparticle structures. According to the SEM images (Appendix A) from commercial anatase TiO_2, rutile TiO_2 and ZnO, the small nanoparticles with a diameter of approximately 50 nm could be attributed to either the anatase or rutile precursor, whereas the larger nanoparticle structure could be attributed to ZnO. These observations suggest that ball-milling at a lower rotation speed effectively combines anatase TiO_2 and ZnO, facilitating the formation of heterostructures. It was observed that most particles had a tendency to aggregate, leading to the formation of larger clusters.

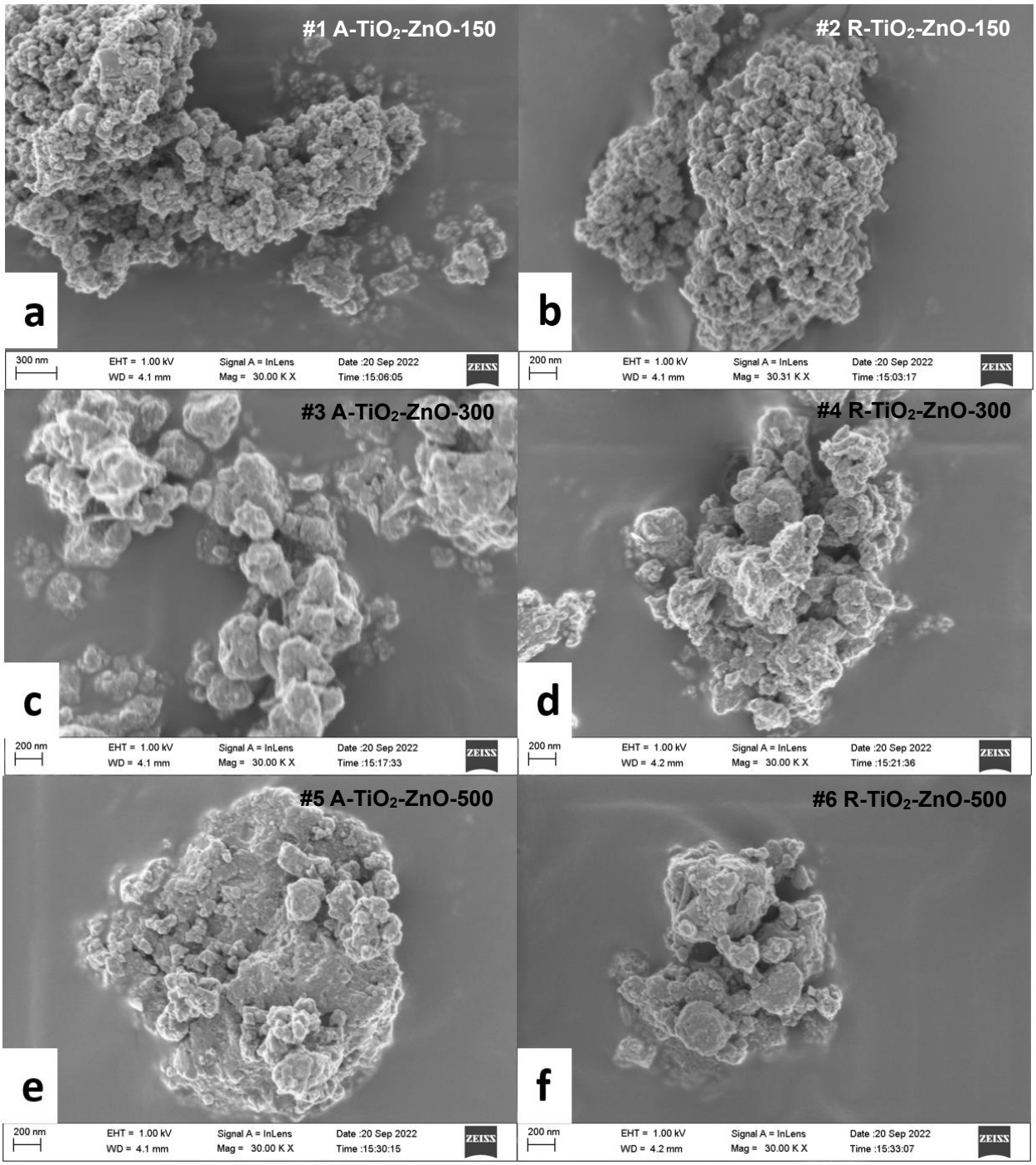

Figure 4-2. SEM images with an acceleration voltage of 1 kV and a magnification of 30000 for ***(a)*** *#1 A-TiO_2-ZnO-150* ***(b)*** *#2 R-TiO_2-ZnO-150* ***(c)*** *#3 A-TiO_2-ZnO-300* ***(d)*** *#4 R-TiO_2-ZnO-300* ***(e)*** *#5 A-TiO_2-ZnO-500* ***(f)*** *#6 R-TiO_2-ZnO-500*

Figure 4-3 presents HR-TEM images illustrating the morphology and crystal structure of ball-milling rutile TiO_2/ZnO heterojunction, produced at a rate of 150 rpm (sample#2). As depicted in Figure 4-3a, post-modification, a ZnO nanoparticle with diameters about 70-80 nm adheres to the surface of the TiO_2 nanoparticle, creating a heterostructure. This is in agreement with the findings from SEM images (Figure 4-2b).

A more detailed look using High-Resolution Transmission Electron Microscopy (HRTEM) of ZnO, depicted in Figure 4-3b, reveals a lattice spacing of 0.246 nm, indicative of the (101) plane of ZnO[6,7]. Furthermore, in Figure 4-3c, the lattice space of 0.326 nm is attributed to the (110) plane of rutile TiO_2[8].

The SEM images of samples 3-6 (Figure 4-2 c,d,e,f) display differences compared to the first two samples. The presence of tiny anatase or rutile nanoparticles and ZnO nanoparticles is less apparent due to limited quantities. Conversely, particles of considerably larger size and irregular shapes are observed, likely resulting from the reaction of TiO_2 and ZnO to form new compounds at higher rotation speeds during the ball-milling process.

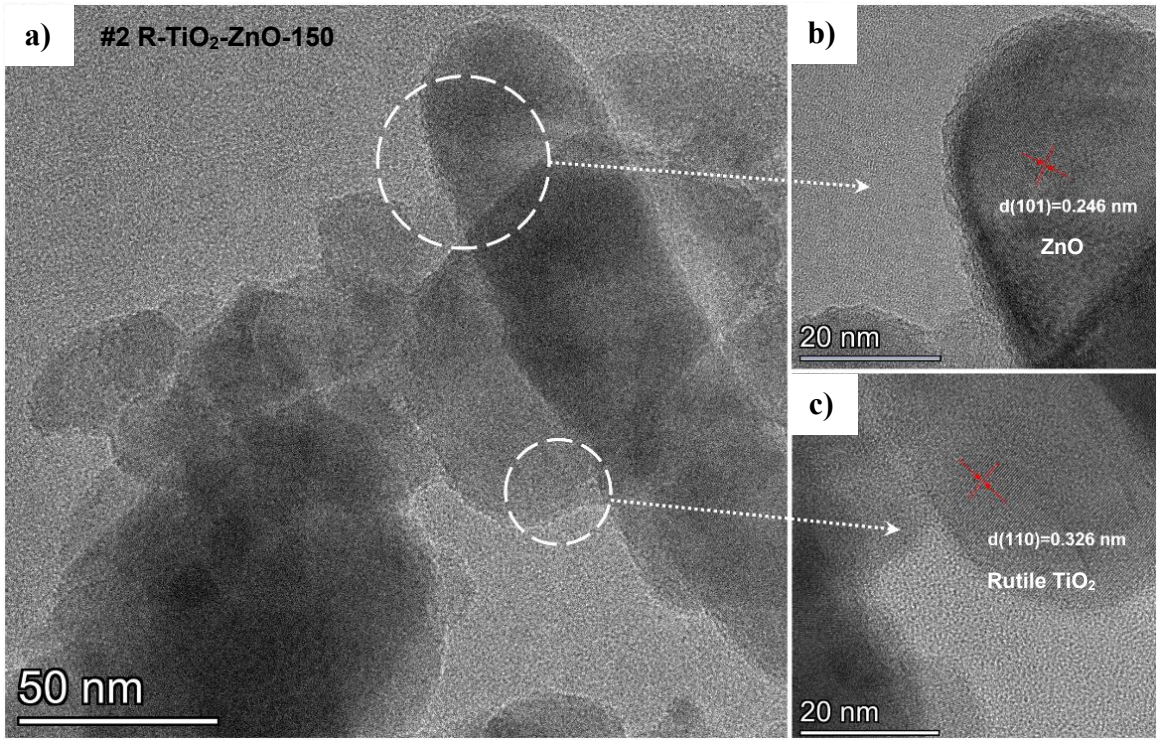

Figure 4-3. HR-TEM images of sample #2 a) with a magnification of 245 kx b) and c) with a magnification of 630 kx

TEM-EDX images can provide the elemental distribution in the sample. The TEM-EDX elemental mapping of sample#2 (Fig. 4-4), it provides that Ti and Zn elements are uniformly distributed in sample #2. The atomic ratio of Ti: Zn is close to 1:1, which provides the distribution of heterostructures uniformly in the samples.

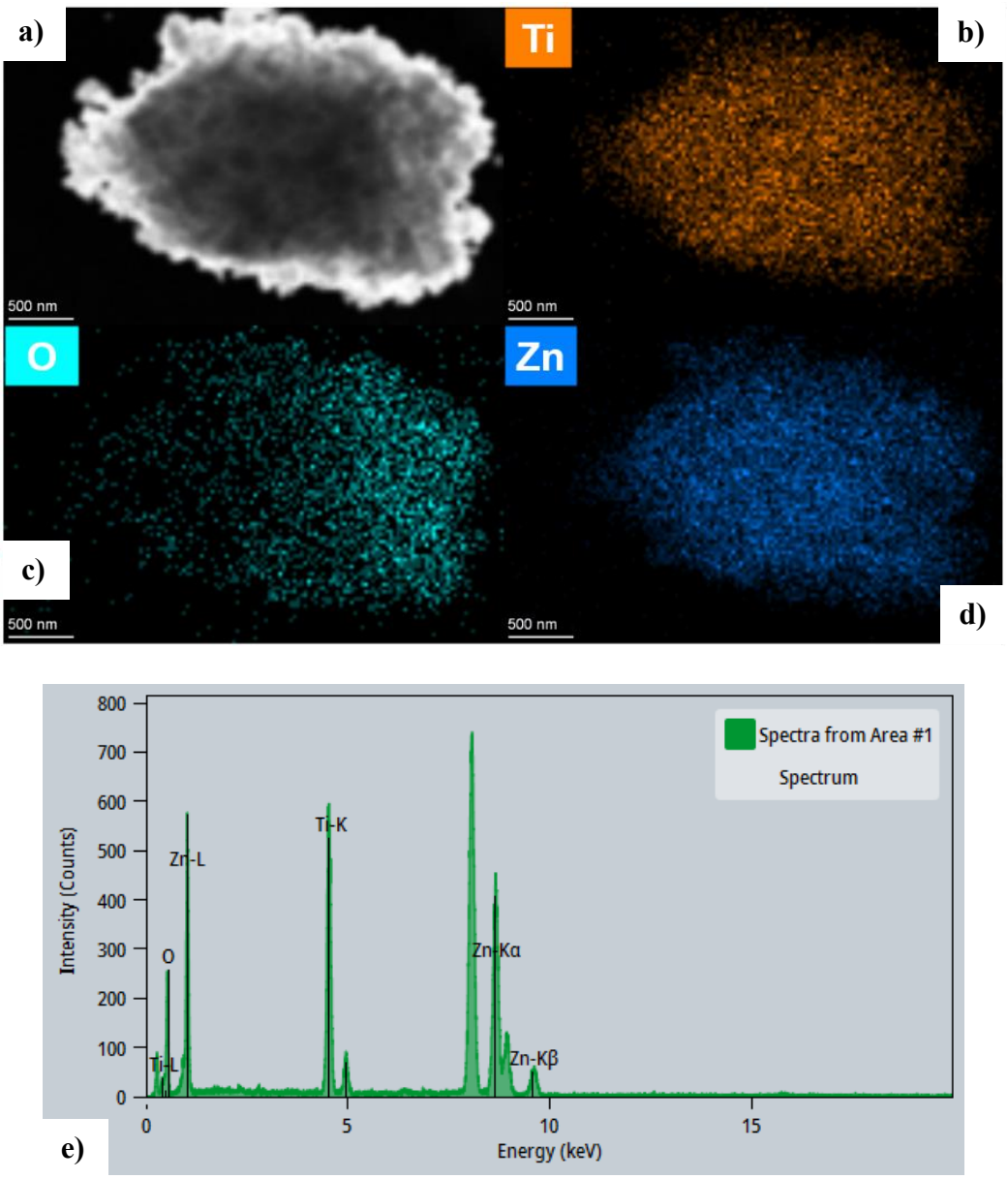

Figure 4-4. TEM-EDX elemental mapping of sample #2 of a) TEM-EDX image b) Ti elemental mapping c) O elemental mapping d) Zn elemental mapping e) an EDX spectrum

4.3.2 Chemical composition

To further corroborate the presence of heterostructures and novel chemical compounds, XRD analysis serves as an essential step to validate the chemical compositions of the samples. The identities of these chemical compounds can be verified by comparing the products thus obtained with standard PDF cards. In the case of samples #1 and #2 (figure 4-5 a and b), only signals from precursors were detected, which is consistent with the results derived from SEM analyses. This indicates that the majority of the precursors retained their original chemical composition but form heterojunctions between ZnO and TiO_2 when subjected to lower ball milling speeds.

For samples #3 and #4, the emergence of new compounds was confirmed as the XRD spectrum revealed peaks characteristic of $ZnTiO_3$ and Zn_2TiO_3 (as shown in Figure 4-5a). Notably, no matched peaks corresponding to the precursors were observed. This suggests that a complete reaction between TiO_2 and ZnO occurred under the conditions of high-speed ball-milling, specifically at a rotation speed of 300 rpm.

In the case of sample #5 and #6, analogous to samples #3 and #4, all precursors were transformed into new compounds. As inferred from Figure 4-6, a new crystal $ZnTiO_3$, is presented in sample #5 and #6.

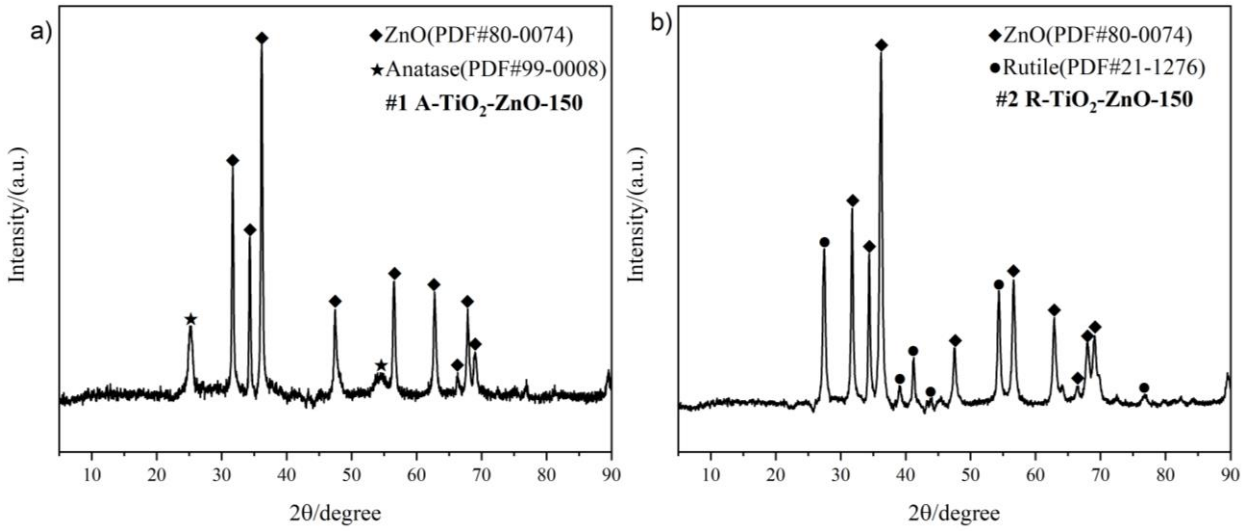

Figure 4-5. XRD images of a) sample #1 with ZnO PDF #80-0074 and anatase TiO_2 PDF #99-0008 b) sample #2 with ZnO PDF #80-0074 and rutile TiO_2 PDF #21-1276

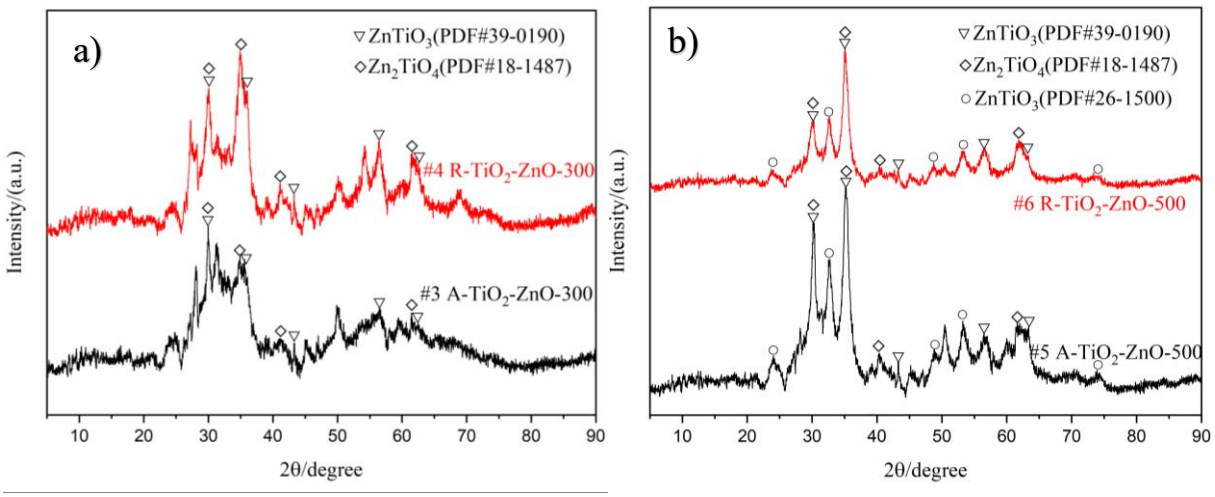

Figure 4-6. XRD images of a) samples 3-4 with $ZnTiO_3$ PDF#39-0190 and Zn_2TiO_4 PDF#18-1487 b) samples 5-6 with $ZnTiO_3$ PDF#39-0190, Zn_2TiO_4 PDF#18-1487 and ZnO_3 PDF#26-1500

4.3.3 XANES & XES analysis

The XANES (XAS) experiments in this section were carried out at the Spherical Grating Monochromator (SGM) beamline, situated at the Canadian Light Source (CLS) within the University of Saskatchewan in Saskatoon. The XES experiments in this section were carried out at the Resonant Elastic and Inelastic X-ray Scattering (REIXS) beamline, also situated at CLS.

The efficacy of XANES is anchored in its extraordinary sensitivity to the electronic structures of the samples under investigation. Further analysis of the XAS spectra allows utilizing more data on the strength and symmetry of the crystal field, hybridization, as well as the oxidation state of the specific ion under consideration, such as Ti and Zn ions.

To differentiate further the chemical environment changes and electronic structure in heterostructure samples, and the defects in the heterojunctions, a combined analysis of the XAS and XES spectra is essential. Moreover, electron transfer can be tracked by XEOL. XAS spectra were generated for samples 1-6 across the Ti $L_{3,2}$-edge, Zn $L_{3,2}$-edge and O K-edge. XES spectra was collected for samples 3-6 from the Zn $L_{3,2}$-edge.

4.3.3.1 XAS spectra at the Ti $L_{3,2}$-edge

Figure 4-7 presents the XAS spectra of the anatase and rutile TiO_2 precursors and of the final TiO_2/ZnO heterostructures synthesized via the ball milling process at various speed rates (sample 1-6) in TEY detection mode. Moreover, the inset images in the XAS spectra were performed for detailed information. Figure 4-7a generate the XAS spectra and inset XAS spectra of sample #1, #3 and #5 reference anatase TiO_2 and rutile TiO_2, samples #1, #3 and #5 have the same precursor anatase TiO_2. Figure 4-7b generate the XAS spectra and inset XAS spectra of samples #2, #4, and #6, reference anatase TiO_2 and rutile TiO_2, samples #2, #4 and #6 have the same precursor rutile TiO_2.

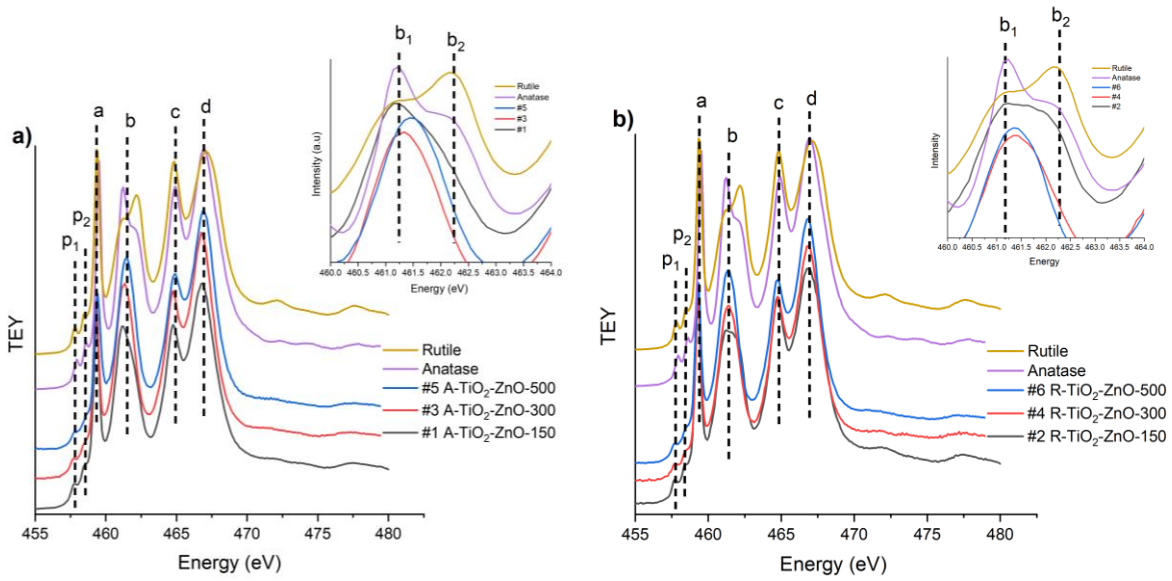

Figure 4-7. XAS spectra and inset XAS spectra at the Ti $L_{3,2}$-edge of a) samples 1,3,5 and reference anatase and rutile TiO_2 b) sample 2,4,6 and reference anatase and rutile TiO_2.

As per discussed in Chapter 3, the XANES spectra at the Ti $L_{3,2}$-edge correspond to the excitation of electrons from the $2p_{3/2,1/2}$ core level to unoccupied 3d states of Ti atoms following dipole selection rules. These structures exhibit a complex configuration due to the combined effects of the crystal field and atomic interactions[9,10]. Pre-edge features are resulting in the core-hole-d-electron interactions[11]. The difference between peaks b_1 and b_2 serves as a distinguishing characteristic between rutile (D_{2h}) and anatase (D_{2d}) phases[12,13]. Anatase TiO_2 exhibits a more prominent b_1 peak compared to b_2, while the opposite trend is observed in rutile TiO_2.

In Figure 4-7, samples #1 and #2 exhibit mixed peak features as reference anatase TiO_2 and rutile TiO_2 respectively. However, closer inspection reveals that the peaks b_1 and b_2 merge and become less distinguishable. It is likely due to the formation of heterostructure.

In contrast, samples 3-6 present similar peak features as reference samples, except peak b, which narrows and there is no further peak splitting in, e_g orbital at Ti $L_{3,2}$-edge. It only shows as a single peak and the disappearance of the splitting suggests a higher local symmetry as often observed in $SrTiO_3$, an octahedral symmetry, which is a typical feature for titanate phases in an O_h symmetry. Because the size of Zn^{2+} is smaller than Ti^{4+}, there is a slight distortion compared to the TiO_6 octahedron[9]. There is no evidence for the existence of either anatase or rutile TiO_2 in those four samples. Since peak splitting still exist in the Ti L_3-edge (peaks a and b) and Ti L_2-edge (peaks c and d), the Ti site is in a TiO_6 octahedron. Based on the results from XRD analysis, the XANES results confirmed that a new zinc titanium compound with an octahedron Ti $^{4+}$ environment had formed.

In conclusion, the existence of heterostructure in sample #1 and #2 have been observed. For the rest of the relatively high-speed ball-milling ZnO/TiO_2 samples, new chemical compounds are formed.

4.3.3.2 XAS spectra at the O K-edge

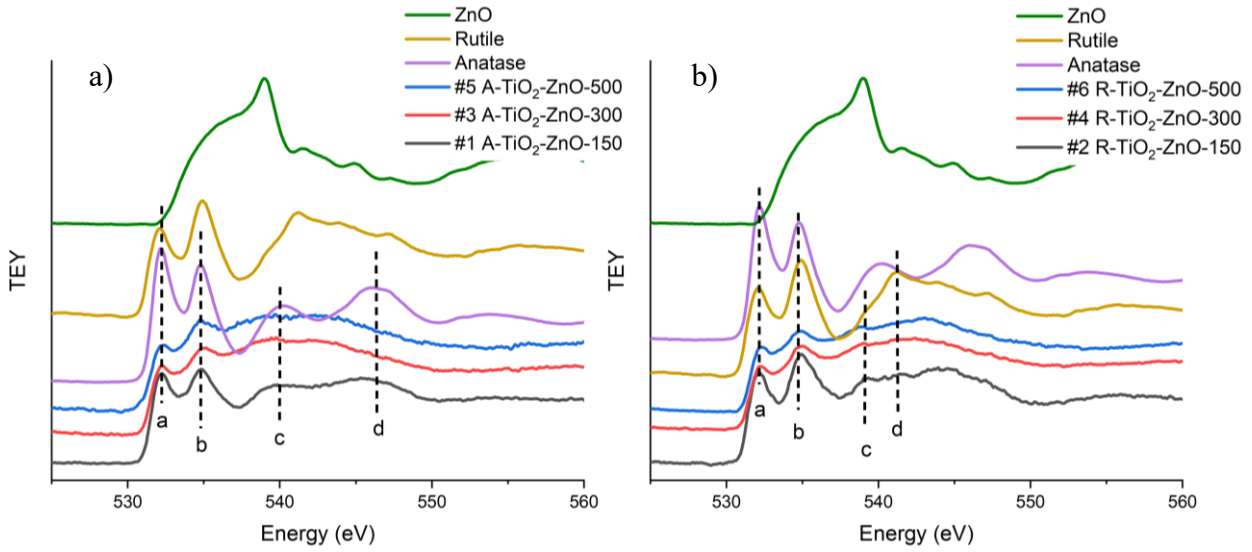

Figure 4-8. XAS spectra at the O K-edge of a) samples 1,3,5 and reference ZnO, anatase and rutile TiO_2 b) samples 2,4,6 and reference ZnO, anatase and rutile TiO_2

Figure 4-8 shows the XAS spectra of samples 1-6, reference anatase TiO_2, rutile TiO_2 and ZnO. Typically, the O K-edge is related to the electronic transition from O 1s to the unoccupied O 2p orbital, the multiple peaks originate from the hybridization of orbitals which can also be described as unoccupied densities of states of O 2p character derived from band structure calculations.

Two distinct peaks observed at photon energies of 532 eV (peak a) and 535 eV (peak b) are attributed to the electronic transition from O 1s to 2p states, which are covalently hybridized with the unoccupied split Ti 3d bands (3d-t_{2g} and 3d-e_g orbitals)[14]. The splitting peaks a and b are due to the crystal field effect, which is sensitive to the extent of orbital hybridization. The observed relative increase/decrease of peaks a and b has been previously discussed in the XAS spectra across Ti $L_{3,2}$-edge, the relatively changed electron population in the Ti 3d-t_{2g} and 3d-e_g states. Peak c and d are contributed by the Ti 2p, 4s and 4p states hybridized with the electronic transition of O 1s to O 2p orbital[15]. In detail, peak c is the origin of the antibonding state and peak D is originated from the bonding state, both peaks show dispersion effects, and it is highly sensitive to the long-range order[16–18].

In figure 4-8 a and b, samples #1 and #2 exhibit similar peak features as the reference anatase TiO_2 and rutile TiO_2, respectively. However, peaks a and b have lower intensity than the reference samples, which could be due to the Oxygen vacancies (O_{vac}) and other defects in the heterostructures. These defects could further influence on the O 2p- Ti 3d interactions[14,19]. Similarly, the decreased intensity of peaks c and d indicates the increased O_{vac} and the lack of long-range order. Another possible reason for this could be that the concentration of TiO_2 in the products is lower than reference. Similarly, the decreased intensity of peaks c and d indicates an increased number of defects and the lack of long-range order.

Differently from the first two samples, samples 3-6 present different features with the reference chemicals, which result from the formation of new chemical compounds. The chemical environment of O atoms has been changed, which results in structure distortion. However, the features of O K-edge spectrum are dominated by TiO_2. A plausible reason could be the lower hardness of ZnO (4.5 on Mohs scale) compared to anatase TiO_2 (5.5-6.0 on Mohs scale) and rutile (6.2 on Mohs scale). During the ball-milling process, parts of ZnO may become disordered and

convert to an amorphous state. In the meanwhile, Zn 3d orbitals have been fully occupied, leading to an absence of ZnO features in the samples.

Overall, the formation of heterostructure led to an increase in defects, weaker hybridization of O 2p orbitals and Ti 3d orbitals, and a lack of long-range order. Furthermore, for samples 3-6, the formation of new chemicals has been confirmed.

4.3.3.3 XAS spectra at the Zn $L_{3,2}$-edge

Figure 4-9 shows the TEY spectra for samples 3-6 and reference ZnO at Zn $L_{3,2}$-edge. The L-edge can be separated into L_1, L_2, and L_3 edges, with L_3-edge and L_2-edge being the prominent peaks presented in the spectra. According to the dipole-transition rule, electrons transition from the 2s orbital to the p orbital at the L_1 edge and from the $2p_{1/2}$ and $2p_{3/2}$ orbitals to the d and s orbitals at the L_2 and L_3 edges, respectively. As Chapter 1 mentioned previously, the DOS of ZnO (Figure 1-4) represents that in the ZnO system, the main contributor of VB is O-2p orbitals. Since the Zn-3d orbital is often filled or nearly filled, the main contributor of CB is Zn-4s/4p orbitals. As a result, the Zn $L_{3,2}$-edge XANES probes the Zinc electron transitions from O-2p to Zn-3d/4s orbital. In this case, the 3d orbital is almost completely filled and has minor character in the conduction band. In Figure 4-9, peak a represents the 4s orbital, and peak b and c represent the 4 d orbitals[20].

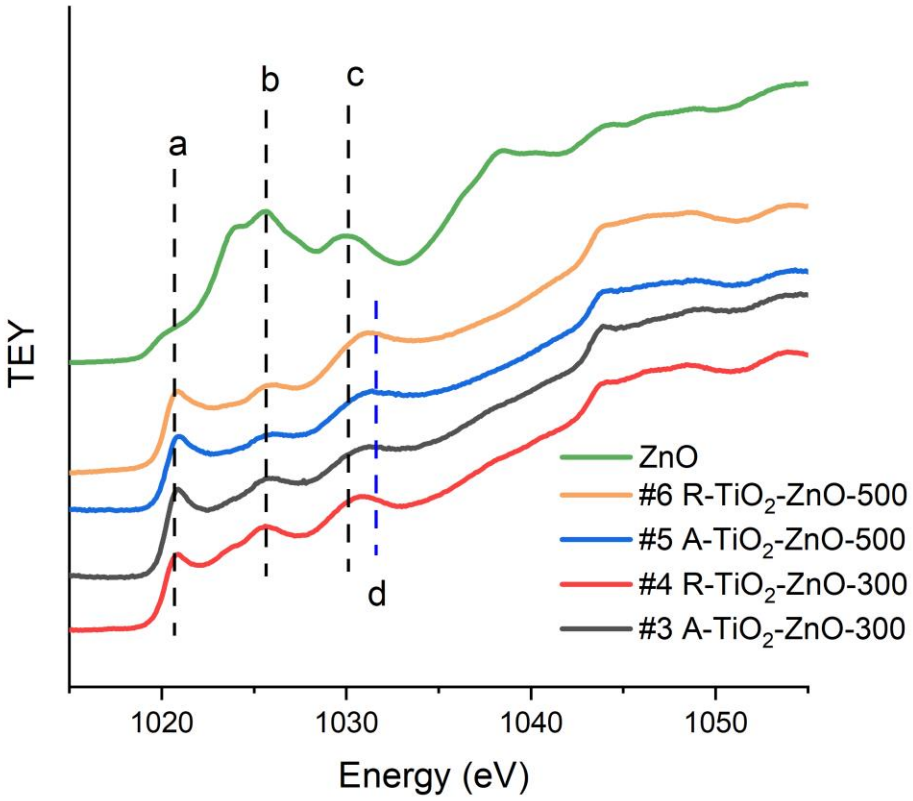

Figure 4-9. XAS spectra at the Zn $L_{3,2}$-edge of samples 3,4,5, 6, and reference ZnO

For samples 3-6, as shown in Figure 4-9, the spectra varied from that of ZnO, substantiating the absence of ZnO on the surfaces of samples. Nonetheless, three peaks (a, b, and d) are present in samples # 3, #4, #5, and #6, and exhibit a zinc sulphate like structure (Appendix B), Zn^{2+} cations are coordinated to Oxygen in octahedral symmetry, with a coordination number of 6[21]. There is a transformation in chemical environment around Zn^{2+} shifting from tetrahedral to octahedral symmetry, which results in a slight peak shift from c to e. All four samples exhibit the same features, thereby corroborating the results from XRD; new zinc titanium compounds were formed after the high-speed ball-milling process. Moreover, it should be noted that the proportion of peak a in samples is greater than ZnO. This implies a more substantial electrons transfer from 2p occupied orbitals to the unoccupied 4s or 3d states likely attributable to the chemical environment changes of Zn^{2+} cations.

4.3.3.4 XES spectra at the Zn $L_{3,2}$-edge

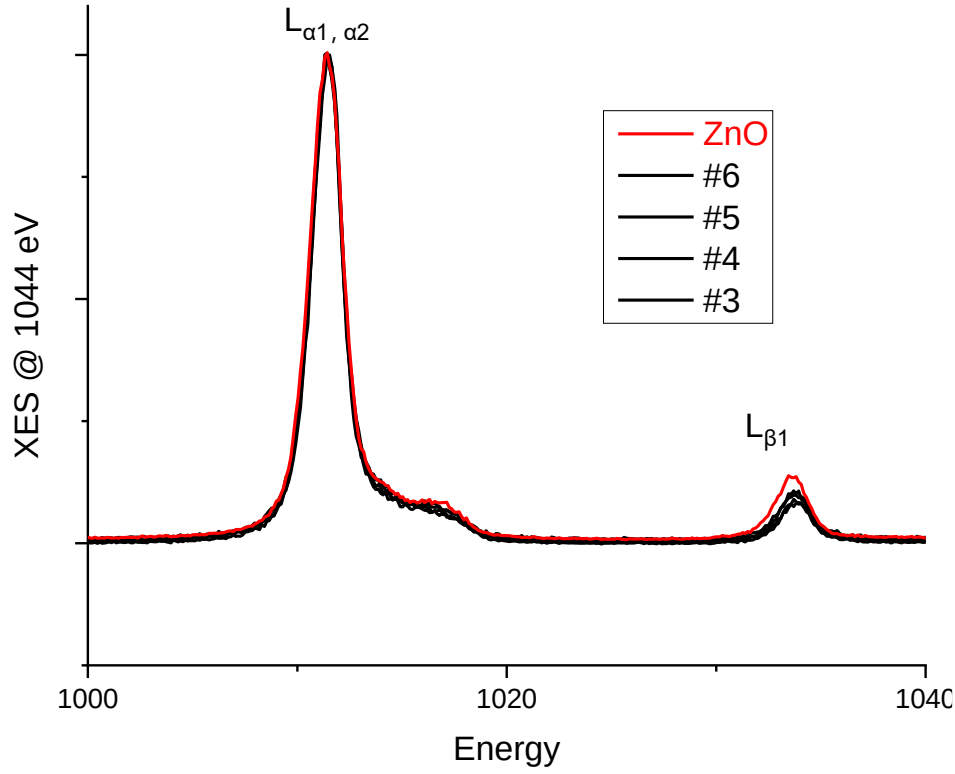

Figure 4-10. XES spectra at the Zn $L_{3,2}$-edge with 1044 eV of samples 3,4,5, 6, and reference ZnO

Figure 4-10 displays the XES spectra of samples 3-6 and ZnO at 1044 eV. Contrary to XAS, the XES spectra presents the photon emission from upper-energy orbitals to core holes. At Zn $L_{3,2}$-edge, after energy absorption from X-ray, the electron from the 2p orbital becomes excited to unoccupied orbitals, leaving some holes behind. The refilling of the core hole in $2p_{3/2}$ orbitals by electrons from $3d_{5/2, \text{ and } 3/2}$ orbitals defines the $L_{\alpha 1, \alpha 2}$ fluorescence. The first sharp peaks of samples and ZnO in Figure 4-10 represent the $L_{\alpha 1, \alpha 2}$ fluorescence. The shoulder area around the sharp peaks of samples is slightly smaller than the ZnO. Figure 4-11 illustrates the calculated DOS of $ZnTiO_3$. The main contributor for VB is O-2p electrons and the minor contributors are Zn-3d, Ti-3d electrons, while the main contributor for CB is Ti-3d orbitals. Besides that, the hybridizations between Zn-3d and O-2p states can be clearly observed. Combining the information of Figure 4-10 and 4-11, it is evident that more electrons are transferred from O-2p orbitals to unoccupied states (mainly Ti-3d orbitals) in the samples than ZnO. Understandably, there are fewer electrons

transferred from Zn-$3d_{5/2, 3/2}$ orbitals to core holes in the O-2p orbital in samples compared to ZnO. The $L_{\beta 1}$ fluorescence peaks, indicating the filling electron is from $3d_{3/2}$ orbital to $2p_{1/2}$ orbitals, also show similar results to $L_{\alpha 1,\alpha 2}$ fluorescence peaks, a consequence of the chemical environment changes of Zn^{2+} cations.

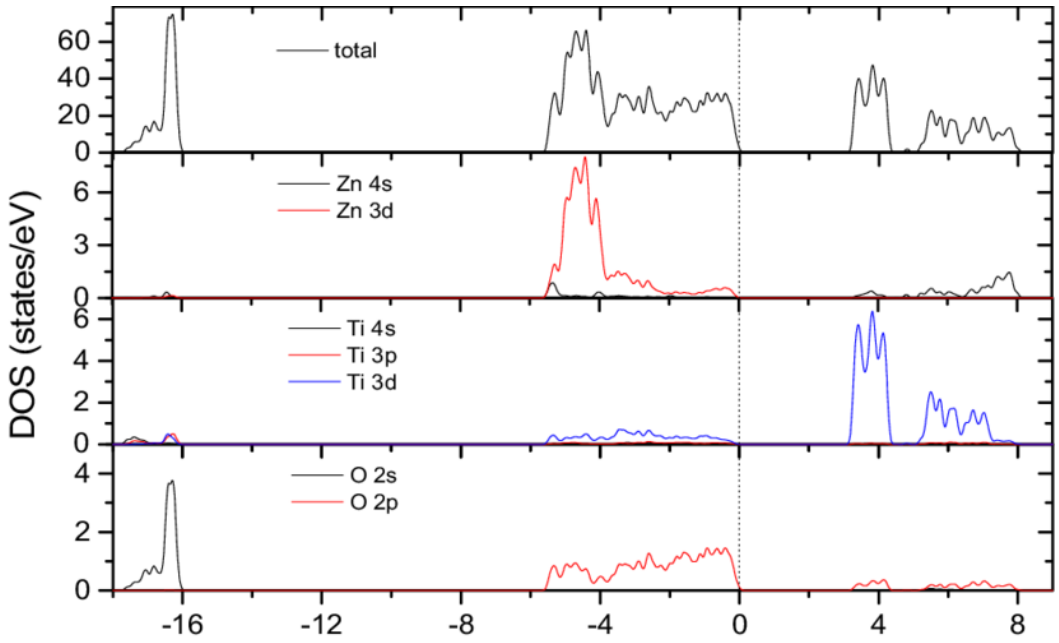

Figure 4-11. Calculated DOS of $ZnTiO_3$ with the Fermin levels at 0 eV[22].

4.3.4 2D XEOL-XANES Spectra

As introduced in Chapter 2, X-ray Excited Optical Luminescence (XEOL) represents a process of photon-induced emission where substances emit visible light upon X-ray irradiation. These selected X-rays trigger an excitation within the atomic structure of the material, exciting electrons to higher energy states. Following this excitation, the electrons undergo decay or recombination with holes, predominantly near the bandgap of the material, resulting in light emission. The luminescence provides critical insights into the electronic configuration and defect states within the material under investigation. The efficacy of the XEOL process can be affected by factors such as the efficiency of energy transfer and the presence of diverse defect states.

Two-dimensional X-ray absorption near-edge structure-X-ray excited optical luminescence (2D XANES-XEOL) is a relatively novel synchrotron spectroscopy technique to analyze the optical luminescence properties of materials. In the photoluminescence yield (PLY) mode, the XANES

and XEOL can be recorded simultaneously while the spectra are measured in the UV-vis region. 2D XANES-XEOL is the combination of wavelength-selective-optical-XANES spectra and excitation-energy-selective XEOL spectra, providing a multidimensional model for data analysis of the luminescence properties of materials while maintaining the elemental specificity obtained from XANES[25,26]. 2D XANES-XEOL spectra were measured in the SGM beamline at CLS, designed for the soft X-ray absorption region. In the soft X-ray region, XEOL is particularly effective. Compared to the hard-X-ray techniques, the considerably reduced thermalization track of the secondary process significantly influences the transformation from X-ray to visible light. Additionally, the high absorption cross-section can result in the high absorption of the incident light, further enhancing the contrast in the optical yield[27].

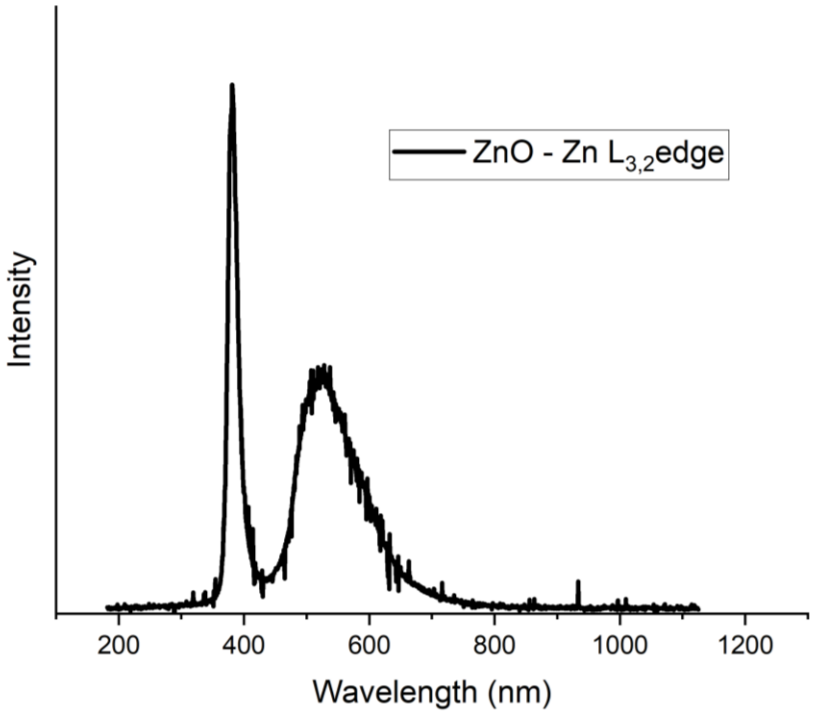

Figure 4-12. XEOL spectrum of reference ZnO at Zn $L_{3,2}$-edge

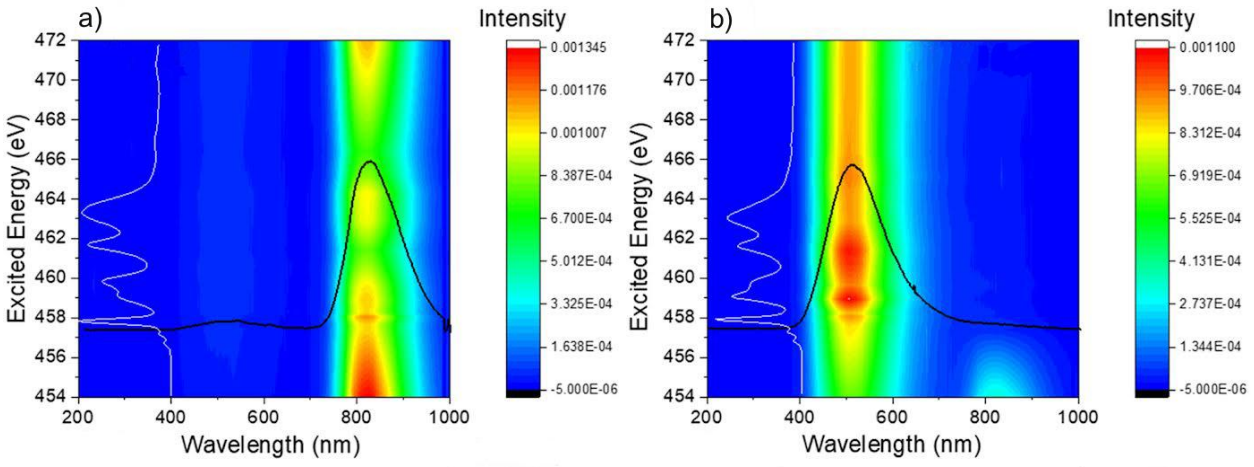

Figure 4-13. 2D-XANES-XEOL spectrum of a) rutile-dominated TiO_2 b) anatase-dominated TiO_2[24]

Figure 4-12 illustrates the XEOL spectrum of reference ZnO at Zn $L_{3,2}$-edge. A sharp peak around 380 nm is attributed to the band gap emission (BGE), while a broad peak around 510 nm is results from the defect emission (DE). Specifically, the DE in particular is indicative of O_{vac} in the near-surface region of the material[23]. Figure 4-13 shows the 2D-XANES-XEOL spectrum of rutile-dominated and anatase-dominated TiO_2. The anatase-dominated TiO_2 exhibit a broad emission band centralized around 520 nm (Figure 4-13 b), while the rutile-dominated TiO_2 exhibit a broad emission band centered around 825 nm (Figure 4-13 a). Figures 4-12 and 4-13 can be employed for comparative analysis of samples.

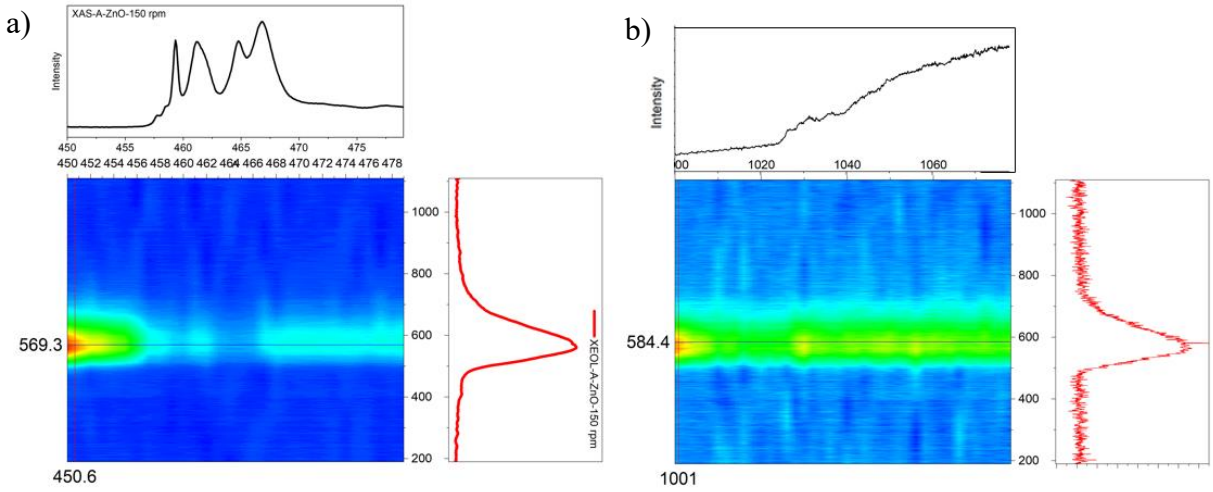

Figure 4-14. The 2D-XANES-XEOL map of sample #1 a) at Ti $L_{3,2}$-edge b) Zn $L_{3,2}$-edge. The top figure is the XANES spectra, the middle figure is mapping, and the right figure is XEOL. In the mapping figures, the X-axis is wavelength with a unit of nm, the Y-axis is excitation energy (eV), and the Z-axis is the intensity which is represented by colors.

Figure 4-14 shows the 2D XANES-XEOL map of sample #1, in which the depth of color presents the relative intensity of the XEOL across the selected energy ranges, including 450-475 eV (across Ti $L_{3,2}$-edge) and 1000-1080 eV (across Zn $L_{3,2}$-edge). The right attached figures are vertical cuts of the maps which show the XEOL spectra (wavelength window) excited at an excitation energy of interest. As shown in Fig. 4-14 a and b, one broad green peak at 569.3 nm at Ti $L_{3,2}$-edge, and another one at 584.4 nm at Zn $L_{3,2}$-edge, in detail the O_{vac} firstly increased around 470- 570 eV and then decreased around 570-650 eV. Compared to the reference ZnO XEOL spectra (Figure 4-12), the emission peak shows the right shift. Moreover, there might be anatase TiO_2-related peaks presented in the XEOL spectra around 590 nm[28]. However, the XEOL single from ZnO displays a considerably higher intensity compared to that of anatase TiO_2, the spectrum is ZnO-dominated. It might be due to the competitiveness between two optical decay channels (anatase TiO_2 and ZnO) for achieving the recombination process of electron-hole pairs. This phenomenon shows that in the ZnO/TiO_2 heterostructure, both ZnO and TiO_2 luminescence were presented, which might have resulted in a different electron transfer model in the heterojunction. The right-shift peaks on the XEOL spectra might be due to the increased O_{vac} after the formation of heterostructures.

4.3.5 WIEN2k calculation fitting

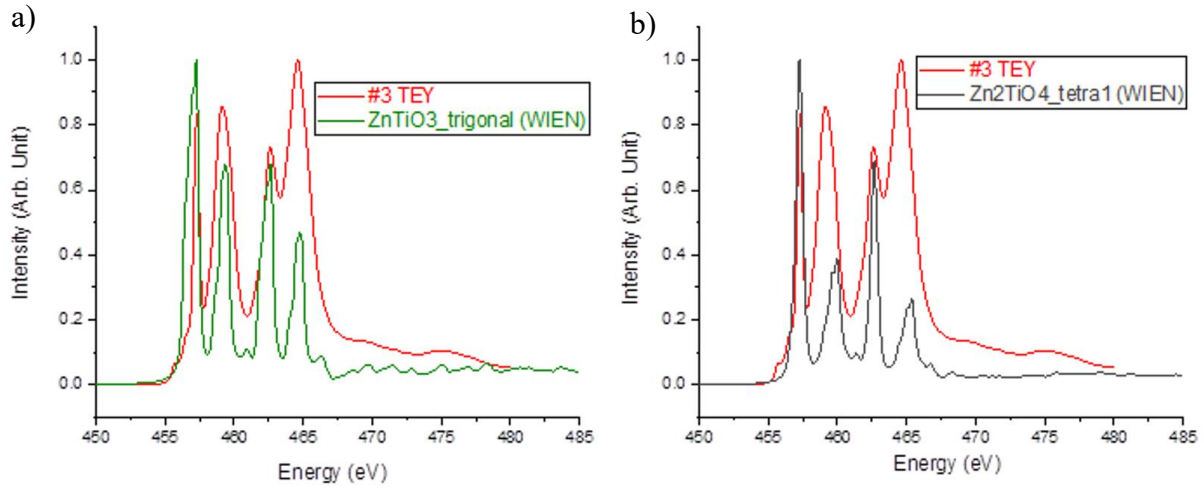

Figure 4-15. WIEN2k calculated TEY spectra compared with sample#3 a) calculated trigonal $ZnTiO_3$ crystal with measured sample#3 b) calculated tetragonal Zn_2TiO_4 with measured sample #3

XRD results have been reported in Chapter 4.3.2, however, the crystal structure of the new compounds is not determined. WIEN2k is a software program developed to execute computations of solid electronic structures, utilizing the foundational principles of quantum mechanics (density functional theory). One way to identify the crystal structure is by using a highly sophisticated WIEN2k program to calculate the theoretical TEY spectra based on the density functional theory (DFT).

In Figure 4-15, results from calculations performed using the WIEN2k software are depicted. The data reveals that the optimal crystal structure for $ZnTiO_3$ is trigonal. On the other hand, for the compound Zn_2TiO_4, a tetragonal crystal structure has been identified as the most fitting configuration. This comprehensive and rigorous analysis was not undertaken in isolation; rather, it was made possible through collaborative efforts with Dr. Yun-Mui Yiu, whose expertise and insights contributed substantially to the project.

4.3.6 Conclusion

In conclusion, chemical reactions transpired between TiO_2 and ZnO under the high rotational speed (300 and 500 rpm) extrusion of ball-milling. The formation of trigonal $ZnTiO_3$ and tetragonal Zn_2TiO_4, in terms of composition and chemical environments, was corroborated by XRD, XAS, and XES results. The Zn^{2+} cation in these new compounds exhibits more unoccupied states than ZnO. The existence of heterostructures and electron transfer properties were substantiated through XRD, TEM, XANES and XEOL techniques.

4.4 Ball-milling TiO_2/SnO_2 heterostructures

Same as Chapter 4.3, the ball-milling anatase TiO_2/SnO_2 and rutile TiO_2/SnO_2 heterostructure were studied in this chapter.

4.4.1 Morphology

Fig. 4-16 illustrates the morphology of sample #7, wherein the sample surface reveals a hierarchical structure with nanoparticle formation. The smaller particles, approximately 50 nm in diameter, can presumably be ascribed to the anatase TiO_2, while the presence of a larger nanoparticle could suggest the existence of SnO_2. Moreover, the particles aggregate into a bulky structure, rendering the boundaries between different particles indistinct.

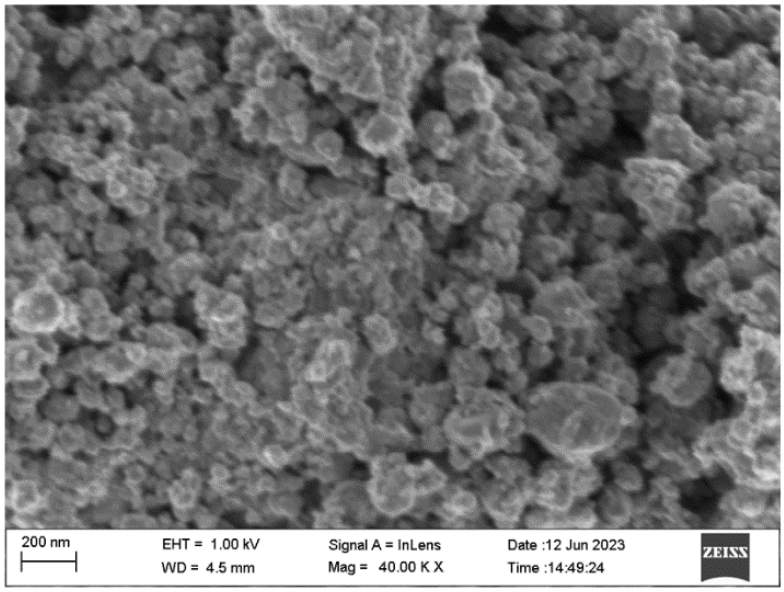

Figure 4-16. SEM images with an acceleration voltage of 1 kV and a magnification of 40 kx for sample #7

Figure 4-17 exhibits the TEM images showcasing the morphology and crystal structure of ball-milling rutile TiO_2/SnO_2 heterojunction at a rate of 150 rpm (sample#8). The SnO_2 nanoparticle, with diameters about 40-50 nm, appears to have attached on the top of the TiO_2 nanoparticle forming a heterostructure. In more detail, a lattice spacing of 0.326 nm is indicative of the (110) plane of rutile TiO_2[8]. Another crystal has a lattice spacing of 0.298 nm, indicative of the (111) plane of SnO_2[29].

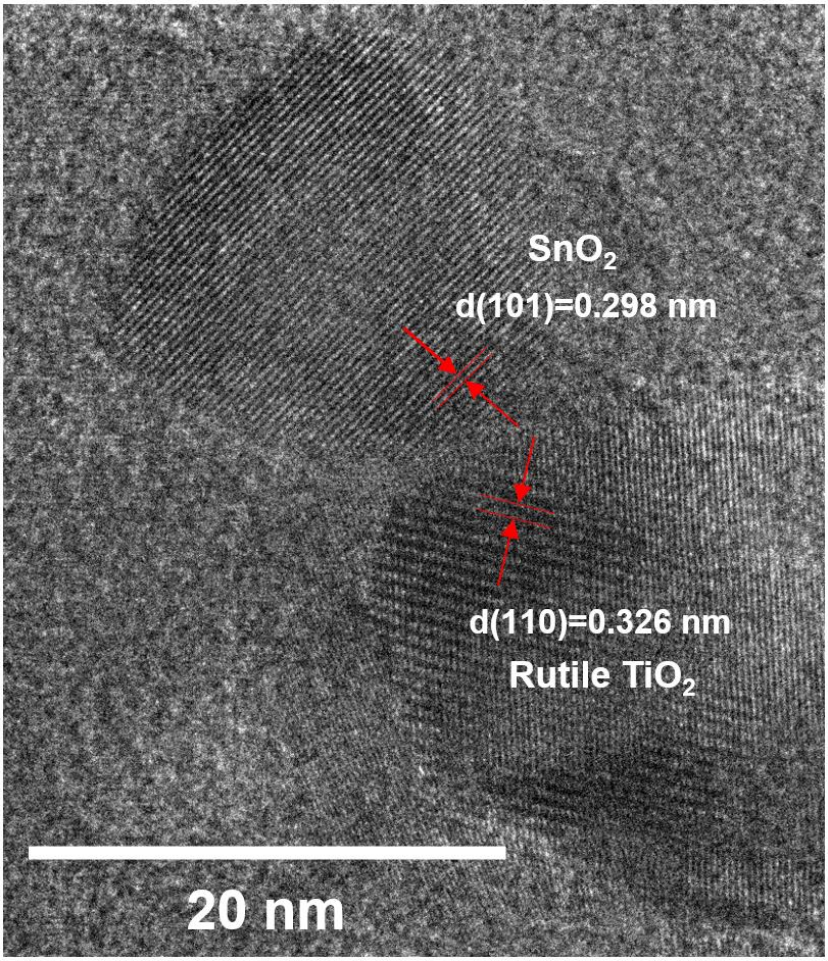

Figure 4-17. TEM images of sample #8 with a magnification of 630 kx

4.4.2 Chemical composition

To corroborate the presence of heterostructures and novel chemical compounds, it is critical to utilize XRD analysis for verification of the chemical composition in the samples. Standard PDF cards facilitate the identification of these chemicals by enabling comparison. Only signals from precursors have been observed for samples #7 and #8 (figure 4-18 a and b), which aligns with the data obtained from SEM investigations. At a relatively reduced ball milling rate, no chemical reactions were observed, instead, an effective surface modification of TiO_2 and SnO_2 occurred, resulting in the formation of heterostructures.

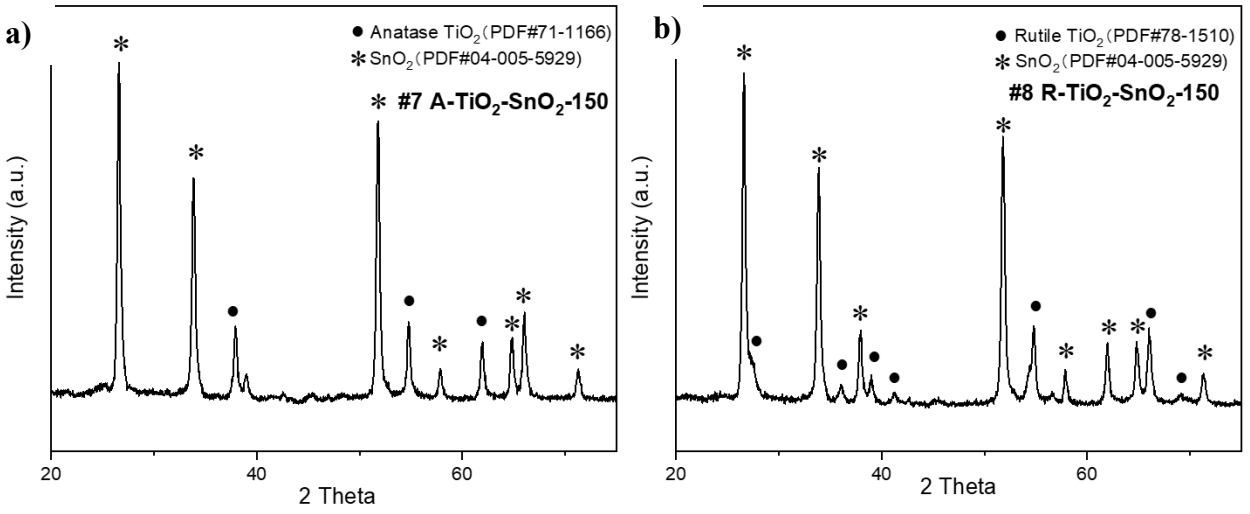

Figure 4-18. XRD images of a) sample #7 with SnO_2 PDF #04-005-5929 and anatase TiO_2 PDF #71-1166 b) sample #8 with SnO_2 PDF #04-005-5929 and rutile TiO_2 PDF #78-1510

4.4.3 XANES analysis

X-ray absorption near-edge structures (XANES) spectra were taken for samples #7 and #8 across the Ti $L_{3,2}$-edge and O K-edge.

4.4.3.1 XAS spectra at the Ti $L_{3,2}$-edge

Fig. 4-19 illustrates the XANES spectra of TiO_2/SnO_2 ball-milling heterostructured samples (sample #7 and 8) and reference anatase, rutile TiO_2 in TEY detection mode. Additionally, the magnified view in the XANES spectra is used to provide more detailed information.

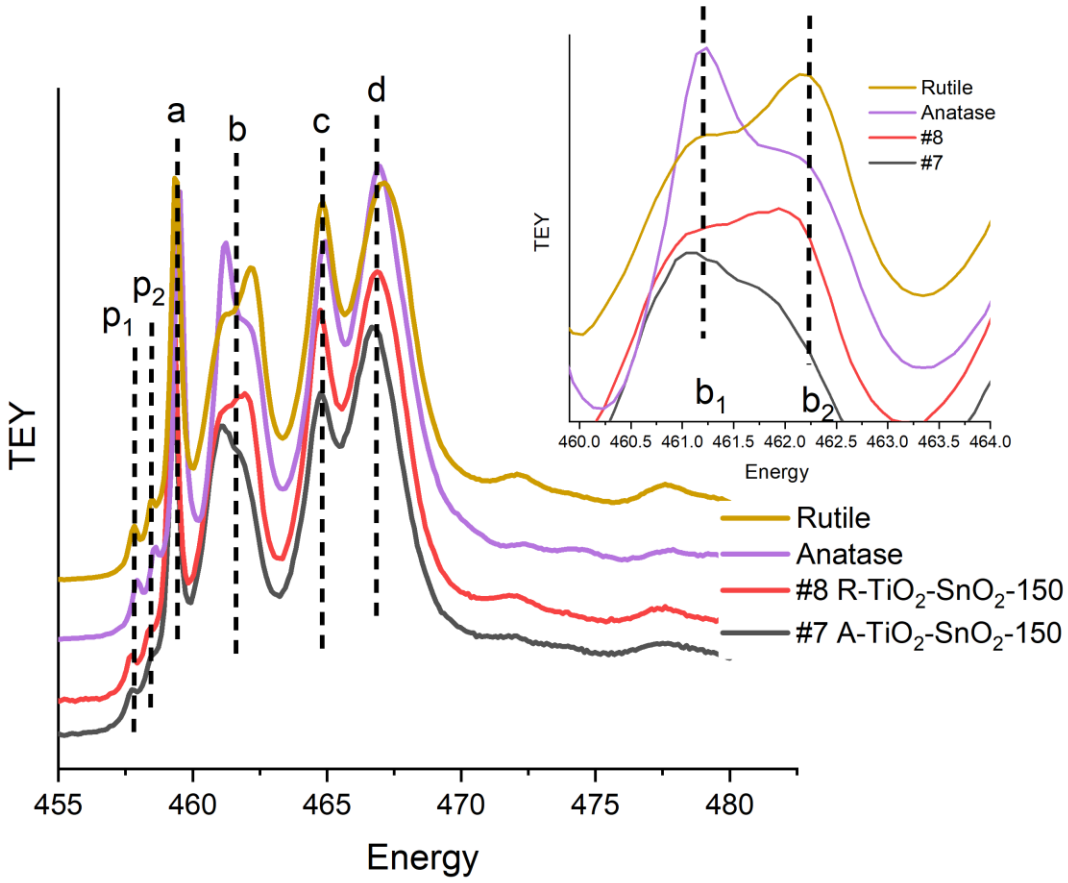

Figure 4-19. XANES spectra and inset XANES spectra at the Ti $L_{3,2}$-edge of samples 7,8, reference anatase and rutile TiO_2.

The spectra clearly show the small pre-edge p_1, p_2, and the sharpened peaks a (absorption edge), b, c, and d in both samples and reference chemicals. These peak features originated from the excitation of the electron from the 2p core level to unoccupied 3d states of the Ti atom as reported previously in chapter 4.3.3.1. In conclusion, sample #7 and #8 present similar but weaker peaks in peak b in comparison to anatase TiO_2 and rutile TiO_2 respectively. This observation could potentially be attributed to the emergence of the heterostructure and the reduced TiO_2 concentration. Specifically, it could be ascribed to the creation of defect with an increased number of such vacancies becoming available for utilization during the photocatalyst activities[19].

4.4.3.1 XANES spectra at the O K-edge

XANES investigations examine the unoccupied density states that are above the Fermi-level, facilitated by the application of dipole selection rules: O K-edge is s to p electronic transition. As introduced in chapter 4.3.3.2, peaks a, b, c (c_1 and c_2) and d (d_1 and d_2) are representing the electronic transition from O 1s to 2p states while hybridized with unoccupied splitting Ti 3d orbitals and Ti 2p, 4s and 4p states[14,15]. In detail, c_1 and d_1 peaks are fingerprints of anatase TiO_2, while c_2 and d_2 are iconic features of rutile TiO_2.

In the XAS of reference SnO_2 (as shown in Fig. 4-20), an initial sharp peak (peak 2) succeeded by a broader structured feature (peaks 3 and 4). Based on the calculated DOS[30,31], the first distinct peak (peak 2) originated from the O 2sp antibonding σ^* states hybridized with the unoccupied 5s states. The intensity of peak 2 is correlated with the bonding strength of Oxygen within the threefold planar coordination. The following broad peak (peaks 3 and 4) can be attributed to the O 2sp states and O 2p state hybridized with the Sn 5p orbital[32].

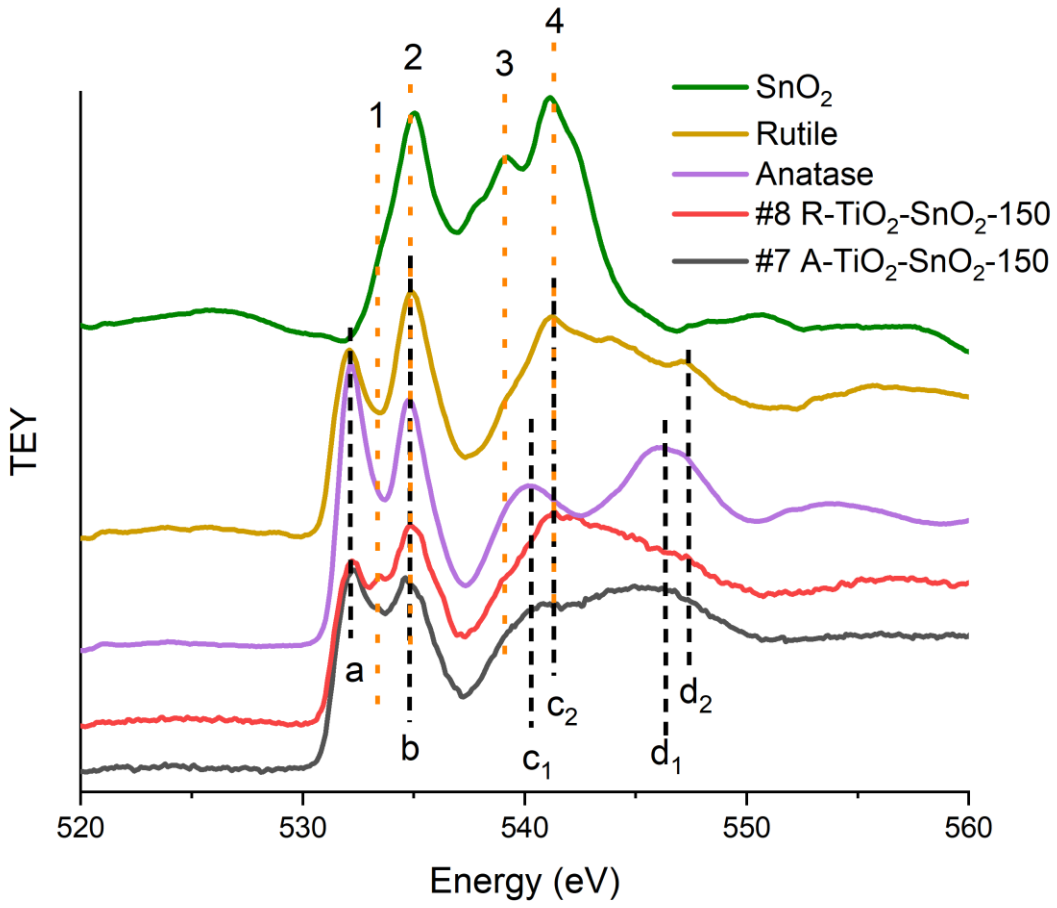

Figure 4-20. XANES spectra and inset XANES spectra at the Ti O K-edge of samples 7,8, reference SnO_2 and anatase and rutile TiO_2.

In samples #7 and #8, TiO_2-dominated features are exhibited in the XANES spectra. Similar peaks features are present in the samples compared to the reference data. Sample#7 is produced by the anatase TiO_2 and SnO_2 nano powder, correspondingly the same peaks a, b, c_1 and d_1 are shown in the sample's spectra. Similarly, sample #8 shows the same features as rutile TiO_2. However, it is clear that the intensity of those peaks decreased, which could result in the presence of defects in the heterostructures. Meanwhile, there is a new peak 1 present compared to the reference TiO_2 spectra, which might be contributed to the existence of increasing absorption edge in SnO_2. One of the possible reasons for the broadened peak feature is the formation of heterostructure resulting in the increased size of samples (TiO_2 and SnO_2 nanoparticles aggregated together). The higher distribution of sample size in bulk powder, the broader peak it can induce with.

4.4.4 2D XEOL-XANES Spectra

Through the combination of excitation-energy-selective XEOL and wavelength-selective-optical-XANES, the luminescence properties of materials can be studied, while preserving the elemental specificity derived from XANES. This allows us to understand the nature of the X-ray excited optical luminescence process in the samples. While bulk SnO_2 does not exhibit luminescent properties, SnO_2 in the nanodomain has demonstrated a strong and broad luminescence peak, typically attributed to surface defects in the near-surface region[33,34]. In detail, the observed luminescence is ascribed to the radiative decay of electrons -- some electrons are trapped in the defects marginally below the conduction band (CB), while other transition from the CB to intrinsic surface states within the band gap[35].

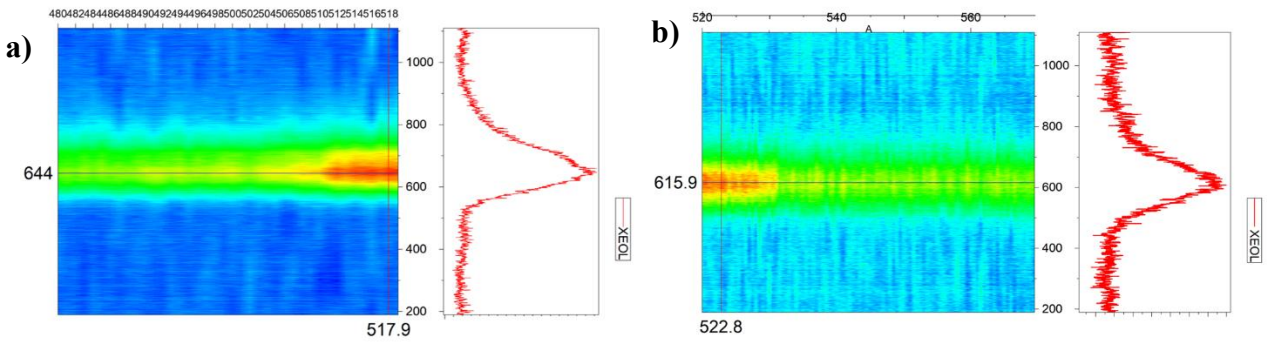

Figure 4-21. 2D XEOL-XANES spectra of sample #7 a) at Sn $M_{5,4}$-edge b) O K-edge

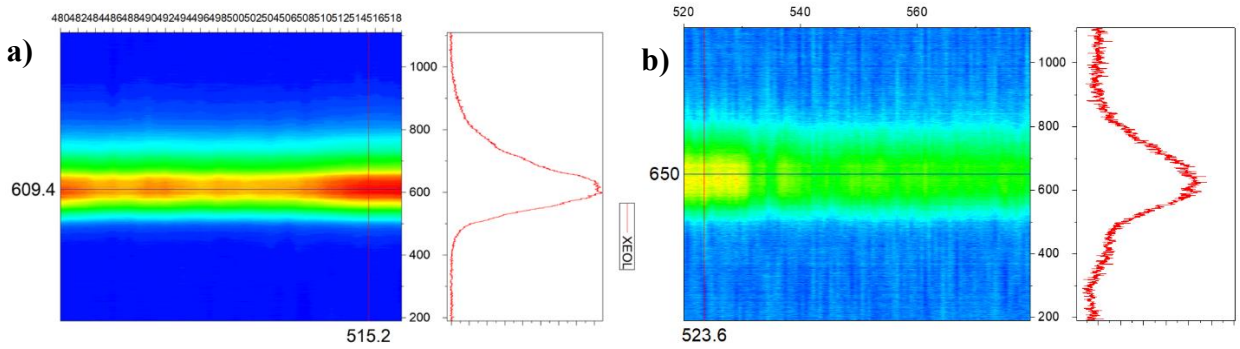

Figure 4-22. 2D XEOL-XANES spectra of sample #8 a) at Sn $M_{5,4}$-edge b) O K-edge

Figures 4-21 and 4-22 show the 2D-XEOL-XANES spectra for ball-milling anatase TiO_2/SnO_2 and rutile TiO_2/SnO_2 samples across Sn $M_{5,4}$-edge (480-520 eV) and O K-edge (520-570 eV). All spectra showed a broad, intense emission band around 410-900 nm (3.02-1.38 eV), centered at approximately 610 nm or 645 nm. No emission can be attributable to the BG of SnO_2 (3.6 eV), which would otherwise be detectable as a small peak at 344 nm. This absence of emission might be a result of surface modification after the formation of the heterostructure. Moreover, no anatase TiO_2-related peaks were presented in the XEOL spectra, potentially due to the competition between two optical decay channels (TiO_2 and SnO_2) for achieving the recombination process of electron-hole pairs. This phenomenon suggests that in the SnO_2/TiO_2 heterostructure, only SnO_2 luminescence is predominantly present, indicating a potential competitive luminescence within the heterostructure.

4.5 Summary

Two notable results emerged following the ball-milling treatments. On one hand, at a rate of 150 rpm heterostructured metal oxides formed, including anatase TiO_2-ZnO, rutile TiO_2-ZnO, anatase TiO_2-SnO_2 and rutile TiO_2-SnO_2. This was confirmed by the XRD, EDX and HR-TEM techniques in chemical composition and morphology. Furthermore, the 2D-XEOL-XANES spectra proved the competitiveness between two luminescence materials, which might be due to electron transfer between heterojunctions due to band alignment. Specifically, within the heterostructured TiO_2-ZnO system, ZnO was identified as the primary contributor to luminescence; similarly, in the heterostructured TiO_2-SnO_2, SnO_2 was the main contributor in luminescence, since both are stronger light emitting materials than TiO_2.

On the other hand, at a higher rate (300 and 500 rpm), new chemical compounds were synthesized. The results from XRD, XAS, and XES confirmed the formation of trigonal $ZnTiO_3$ and tetragonal Zn_2TiO_4 in composition and chemical environments. And XANES and XES spectra further illustrate the change in chemical structure. Specifically, The Zn^{2+} cation in new compounds has more unoccupied states than ZnO.

4.6 Reference

1. Yang, B., Wang, J., Jiang, C., Li, J., Yu, G., Deng, S., Lu, S., Zhang, P., Zhu, C., Zhuo, Q. (2017a). Electrochemical mineralization of perfluorooctane sulfonate by novel F and Sb co-doped Ti/SnO_2 electrode containing Sn-Sb Interlayer. Chemical Engineering Journal, 316, 296–304. https://doi.org/10.1016/j.cej.2017.01.105
2. Peng, Y., Wang, K. K., Liu, T., Xu, J., Xu, B. G. (2017a). Synthesis of one-dimensional Bi_2O_3-$Bi_2O_{2.33}$ heterojunctions with high interface quality for enhanced visible light photocatalysis in degradation of high-concentration phenol and Mo Dyes. Applied Catalysis B: Environmental, 203, 946–954. https://doi.org/10.1016/j.apcatb.2016.11.011
3. Abdel-Messih, M. F., Ahmed, M. A., El-Sayed, A. S. (2013). Photocatalytic decolorization of Rhodamine B Dye using novel mesoporous SnO_2-TiO_2 nano mixed oxides prepared by sol–gel method. Journal of Photochemistry and Photobiology A: Chemistry, 260, 1–8. https://doi.org/10.1016/j.jphotochem.2013.03.011
4. Le, T. H., Truong, Q. D., Kimura, T., Li, H., Guo, C., Yin, S., Sato, T., Ling, Y.-C. (2013). Construction of 3D hierarchical SnO_2 microspheres from porous nanosheets towards no decomposition. Solid State Sciences, 15, 29–35. https://doi.org/10.1016/j.solidstatesciences.2012.09.004
5. Ban, V., Sadikin, Y., Lange, M., Tumanov, N., Filinchuk, Y., Černý, R., Casati, N. (2017). Innovative in situ ball mill for X-ray diffraction. Analytical Chemistry, 89(24), 13176–13181. https://doi.org/10.1021/acs.analchem.7b02871
6. Zhang, X., Pan, J., Zhu, C., Sheng, Y., Yan, Z., Wang, Y., Feng, B. (2015). The visible light catalytic properties of carbon quantum dots/ZnO nanoflowers composites. Journal of Materials Science: Materials in Electronics, 26(5), 2861–2866. https://doi.org/10.1007/s10854-015-2769-x
7. Zhu, M., Deng, X., Lin, X., Zhang, L., Zhang, W., Lv, Y., Pan, J. (2018). The carbon quantum dots modified ZnO/TiO_2 nanotube heterojunction and its visible light photocatalysis enhancement. Journal of Materials Science: Materials in Electronics, 29(13), 11449–11456. https://doi.org/10.1007/s10854-018-9237-3
8. He, J., Du, Y., Bai, Y., An, J., Cai, X., Chen, Y., Wang, P., Yang, X., Feng, Q. (2019a). Facile formation of anatase/rutile TiO_2 nanocomposites with enhanced photocatalytic activity. Molecules, 24(16), 2996. https://doi.org/10.3390/molecules24162996
9. de Groot, F. M., Fuggle, J. C., Thole, B. T., Sawatzky, G. A. (1990). $L_{2,3}$ X-ray-absorption edges of d^0 compounds: K^+, Ca^{2+}, Sc^{3+}, and Ti^{4+} in O_h (octahedral) symmetry. Physical Review B, 41(2), 928–937. https://doi.org/10.1103/physrevb.41.928
10. Chen, S. C., Sung, K. Y., Tzeng, W. Y., Wu, K. H., Juang, J. Y., Uen, T. M., Luo, C. W., Lin, J.-Y., Kobayashi, T., Kuo, H. C. (2013). Microstructure and magnetic properties of oxidized titanium nitride thin films in-situ grown by pulsed laser deposition. Journal of Physics D: Applied Physics, 46(7), 075002. https://doi.org/10.1088/0022-3727/46/7/075002
11. Crocombette, J. P., Jollet, F. (1994). Ti 2p X-ray absorption in titanium dioxides (TiO_2): The influence of the cation site environment. Journal of Physics: Condensed Matter, 6(49), 10811–10821. https://doi.org/10.1088/0953-8984/6/49/022
12. de Groot, F. M., Fuggle, J. C., Thole, B. T., Sawatzky, G. A. (1990a). 2p X-ray Absorption of 3d Transition-Metal Compounds: An Atomic Multiplet Description including the Crystal Field. Physical Review B, 42(9), 5459–5468. https://doi.org/10.1103/physrevb.42.5459

13. Kucheyev, S. O., van Buuren, T., Baumann, T. F., Satcher, J. H., Willey, T. M., Meulenberg, R. W., Felter, T. E., Poco, J. F., Gammon, S. A., Terminello, L. J. (2004). Electronic structure of titania aerogels from soft X-ray absorption spectroscopy. Physical Review B, 69(24). https://doi.org/10.1103/physrevb.69.245102
14. Hwu, Y., Yao, Y. D., Cheng, N. F., Tung, C. Y., Lin, H. M. (1997). X-ray absorption of Nanocrystal TiO_2. Nanostructured Materials, 9(1–8), 355–358. https://doi.org/10.1016/s0965-9773(97)00082-2
15. Finkelstein, L. D., Zabolotzky, E. I., Korotin, M. A., Shamin, S. N., Butorin, S. M., Kurmaev, E. Z., Nordgren, J. (2002). Vacant states of TiO_2 with rutile structure and their reflection in different-type X-ray absorption spectra. X-Ray Spectrometry, 31(6), 414–418. https://doi.org/10.1002/xrs.596
16. Wu, Z. Y., Ouvrard, G., Gressier, P., Natoli, C. R. (1997). Ti and O k edges for titanium oxides by multiple scattering calculations: Comparison to XAS and Eels Spectra. Physical Review B, 55(16), 10382–10391. https://doi.org/10.1103/physrevb.55.10382
17. Stewart, S. J., Fernández-García, M., Belver, C., Mun, B. S., Requejo, F. G. (2006). Influence of N-doping on the structure and electronic properties of Titania nanoparticle photocatalysts. The Journal of Physical Chemistry B, 110(33), 16482–16486. https://doi.org/10.1021/jp0624451
18. Soriano, L., Abbate, M., Fuggle, J. C., Prieto, P., Jiménez, C., Sanz, J. M., Galán, L., Hofmann, S. (1993). Thermal oxidation of tin studied by means of soft X-ray absorption spectroscopy. Journal of Vacuum Science: Technology A: Vacuum, Surfaces, and Films, 11(1), 47–51. https://doi.org/10.1116/1.578718
19. Qiu, C., Odarchenko, Y., Meng, Q., Xu, S., Lezcano-Gonzalez, I., Olalde-Velasco, P., Maccherozzi, F., Zanetti-Domingues, L., Martin-Fernandez, M., Beale, A. M. (2022). Resolving the effect of oxygen vacancies on CO nanostructures using soft XAS/X-PEEM. ACS Catalysis, 12(15), 9125–9134. https://doi.org/10.1021/acscatal.2c00611
20. Nie, Y., Wang, Z., Wang, J., Bao, F., Zhang, J., Ma, Y., Sham, T.-K., Sun, X. (2017a). Synthesis and structure-dependent optical properties of ZnO Nanocomb and ZnO nanoflag. The Journal of Physical Chemistry C, 121(46), 26076–26085. https://doi.org/10.1021/acs.jpcc.7b08016
21. Caretti, I., Yuste, M., Torres, R., Sánchez, O., Jiménez, I., Escobar Galindo, R. (2012). Coordination chemistry of titanium and zinc in $Ti_{(1-x)}Zn_{2x}O_2$ ($0 \leqslant x \leqslant 1$) ultrathin films grown by DC reactive magnetron sputtering. RSC Advances, 2(7), 2696. https://doi.org/10.1039/c2ra01077a
22. Zhang, J., Xu, B., Wang, Y.-S., Qin, Z., Ke, S.-H. (2019). First-principles investigation of the Ferroelectric, piezoelectric and nonlinear optical properties of $LiNbO_3$-type $ZnTiO_3$. Scientific Reports, 9(1). https://doi.org/10.1038/s41598-019-53986-6
23. Wang, Z., Guo, X., Sham, T.-K. (2014). 2d Xanes-XEOL mapping: Observation of enhanced band gap emission from ZnO nanowire arrays. Nanoscale, 6(12), 6531–6536. https://doi.org/10.1039/c4nr01049c
24. Yao, L., Chen, J., Wang, Z., Sham, T.-K. (2022). TiO_2 nanotubes: Morphology, size, crystallinity, and phase-dependent properties from Synchrotron-spectroscopy studies. The Journal of Physical Chemistry C, 126(6), 3265–3275. https://doi.org/10.1021/acs.jpcc.1c10577
25. Li, J., Liu, L., Sham, T.-K. (2015). 2d XANES–XEOL spectroscopy studies of morphology-dependent phase transformation and corresponding luminescence from

hierarchical TiO_2 nanostructures. Chemistry of Materials, 27(8), 3021–3029. https://doi.org/10.1021/acs.chemmater.5b00363
26. Ward, M. J., Han, W.-Q., Sham, T.-K. (2011). 2D XAFS–XEOL mapping of $Ga_{1-x}Zn_xN_{1-x}O_x$ nanostructured solid solutions. The Journal of Physical Chemistry C, 115(42), 20507–20514. https://doi.org/10.1021/jp207545a
27. Sham, T.-K. (2002). Chemical applications of Synchrotron Radiation. World Scientific.
28. Vequizo, J. J., Kamimura, S., Ohno, T., Yamakata, A. (2018). Oxygen induced enhancement of NIR emission in Brookite TiO_2 powders: Comparison with rutile and anatase TiO_2 powders. Physical Chemistry Chemical Physics, 20(5), 3241–3248. https://doi.org/10.1039/c7cp06975h
29. Suito, K., Kawai, N., Masuda, Y. (1975). High pressure synthesis of orthorhombic SnO_2. Materials Research Bulletin, 10(7), 677–680. https://doi.org/10.1016/0025-5408(75)90050-1
30. Cabaret, D., Mauri, F., Henderson, G. S. (2007). Oxygen K -edge XANES of germanates investigated using first-principles calculations. Physical Review B, 75(18). https://doi.org/10.1103/physrevb.75.184205
31. Jollet, F., Noguera, C. (1993). Core hole effect on the XAS Si K edge shape in α-quartz. Physica Status Solidi (b), 179(2), 473–488. https://doi.org/10.1002/pssb.2221790222
32. Frati, F., Hunault, M. O., de Groot, F. M. (2020). Oxygen K-edge X-ray absorption spectra. Chemical Reviews, 120(9), 4056–4110. https://doi.org/10.1021/acs.chemrev.9b00439
33. Hu, J. Q., Bando, Y., Liu, Q. L., Golberg, D. (2003). Laser-ablation growth and optical properties of wide and long single-crystal SnO_2 ribbons. Advanced Functional Materials, 13(6), 493–496. https://doi.org/10.1002/adfm.200304327
34. Calestani, D., Lazzarini, L., Salviati, G., Zha, M. (2005). Morphological, structural and optical study of quasi‐1d SnO_2 nanowires and nanobelts. Crystal Research and Technology, 40(10–11), 937–941. https://doi.org/10.1002/crat.200410463
35. Zhou, X. T., Heigl, F., Murphy, M. W., Sham, T. K., Regier, T., Coulthard, I., Blyth, R. I. (2006). Time-resolved X-ray excited optical luminescence from SnO_2 nanoribbons: Direct evidence for the origin of the blue luminescence and the role of Surface States. Applied Physics Letters, 89(21). https://doi.org/10.1063/1.2387476

Chapter 5

Chapter 5 Summary and Outlook

5.1 Summary

The work in this thesis is performed on tracking the changes in the electronic and structural properties during the phase transition of TiO_2 and the formation of heterostructured metal oxides (TiO_2/ZnO and TiO_2/SnO_2). It was investigated by selected Synchrotron techniques such as XANES, XES and XEOL. The primary research is illustrated in Chapters 3 and 4.

In Chapter 3, I investigated an eco-friendly synthesis method to induce phase transformation in TiO_2 nanoparticles. Other researchers studied the importance of mixed-phase TiO_2 (anatase and rutile) in the improvement of photocatalyst activities[1,2]. In order to provide further confirmation of the phase transitions occurring during the sample modification process, a mixed-precursors system was utilized. The ball-milling process effectively induced the desired phase transitions, and an increase in the ball-milling rate resulted in a higher ratio of anatase-to-rutile on the surface. These findings were substantiated by XRD, SEM, TEM, and XANES techniques. The relative composition ratio was determined by employing the LCF method using Athena software. The ability to track the bulk properties with XRD and surface properties with TEY XANES is triumphantly demonstrated.

In Chapter 4, I investigated the influence of various Ball-Milling rates on the final products and the formation of heterostructure on the electric and luminescence properties. The importance of the formation of heterostructure (TiO_2, ZnO and SnO_2) was discussed in terms of its impact on the recombination rate of e^-/h^+ pairs in photocatalytic reactions. The ball-milling treatment resulted in two distinct outcomes. Initially, at a rate of 150 rpm, the formation of heterostructured metal oxides is observed, including anatase TiO_2-ZnO, rutile TiO_2-ZnO, anatase TiO_2-SnO_2 and rutile TiO_2-SnO_2. This was substantiated through the application of XRD, EDX, and HR-TEM methods which introduce their chemical composition and morphology. Notably, the XANES spectra indicated the existence of defect states and an increase in Oxygen vacancies, which is able to trap electrons and inhibit the recombination process of electron-hole pair. 2D-XEOL-XANES spectrum further confirmed the existence of a competitive scenario between two luminescent materials, potentially attributable to a novel electron transfer mechanism within the heterojunctions. Specifically, within

the heterostructured TiO_2-ZnO system, ZnO was identified as the primary contributor to luminescence; similarly, in the heterostructured TiO_2-SnO_2, SnO_2 was the main contributor in luminescence. Conversely, when subjected to a higher rate (300 and 500 rpm), the synthesis of new chemical compounds was observed. The emergence of trigonal $ZnTiO_3$ and tetragonal Zn_2TiO_4 in terms of their composition and chemical environments was validated through the results procured from XRD, XAS, and XES. The XANES and XES spectra provide additional insights into the transformations occurring within the chemical structure. Specifically, the Zn^{2+} cation within the newly synthesized compounds was observed to exhibit a higher number of unoccupied states compared to ZnO.

5.2 Outlook - The continuous XANES and XEOL study of heterostructured luminance semiconductors: ZnO/SnO_2

The growing interest in nanotechnology is reflected in the increasing number of electronic industry applications[3], including the production of optoelectronic devices[4], gas sensors[5] and solar cell electrodes[6]. A comprehensive understanding of semiconductors in the nano-domain will undoubtedly gain prominent attention in research. The current projects only focus on the phase transition of TiO_2 and the heterostructure study of TiO_2/ZnO and TiO_2/SnO_2. In future work, ZnO/SnO_2 heterostructure systems can be investigated. As mentioned in the previous chapters, both ZnO and SnO_2 in nano size exhibit luminescent properties with a bandgap of 3.37 eV and 3.6 eV, respectively[7–9]. Part of the characterization has been finished and shown in Fig 5-1 and 5-2. Furthermore, the electronic structure and chemical environment of Zn^{2+} and Sn^{2+} need to be determined by XANES and XES at the RIXIS beamline in CLS. And RXIS has been introduced in Chapter 2.

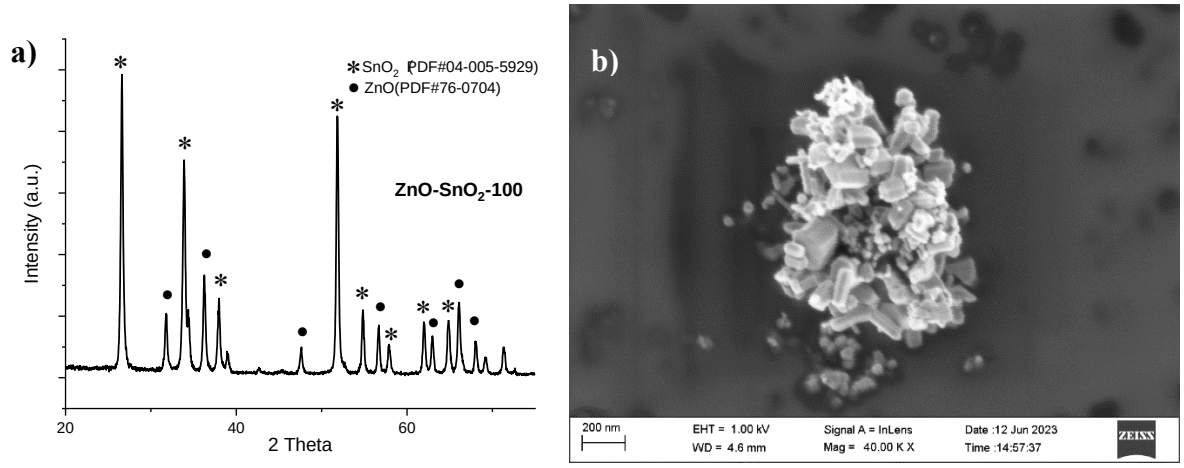

Figure 5-1. The information of chemical compostion and morphology a) XRD analysis of ZnO/SnO_2 heterostructure b) SEM image of ZnO/SnO_2 heterostructure with an acceleratteion voltagee of 1kV and a magnficaation of 40.00 kx

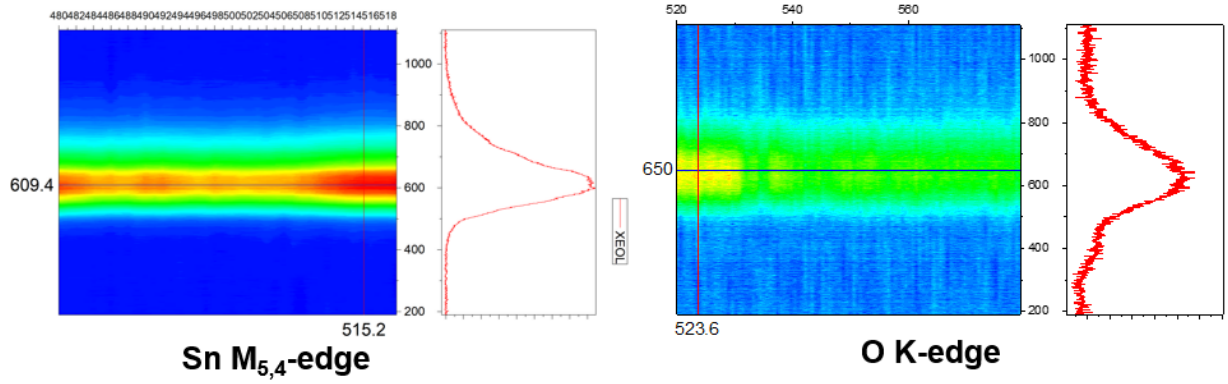

Figure 5-2. 2D XEOL-XANES spectrum of ZnO/SnO_2 heterostructure a) at Sn $M_{5,4}$-edge b) O K-edge

5.3 Outlook – The XANES and XEOL studies of heterostructure synthesis by two-step Chemical Vapor Deposition (CVD) method

Another method to synthesize heterostructured metal oxides is Chemical vapor deposition (CVD). Chemical vapor deposition (CVD) is a powerful synthesis method to produce advanced-performance material with volatile precursors, which react or decompose on the surface of the substrate in the presence of a reaction initiator, such as plasma or high temperatures[10]. In the two-step temperature-triggered CVD method, temperature control the deposition process in the Tube Furnace. First one precursor is deposited on the substrate by CVD, then the pre-deposited sample

will be used as substrate for another precursor to deposit. As a result, nanotube-formed heterostructure will be synthesized. The schematic image of temperature-controlled Tube Furnace is presented in Fig 5-3 a). And Fig 5-3 b) demonstrates the CVD synthesis in quartz tube.

Compared to the Ball-Milling heterostructure, the local and electronic structure might be different, which can be determined by XANES and XES in synchrotron center. Furthermore, the Oxygen vacancies and electron transfer on the interface in the nanotube-formed heterostructure can be identified by synchrotron techniques as well.

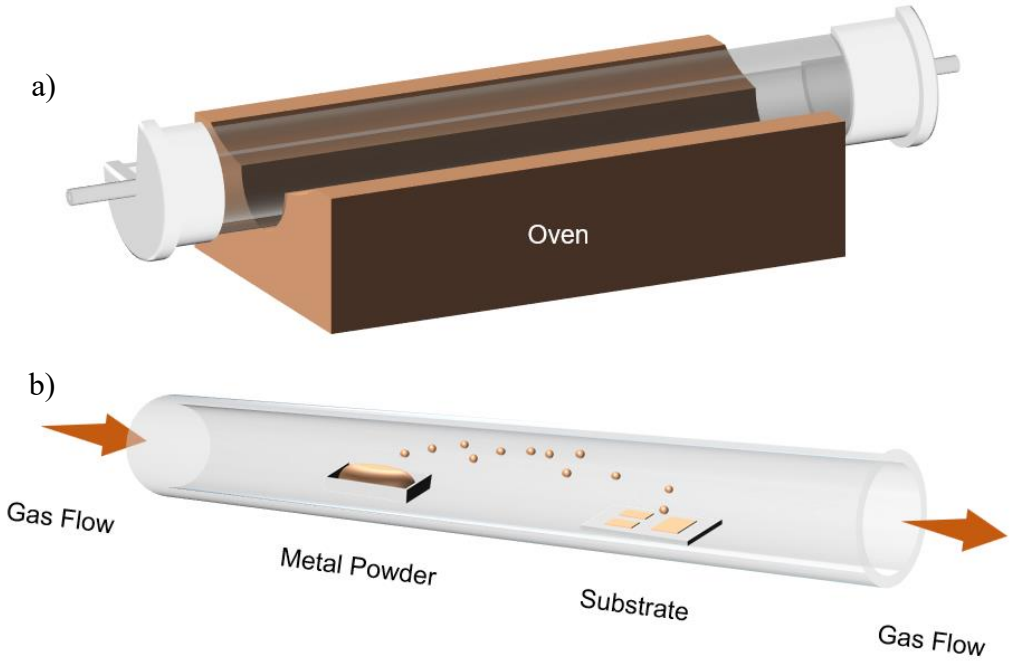

Figure 5-3. Schematic illustrations of a) Chemical Vapor Deposition Tube Furnace b) CVD process in quartz tube.

5.4 References

1. Ohno, T., Tokieda, K., Higashida, S., & Matsumura, M. (2003). Synergism between rutile and anatase TiO_2 particles in photocatalytic oxidation of naphthalene. Applied Catalysis A: General, 244(2), 383–391. https://doi.org/10.1016/s0926-860x(02)00610-5
2. Jia, J., Ohno, T., Matsumura, M. (2000). Efficient dihydroxylation of naphthalene on photo irradiated rutile TiO_2 powder in solution containing hydrogen peroxide. Chemistry Letters, 29(8), 908–909. https://doi.org/10.1246/cl.2000.908
3. Yang, X., Zhang, S., yu, Q., Zhao, L., Sun, P., Wang, T., Liu, F., Yan, X., Gao, Y., Liang, X., Zhang, S., Lu, G. (2019). One step synthesis of branched SnO_2/ZnO heterostructures and their enhanced gas-sensing properties. Sensors and Actuators B: Chemical, 281, 415–423. https://doi.org/10.1016/j.snb.2018.10.138
4. Shi, J., Zhang, J., Yang, L., Qu, M., Qi, D., Zhang, K. H. (2021). Wide bandgap oxide semiconductors: From materials physics to optoelectronic devices. Advanced Materials, 33(50). https://doi.org/10.1002/adma.202006230
5. Wang, Y., Jia, W., Strout, T., Schempf, A., Zhang, H., Li, B., Cui, J., Lei, Y. (2009). Ammonia gas sensor using polypyrrole-coated TiO_2/ZnO nanofibers. Electroanalysis, 21(12), 1432–1438. https://doi.org/10.1002/elan.200904584
6. Wibowo, A., Marsudi, M. A., Amal, M. I., Ananda, M. B., Stephanie, R., Ardy, H., Diguna, L. J. (2020). ZnO nanostructured materials for emerging solar cell applications. RSC Advances, 10(70), 42838–42859. https://doi.org/10.1039/d0ra07689a
7. Zhou, X. T., Heigl, F., Murphy, M. W., Sham, T. K., Regier, T., Coulthard, I., Blyth, R. I. (2006a). Time-resolved X-ray excited optical luminescence from SnO_2 nanoribbons: Direct evidence for the origin of the blue luminescence and the role of Surface States. Applied Physics Letters, 89(21). https://doi.org/10.1063/1.2387476
8. Raji, R., & Gopchandran, K. G. (2017). ZnO nanostructures with tunable visible luminescence: Effects of kinetics of chemical reduction and annealing. Journal of Science: Advanced Materials and Devices, 2(1), 51–58. https://doi.org/10.1016/j.jsamd.2017.02.002
9. Özgür, Alivov, Ya. I., Liu, C., Teke, A., Reshchikov, M. A., Doğan, S., Avrutin, V., Cho, S.-J., Morkoç, H. (2005). A comprehensive review of ZnO materials and Devices. Journal of Applied Physics, 98(4). https://doi.org/10.1063/1.1992666
10. Raiford, J. A., Oyakhire, S. T., Bent, S. F. (2020). Applications of atomic layer deposition and chemical vapor deposition for perovskite solar cells. Energy & Environmental Science, 13(7), 1997–2023. https://doi.org/10.1039/d0ee00385a

Appendices

Appendix A. The SEM images of reference a) anatase TiO_2, b) rutile TiO_2 and c) ZnO

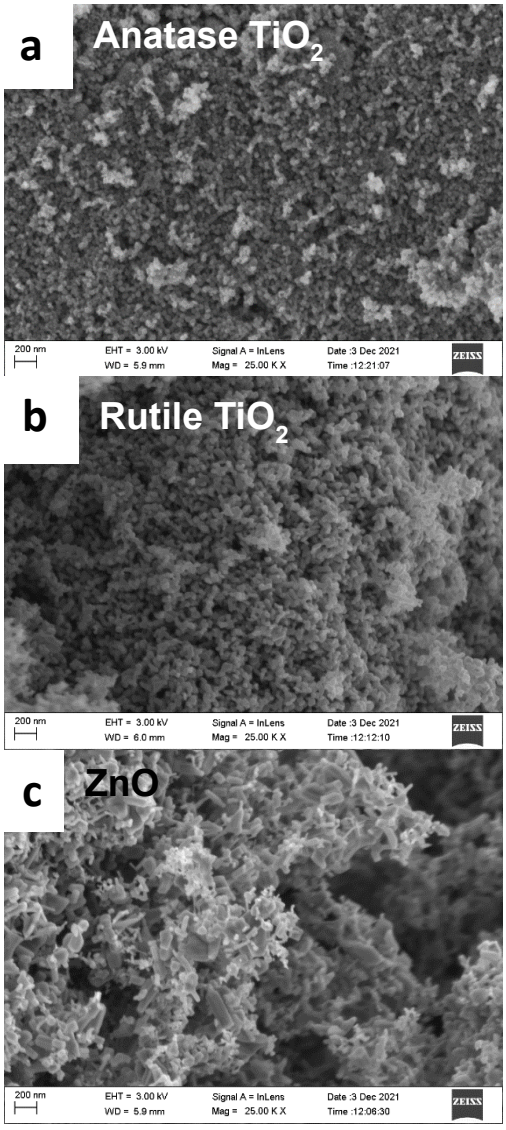

Appendix B. The XANES of $ZnSO_4$ at Zn $L_{3,2}$-edge[1]

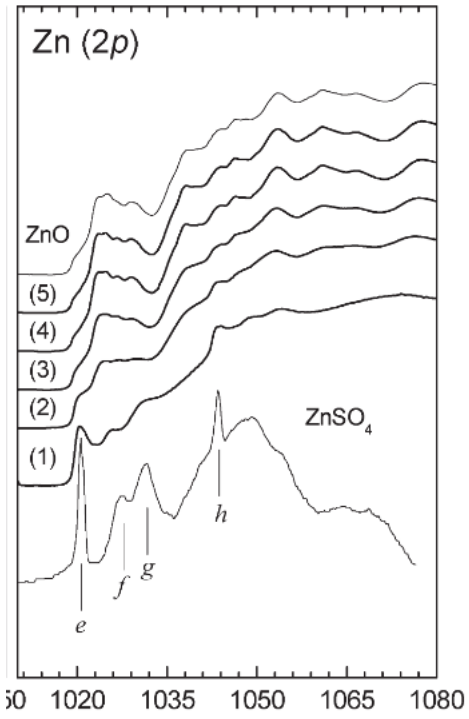

(1) Caretti, I.; Yuste, M.; Torres, R.; Sánchez, O.; Jiménez, I.; Escobar Galindo, R. Coordination Chemistry of Titanium and Zinc in TI(1−x)Zn2xO2 (0 ≤x≤ 1) Ultrathin Films Grown by DC Reactive Magnetron Sputtering. *RSC Advances* **2012**, *2*, 2696.

Bingyu (Caroline) Dong

SKILLS

- Cell Culture, Fume hood works
- Scanning Electron Microscopy
- EDX, XRD
- X-ray Spectroscopy: XAS, XES, XEOL
- Jade, LoggarPro
- MATLAB, R, Origin,
- Microsoft Excel, Word, PowerPoint
- Athena, Artemis, Hephaestus

EDUCATION

Western University Sept. 2021 – Present

Candidate for Master of Science in Thesis Base: Physical Chemistry

- **Capstone Thesis**: Preparation and Characterization of metal oxides heterostructures in nanodomain

Western University Sept. 2016 – Jun. 2020

Honor Specialization in Chemistry

- **Relevant Coursework:** Scientific Methods in Biology, Cell Biology, Organic Chemistry.

RESEARCH EXPERIENCE

Research Assistance

Soochow University – Suzhou, China May 2019 – Aug. 2019

- Leveraging strong knowledge of diverse operating instruments to drive testing and obtain accurate results.
- Developed the laboratory techniques of quantitative analytical separation and spectroscopy.

GRADUATED COURSE

- Chem9546S Optical Properties of Solids
- Chem9547T Surface Chemistry of Nanoparticles
- Chemistry 9774Q Synchrotron & Materials I
- Chemistry 9784R Synchrotron & Materials II